

Inhomogeneity in Intracluster Medium and Its Cosmological Implications

Hajime Kawahara

Department of Physics, Graduate School of Science,
The University of Tokyo

December 2008

Abstract

Recent progress both in numerical simulations and observations has improved physical modeling of galaxy clusters beyond a simple isothermal and spherical approximation for a variety of astrophysical and cosmological applications such as departure from isothermal distribution and non-spherical effect. Despite the previous studies, no physical model has been proposed for the statistical nature of inhomogeneities in the intracluster medium (ICM). We investigate the nature of inhomogeneity in ICM. We construct a statistical model of the density and temperature fluctuations on the basis of cosmological hydrodynamic simulations. We find that the local inhomogeneities of the temperature and density, after corrected for the global radial profiles, have nearly a universal distribution that resembles the lognormal probability density function.

With the lognormal model of the inhomogeneity, we investigate its impact on cosmological applications of galaxy clusters. We explore the origin of the recently reported systematic bias in the spectroscopic temperature of galaxy clusters. We develop an analytical model that explains the bias in the spectroscopic temperature. On the basis of the analytical model, we find that not only the radial profiles but also the local inhomogeneities are largely responsible for the above mentioned bias of cluster temperatures.

We also apply the lognormal model to the Hubble constant measurement from the combined analysis of the Sunyaev-Zel'dovich effect and X-ray observations of galaxy clusters. The Hubble constant estimated from this method has been known to be systematically lower than those from other methods by 10-15 percent. We examine the origin of the systematic underestimate and compare the prediction with idealistic triaxial models and with clusters extracted from cosmological hydrodynamic simulations. We identify three important sources for the systematic errors; density and temperature inhomogeneities in the ICM, departures from isothermality, and asphericity. We find that these systematics well reproduce both the observed bias and the intrinsic dispersions of the Hubble constant estimated from the Sunyaev-Zel'dovich effect.

In order to compare the lognormal model directly with X-ray observations, we develop a method of extracting statistical information about the density fluctuations from the X-ray surface brightness. Performing mock observations, we find that the resulting X-ray surface brightness fluctuations also follow the lognormal distribution fairly well. We analyze *Chandra* observations of the galaxy cluster Abell 3667, and find that its X-ray surface brightness fluctuations follow the lognormal distribution. While the lognormal model was originally motivated by hydrodynamic simulations, this is the observational confirmation of the lognormal signature in a real cluster.

We conclude that the inhomogeneity in the ICM significantly affects the interpretations of cosmological implications of galaxy clusters. The statistical model we develop will be important to understand the current and future results of observations.

Contents

1	Introduction	1
1.1	Motivation	1
1.2	Physical Modeling of Galaxy Clusters	1
1.3	Significance of Inhomogeneity to Cosmology using Galaxy Clusters	2
1.4	Observation of the Inhomogeneity in ICM	3
2	Review of Galaxy Clusters	5
2.1	Components of Galaxy Clusters	5
2.2	Intracluster Medium	9
2.2.1	Gas Density Profile	9
2.2.2	Gas Temperature Profile	11
2.2.3	Ionization Balance in the ICM	12
2.3	X-ray Emission	15
2.3.1	X-ray Line Emission	15
2.3.2	X-ray Continuum Emission	16
2.3.3	Temperature Measurement by the X-ray Spectroscopy	17
2.4	The Sunyaev-Zel'dovich Effect	18
3	Lognormal Model for Inhomogeneity in the ICM	21
3.1	Improvements in Physical Modeling of the ICM	21
3.2	Cosmological Hydrodynamic Simulation	21
3.3	Lognormal Distributions of Temperature and Density	24
3.4	Power Spectra of Density and Temperature Fluctuations	30
3.5	Summary	32
4	Temperature of Galaxy Clusters	33
4.1	Different Definitions of Cluster Temperature	33
4.2	Mock Observation of the Simulated Clusters	34
4.2.1	Spectroscopic-Like Temperature	37
4.3	Analytical Model	39
4.4	Comparison with Simulated Clusters	43
4.5	Mass-weighted Temperature	45
4.6	Summary	47

5	The Hubble Constant Measurement from the Sunyaev-Zel'dovich effect	49
5.1	Discrepancy between the Hubble Constant Estimates from Clusters and Other Observations	49
5.2	Estimating H_0 from the SZE in the Spherical Isothermal β Model	50
5.3	Analytic Modeling of Systematic Errors of H_0 for Spherical Clusters	51
5.4	Numerical Modeling of Systematic Errors of H_0 for Inhomogeneous and Triaxial Clusters	54
5.5	Comparison with Clusters from Cosmological Hydrodynamic Simulations	58
5.5.1	Results	58
5.5.2	Comparison with previous studies	60
5.6	Summary	61
6	Reconstructing 2D fluctuations from 2D observation	63
6.1	Complex Structure in X-ray Clusters	63
6.2	Synthetic Clusters	64
6.2.1	Method	64
6.2.2	Statistical Analysis of the Synthetic Clusters	67
6.2.3	Potential Systematics	71
6.3	Application to Abell 3667	75
6.3.1	Data Reduction	75
6.3.2	Analysis and Results	76
6.3.3	Implications	79
6.4	Comparison with the Simulated Clusters	79
6.5	Summary	81
7	Conclusions	85
A	Nature of the Lognormal Distribution	89
A.1	Probability Density Function, Expectation and Moment	89
A.2	The Bivariate Log-normal Function	91
A.3	Distribution of the Random Variable Squared	91
B	Density and Temperature Distributions on a Sphere of the Triaxial Model	93
C	Distribution of f_H for prolate and oblate ellipsoids	97
D	Relation of Density and Surface Brightness Distributions Under the Thick-slice Approximation	101
E	Effect of Poisson process to the observed surface brightness distribution	105

Chapter 1

Introduction

1.1 Motivation

Modern cosmology has established the cold dark matter (CDM) scenario of the Universe, which is supported by various observations, including the galaxy distribution, cosmic microwave background (CMB), and Type Ia supernova. In such a scenario, it is considered that galaxy clusters correspond to the largest halos which grow from peaks in the initial fluctuation of matter. Galaxy clusters are quite suitable for cosmological probes. For example, the cluster mass function is sensitive to the matter density, the dark energy density, and the mass fluctuation amplitude, and the Hubble constant, H_0 can be measured from the Sunyaev-Zel'dovich effect (SZE) and X-ray surface brightness. For these cosmological applications, the physical modeling of ICM plays an important role. Historically, it has been often assumed that the temperature is isothermal, and that the gas density distributes the spherically uniform distribution called the isothermal β model. However, recent results provided both observations and simulations with highly spatial resolution have made us vividly aware of the internal structures and a departure from the spherical-uniform approximation in galaxy cluster. The purpose of this thesis is to study the impact of such inhomogeneities on the cosmological applications. With this motivation, we explore the statistical nature of inhomogeneities on the basis of the cosmological hydrodynamic simulations and test the model directly against X-ray observations of a real cluster.

1.2 Physical Modeling of Galaxy Clusters

The physical modeling of galaxy clusters has a long history. There has been some interest in the member galaxies distributions from the early studies (e.g. Hubble, 1930; de Vaucouleurs, 1948; King, 1966). After the discovery of X-ray emission from clusters, ICM modeling also becomes important. Especially, the X-ray profile determined by proportional counters, such as Imaging Proportional Counter on *Einstein* satellite, was well approximated by the isothermal β model. This model is consistent with the empirical galaxy distribution called King model (King, 1966) and the assumption of the hydrostatic equilibrium. For the dark matter, Navarro et al. (1997) have proposed the universal profile using N-body simulations. Although we now know that the dark matter distribution is not universal in the central concentrations and the halo mass (e.g.

Avila-Reese et al., 1999; Jing, 2000; Jing & Suto, 2000; Fukushige et al., 2004), it remains quite useful for approximately describing the dark matter distributions. On the basis of the NFW dark matter profile and the hydrostatic equilibrium of ICM, an empirical β -model profile has been proposed (Makino et al., 1998; Suto et al., 1998).

All the models above mentioned assume a simple spherical approximation that physical quantity, such as gas density or temperature, can be determined by only one parameter, a radius from the cluster center. Triaxial approximation is one possibility of the physical modeling beyond the simple spherical model and have been studied by many authors (Lee & Shandarin, 1998; Sheth & Tormen, 1999; Jing & Suto, 2002; Lee & Suto, 2003, 2004; Kasun & Evrard, 2005). The physical model for the origin of the triaxial density profile has been proposed based on Zel'dovich approximation (Lee et al., 2005).

Despite an extensive list of the previous studies, no physical model has been proposed for the statistical nature of underlying inhomogeneities in the intra-cluster medium (ICM, hereafter). Given the high spatial resolutions achieved both in observations and simulations, such a modeling should play a vital role in improving our understanding of galaxy clusters, which we will attempt to do in this thesis. For this purpose, we use simulated clusters in cosmological hydrodynamic simulations to construct the inhomogeneity model. To model the inhomogeneity, we take a statistical approach (Kawahara et al., 2007). Having found that the small-scale density and temperature fluctuations approximately follow the lognormal distributions, we characterize the ICM inhomogeneities by the lognormal probability density function (PDF).

1.3 Significance of Inhomogeneity to Cosmology using Galaxy Clusters

By applying such a statistical model of inhomogeneity, we investigate two important cosmological applications of galaxy clusters. One is the bias of the cluster temperature. A cluster temperature is an important quantity for several cosmological parameter estimates. For example, mass-temperature relation which is physically motivated, is used to obtain the mass function of clusters and the mass fluctuation amplitude at $8h^{-1}\text{Mpc}$, σ_8 . In X-ray observations, the spectroscopic temperature, T_{spec} , is estimated by fitting the thermal continuum and the emission lines of the spectrum. In the presence of inhomogeneities in the ICM, the temperature so measured is inevitably an *averaged* quantity over a finite sky area and the line-of-sight. It has been conventionally assumed that T_{spec} is approximately equal to the emission-weighted temperature, T_{ew} . Mazzotta et al. (2004), however, have pointed out that T_{spec} is systematically lower than T_{ew} . The above bias in the cluster temperature should be properly taken into account when confronting observational data with theory in cosmological studies. As noted by Rasia et al. (2005), it can result in the offset in the mass-temperature relation of galaxy clusters. Shimizu et al. (2006) have studied its impact on the estimation of σ_8 . The authors perform the statistical analysis using the latest X-ray cluster sample and find that the systematic difference can thus shift σ_8 by ~ 0.15 . As shown in chapter 4, the simple spherical model does not explain this discrepancy. Therefore, we explore the origin of the bias in the spectroscopic temperature by taking account of inhomogeneity properly. We also construct an analytical model for the local ICM inhomogeneities that can simultaneously explain the systematic bias (Kawahara et al., 2007).

The other important application we consider in this thesis, is the Hubble constant measurement from the SZE and X-ray. The H_0 measurement using clusters is based on the distance to clusters. This method has the advantage of being able to obtain the distance without the cosmic distance ladder. Recent high-resolution X-ray and radio observations enable one to construct a statistical sample of clusters for the H_0 measurement. Carlstrom et al. (2002) compiled the previous results of 38 distance determination to 26 different galaxy clusters, and obtained $H_0 = 60 \pm 3 \text{ km s}^{-1} \text{ Mpc}^{-1}$ (Reese et al., 2002; Uzan et al., 2004). Despite its relatively large individual errors, the mean value of H_0 estimated from the SZE and X-ray appears systematically lower than those estimated with other methods: e.g. $H_0 = 72 \pm 8 \text{ km s}^{-1} \text{ Mpc}^{-1}$ from the distance to Cepheids (Freedman et al., 2001), and $H_0 = 73 \pm 3 \text{ km s}^{-1} \text{ Mpc}^{-1}$ from the CMB anisotropy (Spergel et al., 2007).

Possible systematic errors in the H_0 measurement from the SZE have been extensively studied by several authors (Inagaki et al., 1995; Kobayashi et al., 1996; Yoshikawa et al., 1998; Hughes & Birkinshaw, 1998; Birkinshaw, 1999; Wang & Fan, 2006); they have addressed a number of physical sources of possible biases including the finite extension, clumpiness, asphericity, and non-isothermality of the ICM. Nevertheless they were not able to identify any systematic error that affects the estimate of H_0 by 10-15 percent. Therefore it has been generally believed that the reliability of H_0 from the SZE is determined by the statistics. Given that, the 10-15 percent underestimate bias mentioned above, if real, needs to be explained in terms of additional ICM physics beyond the simple models used in previous studies. The Hubble constant measurement from the SZE and X-ray usually assumes the isothermal β model. Indeed, T_{spec} is adopted to a cluster temperature for this measurement. In chapter 5, we attempt to evaluate the systematic errors of the H_0 measurement taking account of the cluster temperature bias and the lognormal description of the ICM inhomogeneity (Kawahara et al., 2008a).

1.4 Observation of the Inhomogeneity in ICM

The lognormal model of the ICM inhomogeneity proposed in chapter 3 is motivated by clusters from cosmological hydrodynamic simulations. Therefore it is crucial to see if inhomogeneities in real galaxy clusters also show the lognormal signature. Fortunately, cluster images by X-ray satellites with high angular resolution telescope, such as *Chandra* and XMM-Newton, enable us to study the X-ray surface brightness fluctuation. Indeed, recent X-ray observations have unveiled various structures of ICM: complex temperature structure (e.g., Markevitch et al., 2000; Furusho et al., 2001), shock fronts (e.g., Jones et al., 2002), cold fronts (e.g., Markevitch et al., 2000), X-ray holes (e.g., Fabian et al., 2002), sound waves, (e.g., Fabian et al., 2006; Sanders & Fabian, 2008). X-ray surface brightness fluctuation in the core of Coma cluster has been discussed in the context of turbulence (Schuecker et al., 2004). Although individual structures seen in clusters have been interest to many authors, few studies have been carried out on the statistical properties of X-ray inhomogeneities. Because X-ray emission is essentially determined by gas density, X-ray surface brightness inhomogeneity has information of density fluctuation. We attempt to extract the statistical nature of the gas density inhomogeneity in chapter 6 (Kawahara et al., 2008b). In reality, this is not a straightforward task since one can observe clusters in X-rays only through their projection over the line of sight (LOS). The projection effect of inhomogeneity is

of concern in various cosmological and astronomical situations. Column density distributions of inhomogeneous interstellar medium have been investigated by several authors (Vázquez-Semadeni & García, 2001; Elmegreen, 2002; Fischera & Dopita, 2004). Projection of cosmological density field also have been studied in the context of galaxy distribution (e.g. Fry & Thomas, 1999; Zheng, 2004) and weak lensing (Taruya et al., 2002). There have been few works of the projection effect between X-ray fluctuation and density fluctuation. There are two significant difference between the previous studies of various projection and the case of X-ray fluctuation in ICM. One is X-ray emissivity is proportional to density squared, not density as the column density and galaxy number density. The other is X-ray distribution has the radial profiles. Thus, we develop a method of extracting statistical information of the three-dimensional properties of fluctuations from the two-dimensional X-ray surface brightness. Then, we apply the methods to real data of *Chandra* observation. To avoid the contamination of Poisson noise and the central cD galaxy, we choose Abell 3667 that has the best photon statistics of the cluster without the cooling core.

This thesis is organized as follows. Chapter 2 reviews a standard picture of galaxy clusters, including the simple spherical models, the X-ray emission mechanism, and the SZE. In chapter 3, we propose an inhomogeneity model of gas density and temperature by analyzing cosmological hydrodynamic simulation. Chapter 4 presents the application of the inhomogeneity model to the cluster temperature estimate. In chapter 5, we also apply our model to the Hubble constant measurement from the SZE and X-ray. In chapter 6, we test our model directly against X-ray observations of a real cluster. Chapter 7 summarizes our conclusions.

Chapter 2

Review of Galaxy Clusters

Galaxy clusters, just like it sounds, first were recognized as the regions containing hundreds of galaxies within a few Mpc (e.g., Abell, 1958). Now, we can also observe galaxy clusters by X-ray, the SZE, and the gravitational lensing. X-ray emission from galaxy clusters was first observed in the early 1970s (e.g., Gursky et al., 1971; Kellogg et al., 1971; Forman et al., 1972; Giacconi et al., 1972). Panels a and b in Figure 2.1 show the optical and the X-ray images of the same regions of a cluster, Abell 2218. As shown by these two images, the X-ray emission extends over the whole cluster. The thermal bremsstrahlung emission and the line emission of the hot plasma well explain the X-ray spectrum from clusters (Felten et al., 1966). These facts imply the presence of the ICM. It is very hot (typical temperature $T \sim 1 - 10$ keV) and diffuse (typical electron density $n \sim 10^{-5} - 10^{-3} \text{cm}^{-3}$) plasma. Although mass of the ICM is approximately a few - ten times larger than that of member galaxies, it cannot explain total mass of clusters. It is thus generally considered that large amount of non-baryonic matter called dark matter exists in clusters. The distorted images of member galaxies due to the strong and weak lensings as seen in Figure 2.1 c also support the presence of dark matter in clusters. In addition to optical and X-ray observations, recent progress of the radio astronomy enable us to see clusters by the SZE (Figure 2.1 d). The SZE is the spectrum distortion of the CMB due to the inverse Compton scattering of the CMB with the high energy electron in the ICM. At present, the SZE signals have been detected only near the center of clusters as displayed in Figure 2.1 d.

These observations give us much physical information on cluster components that becomes a basis for modeling of clusters. In this chapter, we will review a basic physics of the galaxy cluster. First, we discuss physical properties of components of the clusters (§2.1). Second, we introduce several important models of the ICM and the chemical state of the plasma in §2.2. Finally, we review the emission mechanism of X-ray and the SZE in §2.3 and 2.4, respectively.

2.1 Components of Galaxy Clusters

The assumption that clusters are dynamically relaxed or *virialized* is the most prominent approximation for understanding clusters. This assumption is based on the comparison between the Hubble time $t_H \sim H_0^{-1} \approx 10^{10}$ [yr] and dynamical timescales of the member galaxies and the ICM. The dynamical timescale of the member galaxies can be estimated by the crossing timescale

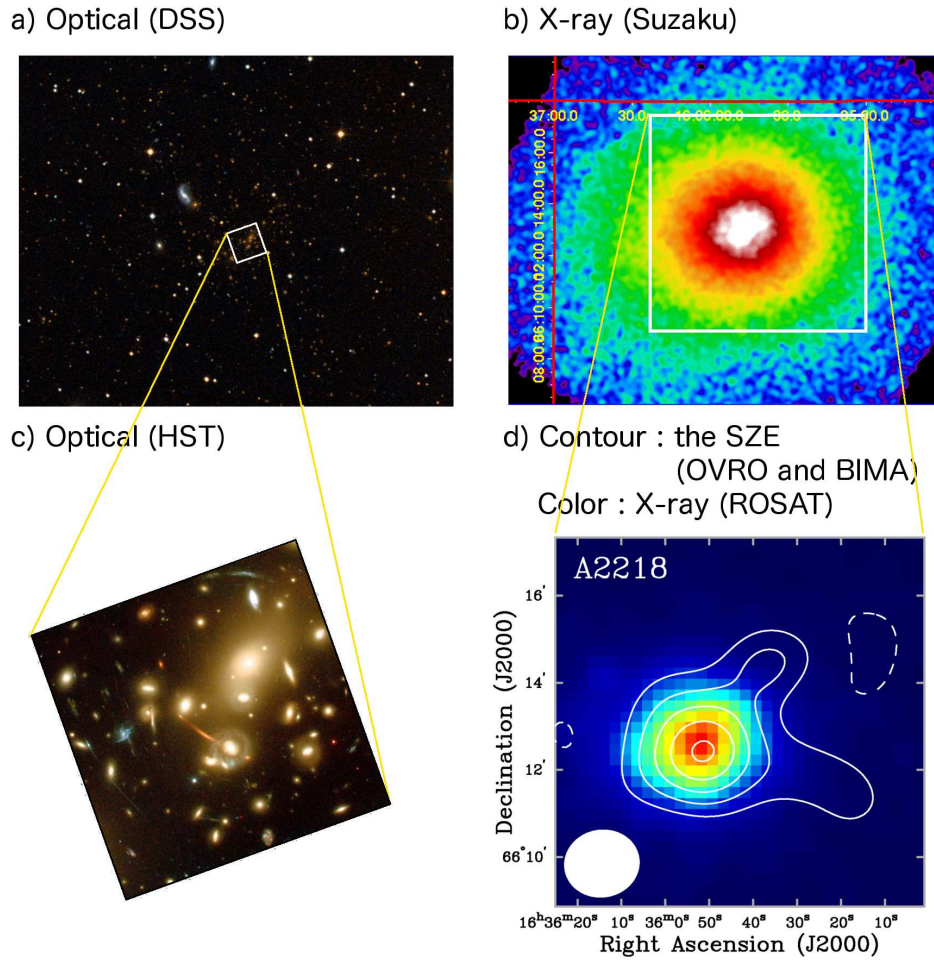


Figure 2.1: Optical, X-ray, and the SZE images of Abell 2218. The panel a displays the optical image provided by Digitized Sky Survey (<http://server1.sky-map.org>) . The deeper image of the center part of the cluster which is observed by Hubble Space Telescope is shown in the panel c. The panel b is X-ray distribution observed by Suzaku satellite (Takei et al., 2007). Note that the panels a and b have the same scale. The panel d shows the CMB temperature decrement by the SZE (contour) and X-ray (color scale) of the center region(Reese et al., 2002). Radio emissions were observed by Owens Valley Radio Observatory and Berkely-Illinois-Maryland Association. The X-ray counterpart was observed by ROSAT satellite.

expressed as

$$t_{\text{cr}} = \frac{R_{\text{cl}}}{\sigma_{\text{gal},r}} \approx 10^9 \left(\frac{\sigma_{\text{gal},r}}{10^3 \text{ km s}^{-1}} \right)^{-1} \left(\frac{R_{\text{cl}}}{1 \text{ Mpc}} \right) [\text{yr}], \quad (2.1)$$

where the typical cluster size R_{cl} is about a few Mpc and $\sigma_{\text{gal},r}$ is the radial velocity dispersion of the member galaxies. The typical value of $\sigma_{\text{gal},r}$ is approximately equal to one thousand km/s

which is estimated by the optical spectroscopy. Therefore, t_{cr} is a factor of a few to one order of magnitude smaller than t_{H} . For the ICM, gas pressure propagates with the sound velocity

$$c_s = \sqrt{\frac{\gamma_s k_B T_{\text{cl}}}{\mu m_p}}, \quad (2.2)$$

where m_p indicates the proton mass, k_B is the Boltzmann constant, $\mu \sim 0.6$ is the mean molecular weight, and γ_s is the specific heat ratio. Therefore, the dynamical timescale of the ICM can be estimated by the sound crossing timescale

$$\begin{aligned} t_{\text{sc}} &= \frac{R_{\text{cl}}}{c_s} \\ &\approx 7 \times 10^8 \left(\frac{T_{\text{cl}}}{10^8 \text{ K}} \right)^{-1/2} \left(\frac{R_{\text{cl}}}{1 \text{ Mpc}} \right) [\text{yr}]. \end{aligned} \quad (2.3)$$

Thus, the sound crossing timescale is also smaller than t_{H} .

On the assumption that clusters are in dynamical equilibrium, the total mass of clusters, M_{tot} can be roughly estimated by the virial theorem, $2K + U = 0$, where K and U are the total kinetic energy and the gravitational potential energy, respectively. The gravitational potential U is approximately equal to $\sum_i G m_i M_{\text{tot}} / R_{\text{cl}}$, where G indicates the gravitational constant and m_i is the mass of a test particle (total galaxy mass $\sum_i m_i = M_{\text{gal}}$ for galaxies or a mean mass of ions $\sum_i m_i = \mu N_p m_p$ for gas, where N_p is the total number of proton). Assuming the isotropic velocity dispersion, we obtain $\langle v^2 \rangle = 3\sigma_{\text{gal},r}^2$, or $2K = M_{\text{gal}} \langle v^2 \rangle = 3M_{\text{gal}} \sigma_{\text{gal},r}^2$. Then, M_{tot} is related to the galaxy velocity dispersion,

$$M_{\text{tot}} \approx \frac{3\sigma_{\text{gal},r}^2 R_{\text{cl}}}{G} \approx 7 \times 10^{14} M_{\odot} \left(\frac{\sigma_{\text{gal},r}}{10^3 \text{ km s}^{-1}} \right)^2 \left(\frac{R_{\text{cl}}}{1 \text{ Mpc}} \right). \quad (2.4)$$

We can also expect the virial relation between the gravitational potential and the temperature of the ICM ($2K = 3N_p k_B T_{\text{cl}}$),

$$M_{\text{tot}} \approx \frac{3k_B T_{\text{cl}} R_{\text{cl}}}{G \mu m_p} \approx 1 \times 10^{15} M_{\odot} \left(\frac{T_{\text{cl}}}{10 \text{ keV}} \right) \left(\frac{R_{\text{cl}}}{1 \text{ Mpc}} \right). \quad (2.5)$$

Developing the above discussion, more sophisticated measurements using the velocity dispersion and the cluster temperature are performed by many authors (e.g. Lewis et al., 1999). Moreover, the gravitational lensing directly gives the total mass of clusters (e.g. Tyson et al., 1990; Fahlman et al., 1994; Hoekstra et al., 1998). In these results, the typical total mass of clusters is $M_{\text{tot}} \sim 10^{15} M_{\odot}$.

The total galaxy mass M_{gal} in a cluster is estimated by the total luminosity of stars in the cluster, $L_{\text{tot}}^* \approx 10^{12-13} L_{\odot}^*$ typically, where $L_{\odot}^* = 3.8 \times 10^{33} \text{ erg s}^{-1}$ is the solar luminosity. Using the typical mass-to-light ratios of the individual galaxies ($m_{\text{gal}}/L_{\text{gal}}^* \approx 5(M_{\odot}/L_{\odot}^*)$), we can estimate the total galaxy mass,

$$M_{\text{gal}} \sim L_{\text{tot}}^* \left(\frac{m_{\text{gal}}}{L_{\text{gal}}^*} \right) \approx 5 \times 10^{12-13} M_{\odot}. \quad (2.6)$$

Although the total gas mass in the cluster can be estimated by the total X-ray luminosity, it is more complicated than the mass of galaxies because the luminosity is proportional to the density squared. Therefore, the radial distribution of the gas becomes important. The typical gas mass derived by the detail analysis is approximately

$$M_{\text{gas}} \approx 10^{14} M_{\odot}. \quad (2.7)$$

Because the sum of M_{gal} and M_{gas} is insufficient to explain M_{tot} , the remaining mass is thought to be the dark matter. The presence of the dark matter is also confirmed by various observation, such as the galactic rotation curve, velocities of globular clusters, and X-ray emission from elliptical galaxies (e.g. Trimble, 1987). Recently, a pair of clusters in the middle of collision was observed by both the X-ray and the gravitational lensing (Clowe et al., 2004). The difference of the mass and the X-ray distribution they showed is considered the direct evidence of the existence of the dark matter. We summarize the typical physical properties in Table 2.1.

Table 2.1: Typical physical properties of galaxy clusters.

Property	Typical value
Length	1 – 3 Mpc
Radial velocity dispersion of galaxy $\sigma_{\text{gal},r}$	10^3 km s^{-1}
Cluster temperature T_{cl}	3 – 10 keV
Total luminosity of stars L_{tot}^*	$10^{12} - 10^{13} L_{\odot}^*$
X-ray luminosity L_x	$10^{43} - 10^{46} \text{ erg s}^{-1}$
Total mass M_{tot}	$10^{15} M_{\odot}$
Galaxy mass M_{gal}	$10^{13} M_{\odot}$
Gas mass M_{gas}	$10^{14} M_{\odot}$

The spherical symmetry approximation is the most conventional to describe the physical quantities of clusters. Under the spherical approximation, the density distributions of the cluster components are expressed as a function of the radial distance r from the center: the gas density $\rho_{\text{gas}}(r)$, the dark matter density $\rho_{\text{dm}}(r)$, and the density of the member galaxies $\rho_{\text{gal}}(r) = m_{\text{gal}} n_{\text{gal}}(r)$. Then, The total mass within r is expressed as

$$\begin{aligned} M(r) &= 4\pi \int_0^r r^2 [\rho_{\text{dm}}(r) + \rho_{\text{gas}}(r) + m_{\text{gal}} n_{\text{gal}}(r)] dr \\ &\approx 4\pi \int_0^r r^2 \rho_{\text{dm}}(r) dr, \end{aligned} \quad (2.8)$$

where the second equation above assumes that the dark matter dominates the total mass. The gravitational potential $\Phi_{\text{G}}(r)$ is related to $M(r)$ as

$$\frac{d\Phi_{\text{G}}(r)}{dr} = -\frac{GM(r)}{r^2}. \quad (2.9)$$

There are many empirical models of the dark matter distribution. Here, we introduce the NFW profile based on the results of N-body simulations (Navarro et al., 1996, 1997).

$$\rho_{\text{dm}}(r) = \frac{\rho_{\text{dm}} r_s^3}{r(r + r_s^2)}, \quad (2.10)$$

where r_s and ρ_{dm} are free parameters. The total mass and the gravitational potential for the NFW model are obtained by

$$M(r) = 4\pi\rho_{\text{dm}}r_s^3 \left[\log\left(1 + \frac{r}{r_s}\right) - \frac{r}{r + r_s} \right] \quad (2.11)$$

$$\Phi_{\text{G}} = -4\pi G\rho_{\text{dm}}r_s^3 \frac{\log(1 + r/r_s)}{r}. \quad (2.12)$$

The hydrostatic equilibrium assumptions of each cluster component connects its distribution and the gravitational potential.

$$\frac{d}{dr} \left[\rho_{\text{gas}}(r) \frac{k_{\text{B}}T(r)}{\mu m_p} \right] = -\rho_{\text{gas}}(r) \frac{d\Phi_{\text{G}}(r)}{dr}, \quad (2.13)$$

$$\frac{d}{dr} [\rho_{\text{dm}}(r) \sigma_{\text{dm},r}(r)^2] = -\rho_{\text{dm}}(r) \frac{d\Phi_{\text{G}}(r)}{dr}, \quad (2.14)$$

$$\frac{d}{dr} [\rho_{\text{gal}}(r) \sigma_{\text{gal},r}(r)^2] = -\rho_{\text{gal}}(r) \frac{d\Phi_{\text{G}}(r)}{dr}. \quad (2.15)$$

2.2 Intracluster Medium

Several cosmological applications of clusters using X-ray and/or the SZE require the precise modeling of physical nature of the ICM. In this section, we review the fundamental model of the density and temperature distribution of the ICM and microscopic state of plasma. These provide the bottom line of interpretation of X-ray and the SZE observational data.

2.2.1 Gas Density Profile

The most popular model for the gas distribution is the β model (Cavaliere & Fusco-Femiano, 1976, 1978). The electron number density at a radius r of the β model is expressed as

$$n(r) = n_0 \left[1 + \left(\frac{r}{r_c} \right)^2 \right]^{-3\beta/2}, \quad (2.16)$$

where n_0 is the central electron number density, r_c is the core radius, and β is the beta index. Figure 2.2 demonstrates the shape of the β model.

Historically, the β model was first derived from relation of the density distributions of member galaxies and gas (Cavaliere & Fusco-Femiano, 1976, 1978). On the assumption that both the gas and the galaxies are isothermal, $T(r) = T_{\text{cl}}$ ($=$ constant) and $\sigma_{\text{gal},r}(r) = \sigma_{\text{gal},r}$ ($=$ const), equations

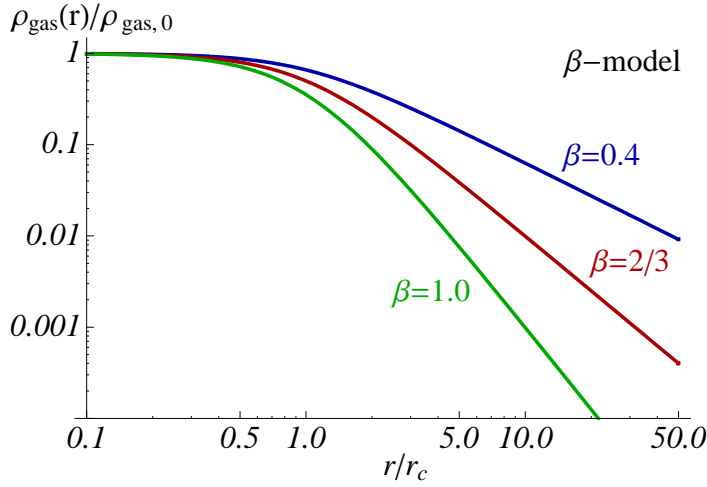


Figure 2.2: The shape of the β model. Each color indicates different value of β : $\beta = 0.4$ (blue), $2/3$ (red), and 1.0 (green).

(2.13) and (2.15) yield

$$\begin{aligned} \beta \frac{d}{dr} [\log \rho_{\text{gal}}(r)] &= \frac{d}{dr} [\log \rho_{\text{gas}}(r)], \\ \beta &\equiv \frac{\mu m_p \sigma_{\text{gal},r}^2}{k_B T} \end{aligned} \quad (2.17)$$

Then, $n(r) = \rho_{\text{gas}}(r)/\mu m_p \propto [\rho_{\text{gal}}(r)]^\beta$. By adopting $\rho_{\text{gal}}(r)$ by the phenomenological model of the galaxy distribution called the King model (King, 1962),

$$\rho_{\text{gal}}(r) = \rho_{\text{gal},0} \left[1 + \left(\frac{r}{r_c} \right)^2 \right]^{-3/2}, \quad (2.18)$$

where r_c is the core radius, we obtain the β model given by equation (2.16).

Combination of the hydrostatic assumption (Eq. [2.13]) and an isothermal assumption with the gravitational potential of the NFW model (Eq. [2.12]) provides another model of gas distribution (Makino et al., 1998; Suto et al., 1998), which is expressed as

$$\begin{aligned} \rho_{\text{gas}}(r) &= \rho'_{\text{gas},0} e^{-B} \left(1 + \frac{r}{r_s} \right)^{\frac{B r_s}{r}}, \\ B &\equiv 4\pi \rho_{\text{dm}} r_s^2 \frac{G \mu m_p}{k T_{\text{cl}}}. \end{aligned} \quad (2.19)$$

However, Makino et al. (1998) have found that the above model can be approximately well by

the β model. They provided the following fit,

$$\begin{aligned}\rho_{\text{gas}}(r) &\approx A\rho'_{\text{gas},0} \left[1 + \left(\frac{r}{r'_c} \right)^2 \right]^{-3\beta'/2}, \\ A &\approx -0.013 B + 0.982 \\ r'_c &\approx 0.22 r_s \\ \beta' &\approx 0.067 B.\end{aligned}\tag{2.20}$$

The fact that the above model is very close to the β model implies the β -model has been related to an empirical dark matter profile, the NFW model.

The β model with a temperature T_{cl} provides the X-ray surface brightness profile:

$$\begin{aligned}S_x(\theta) &= \frac{1}{4\pi(1+z)^4} \int_{-\infty}^{\infty} dl x_{\text{H}} n^2 [r'(l)] \Lambda_{\text{X}}(T_{\text{cl}}) \\ &= \frac{\Lambda_{\text{X}}(T_{\text{cl}}) x_{\text{H}} n_0^2 r_c G(\beta)}{4\pi(1+z)^4} \left[1 + \left(\frac{\theta}{\theta_c} \right)^2 \right]^{-3\beta + \frac{1}{2}} \\ r'(l) &\equiv \sqrt{l^2 + (d_A \theta)^2}\end{aligned}\tag{2.21}$$

where $\theta_c \equiv r_c/d_A$, $\Lambda_{\text{X}}(T_{\text{cl}})$ is the X-ray cooling function, x_{H} is the hydrogen mass fraction, and, we define

$$G(\beta) \equiv \sqrt{\pi} \frac{\Gamma(3\beta - 1/2)}{\Gamma(3\beta)}\tag{2.22}$$

with $\Gamma(x)$ being the gamma function.

The β model approximately explains the X-ray distribution in observation (e.g. Mohr et al., 1999) and the density distribution of the cosmological hydrodynamic simulated clusters (see §3.3). Although the β model was originally derived on the isothermal assumption, we regard the β model as the density profile described by equation (2.16) without any assumption of temperature distribution.

2.2.2 Gas Temperature Profile

Although the isothermal assumption is useful for the zero-th order approximation, in some situation, the temperature distribution becomes important. The radial temperature distribution have been investigated by many authors using both X-ray observations and the cosmological hydrodynamic simulations. We here introduce the temperature distribution models of the ICM commonly used. One is called the polytropic model. Combination the β model with the polytropic relation,

$$P \propto \rho^\gamma,\tag{2.23}$$

yields this model:

$$\begin{aligned}T(r) &= T_0 [n(r)/n_0]^{\gamma-1} \\ &= T_0 \left[1 + \left(\frac{r}{r_c} \right)^2 \right]^{-3\beta(\gamma-1)/2},\end{aligned}\tag{2.24}$$

where T_0 is the temperature at $r = 0$, and γ is the polytrope index (Markevitch et al., 1998). The typical range of γ is 1.1 – 1.2 given by the results of the cosmological hydrodynamic simulations (e.g. Lewis et al., 2000; Ascasibar et al., 2003; Borgani et al., 2004).

We also introduce the cooling cluster model including the central temperature decrement (Allen et al., 2001; Kaastra et al., 2004):

$$T(r) = T_l + (T_h - T_l) \frac{(r/r_c)^\mu}{1 + (r/r_c)^\mu}, \quad (2.25)$$

where T_l and T_h are the central temperature and the temperature at infinity, and μ determines the shape of the profile. A number of observed clusters exhibit such the decrement is known as cool core. Figure 2.3 displays the above two model assuming the typical set of values, $(T_h - T_l)/T_l = 1.5$ and $\mu = 2$. The β model is also shown for comparison. As shown in this figure, temperature profiles is quite shallower than the density one.

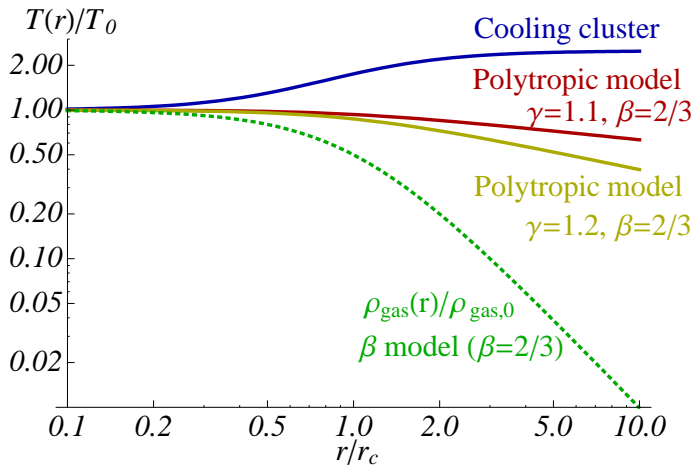


Figure 2.3: The shape of the polytropic model (Eq. [2.24]) with $\gamma = 1.1$ and 1.2, and that of the cooling cluster profile (Eq. [2.25]) with $(T_h - T_l)/T_l = 1.5$ and $\mu = 2$. The β model normalized by the central density is also displayed for comparison (dotted line).

2.2.3 Ionization Balance in the ICM

The dynamical balance between collisional ionization and recombination is called *collisional ionization equilibrium* (CIE). The process that an electron e^- collides an ion A^{i+} and strip out a bound electron is the most popular collisional ionization, which is called *direct collisional ionization*. Direct collisional ionization is the cooling process because the energy equal to the ionization potential of the atom, $\Delta E_{A^{i+}}$ is removed from the incoming electron. This process can be expressed as



Let us define the collisional ionization rate $R_{\text{coll}}^{\text{A},i}$ [$\text{cm}^{-3}\text{s}^{-1}$]. Because the collision frequency is proportional to both the number density of electron (n) and ion ($n_{\text{A},i}$), we can rewrite $R_{\text{coll}}^{\text{A},i}$ as

$$R_{\text{coll}}^{\text{A},i} = nn_{\text{A},i}\alpha_{\text{coll}}^{\text{A},i}. \quad (2.27)$$

Using the energy distribution of electron $\mathcal{F}(E)dE$ and the cross section σ_{coll} , $\alpha_{\text{coll}}^{\text{A},i}$ can be written as

$$\alpha_{\text{coll}}^{\text{A},i} = \int_{E_1}^{\infty} \sigma_{\text{coll}} \sqrt{\frac{2E}{m_e}} \mathcal{F}(E) dE, \quad (2.28)$$

where E_1 is the ionization potential.

Radiative recombination is a process that one electron is caught by an ion A^{i+} and a surplus energy release as light:



where A_* indicates the excited ion. This process produces the continuum radiation called recombination continuum since the energy of the incoming electron may take any value. Because the electron tends to be captured a state of large principle number and high angular momentum, the radiative cascade occur and many photons born. Finally, it returns to the ground state. The above process is expressed as

$$A_*^{(i-1)+} \rightarrow A^{(i-1)+} + h\nu_1 + h\nu_2 + h\nu_3 + \dots \quad (2.30)$$

These photons created by transitions between bound states produce *recombination lines*. In a similar way to the collisional ionization, the recombination rate is expressed as

$$R_{\text{rec}}^{\text{A},i} = nn_{\text{A},i+1}\alpha_{\text{rec}}^{\text{A},i}. \quad (2.31)$$

The collisional ionization equilibrium is the balance between three ions $A^{(i-1)+}$, $A^{(i)+}$, and $A^{(i+1)+}$ described as,

$$R_{\text{coll}}^{\text{A},i} + R_{\text{rec}}^{\text{A},i} = R_{\text{coll}}^{\text{A},i-1} + R_{\text{rec}}^{\text{A},i+1} \quad (i \geq 1). \quad (2.32)$$

However, for the neutral atom ($i=0$), the balance between collisional ionization and recombination involves $R_{\text{coll}}^{\text{A},0} = R_{\text{rec}}^{\text{A},1}$. Using this condition, equation (2.32) reduces to

$$R_{\text{coll}}^{\text{A},i} = R_{\text{rec}}^{\text{A},i+1} \quad (i \geq 0). \quad (2.33)$$

Therefore, we obtain very simple results for a ratio of density of two adjacent ions,

$$\frac{n_{\text{A},i+1}}{n_{\text{A},i}} = \frac{\alpha_{\text{coll}}^{\text{A},i}}{\alpha_{\text{rec}}^{\text{A},i+1}}. \quad (2.34)$$

Note that in the above discussion, we neglect the charge exchange reaction that the direct exchange of an electron between two ions.

Then, we plot the case of hydrogen to understand the ionization state in the ICM. Using the linear approximation of the hydrogen cross section, $\sigma_{\text{coll}}^{\text{H}} \sim \sigma_0(E - E_1)/E_1$ ($\sigma_0 \sim 10^{-16} \text{cm}^2$) and the assumption of the Maxwell distribution ($\mathcal{F}(E) = \mathcal{F}_M(E; T) \equiv \sqrt{E} \exp(-E/kT)$), equation (2.28) is rewritten as

$$\alpha_{\text{coll}}^{\text{A},i} = 2.5 \times 10^{-10} \sqrt{T_e} \left(1 + \frac{T_e}{8 \times 10^4}\right) \exp\left(-\frac{1.6 \times 10^5}{T_e}\right) [\text{cm}^3 \text{s}^{-1}], \quad (2.35)$$

where T_e is the electron temperature measured in kelvin. The recombination rate for hydrogen, the power law approximation of a formula based on an expansion of the Kramers-Gaunt factor Seaton (1958),

$$\alpha_{\text{rec}}^{\text{A},i} = 4.2 \times 10^{-13} \left(\frac{T_e}{10^4}\right)^{-0.72} [\text{cm}^3 \text{s}^{-1}], \quad (2.36)$$

can be used. Combining equations (2.35) and (2.36) with equation (2.34), the ionization rate of hydrogen is obtained by

$$\begin{aligned} \chi_{\text{H}}(T_e) &\equiv \frac{n_{\text{H}^+}}{n_{\text{H}}} = \frac{f_{\text{H}}(T_e)}{1 + f_{\text{H}}(T_e)} \\ f_{\text{H}}(T_e) &\equiv 0.8 T_e^{1.2} \left(1 + \frac{T_e}{8 \times 10^4}\right) \exp\left(-\frac{1.6 \times 10^5}{T_e}\right). \end{aligned} \quad (2.37)$$

The fact that $\chi_{\text{H}}(T_e = 1.4 \times 10^4 \text{ K}) \sim 0.5$ and $\chi_{\text{H}}(T_e = 2 \times 10^4 \text{ K}) \sim 0.98$ involves the hydrogens in the ICM ($T_e > 10^7 \text{ K}$) are almost ionized ($\sim 100\%$). It is important to emphasize the fact that the ionization rate of each ion under CIE, is only dependent to gas temperature.

We demonstrate ionization fractions of several ions in Figure 2.4. As shown in this figure, over the range of temperature of the ICM (typically 1 - 10 keV), hydrogen, helium and even oxygen are almost fully ionized. Helium-like iron (Fe XXV) and hydrogen-like iron (Fe XXVI) become outstanding in range of the ICM temperature and produce strong emission lines in X-ray spectrum.

The timescale of the CIE is approximately described by (e.g. Dopita & Sutherland, 2003)

$$t_{\text{CIE}} = \frac{1}{n(\alpha_{\text{rec}}^{\text{A},i} + \alpha_{\text{coll}}^{\text{A},i})}. \quad (2.38)$$

The CIE is good approximation if $t_{\text{CIE}} \ll t_{\text{cool}}$, where t_{cool} is the cooling timescale. Because the cooling of the ICM is dominated by the X-ray radiative cooling, t_{cool} is the ratio of an energy of a plasma, Q_X [erg/cm³] and the X-ray emissivity, $\varepsilon_X \equiv \dot{Q}_X$ [erg/s/cm³]. One can separate ε_X to the density dependent and the X-ray cooling function: $\varepsilon_X = nn_H \Lambda_X(T)$. We obtain

$$t_{\text{cool}} = \frac{Q_X}{\varepsilon_X} = \frac{3(n + n_I)k_B T}{2nn_H \Lambda_X(T)} \approx \frac{3k_B T}{n \Lambda_X(T)}, \quad (2.39)$$

where n_I is the total ion density. For iron and carbon, CIE is a good approximation for $T > 10^{5.5} \text{ K}$ and $T > 10^6 \text{ K}$, respectively. Thus, under high temperature ($T > 10^8 \text{ K}$) situation in the ICM, the CIE is excellent approximation for the ionization state.

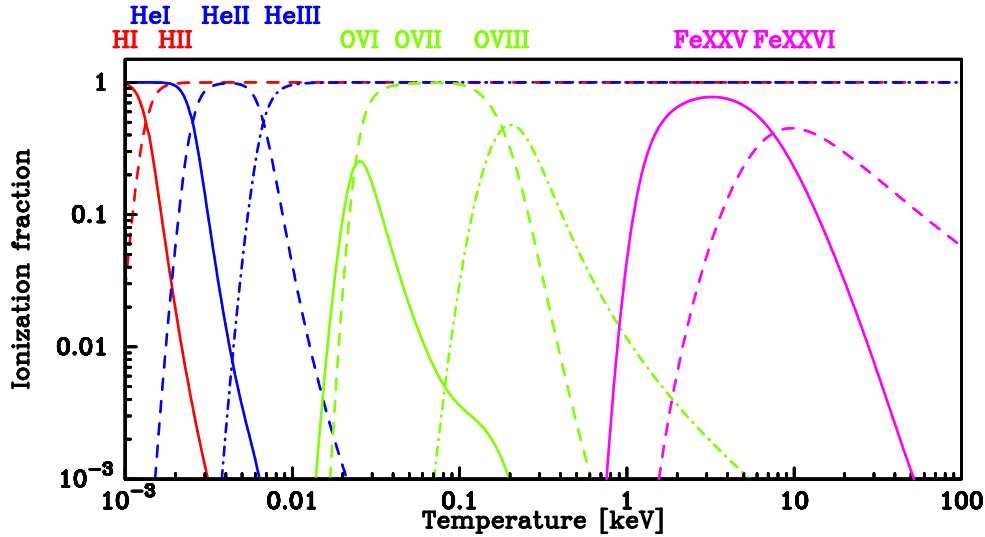


Figure 2.4: Ionization fraction as a function of temperature under the CIE. Red, blue, green, and magenta lines correspond to hydrogen, helium, oxygen, and iron ions, respectively. Each ionization fraction is calculated using SPEX 2.0 (Kaastra et al., 1996).

2.3 X-ray Emission

If one assumes that the ICM is isothermal, has a uniform metallicity, and satisfies the CIE condition, X-ray spectra from the ICM can be written as a combination of line and continuum emission processes. Figure 2.5 shows contributions of line and continuum emission processes to the bolometric cooling function. In temperature range of the ICM (1-10 keV), although continuum dominates the cooling function, the contribution of line emission is *not* negligible. In this section, we review both the line emission processes (§2.3.1) and the continuum emission process (§2.3.2).

2.3.1 X-ray Line Emission

The line emissions originate from the transition of an electron from a higher bound states to a lower bound states, so called bound-bound transition. Therefore, line emissions need the process that bring a bound electron up to an excited states. There are several such processes. First, the most important process under CIE is the excitation of a bound electron by the collision of a free electron (*collisional excitation*). The rate of the collisional excitation from the i -th state to the j -th state is given by

$$R_{ij} = nN_i \int_{E_{ij}}^{\infty} \sigma_{ij}(E) \sqrt{\frac{2E}{m_e}} \mathcal{F}_M(E; T) dE, \quad (2.40)$$

where N_i is the ion number density of the i -th state and E_{ij} is the energy gap between the two states. Second, Radiative recombination (Eq. [2.30]) also produces line emissions by cascade as seen in §2.2.3. Third and Fourth, inner-shell ionization and dielectric recombination also bring an electron to an excited states.

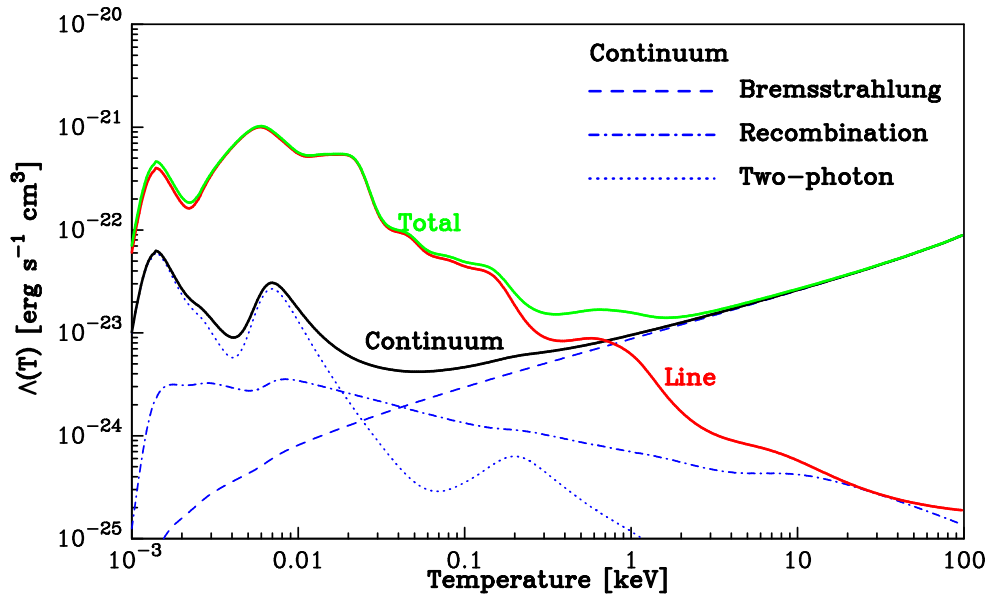


Figure 2.5: Bolometric cooling curve of thermal emission as a function of temperature under the CIE. Solid lines show the cooling function of the continuum emission (black), the line emission (red), and the total (green) emission. Dashed, dot-dashed, and dotted lines indicates the emissivity of three different continuum processes, corresponding to bremsstrahlung, recombination, and two-photon process, respectively. The cooling function of each process are calculated by MEKAL model (Mewe et al., 1985, 1986; Kaastra, 1992; Liedahl et al., 1995) using SPEX 2.0 (Kaastra et al., 1996). We assume the typical metallicity of the ICM, $Z = 0.3 Z_{\odot}$.

After brought up, an electron starts to fall to a lower state emitting photon. This photon with same energy of the energy gap makes the line emission. The radiative transition transition probability can be calculated by quantum mechanics.

2.3.2 X-ray Continuum Emission

Continuum emission mainly consists three emission processes, free-free (bremsstrahlung continuum), free-bound (recombination continuum), and two-photon. The contributions to the cooling function of these processes are shown in three blue lines in Figure 2.5. Under high temperature environment ($T_{cl} > 1$ keV), such as the ICM, the free-free process is the main component of the ICM emission, while the others less contribute to X-ray spectra.

The free-free process is the transition of a free electron between two free states caused by a collision to an ion. The most dominant X-ray continuum called *bremsstrahlung emission* arises from this process. The cross section of the free-free emission is expressed as (e.g. Rybicki & Lightman, 1979; Dopita & Sutherland, 2003)

$$d\sigma_{\text{ff}}(\nu) = \frac{16\pi}{3\sqrt{3}} \left(\frac{e^2}{\hbar c} \right)^3 Z^2 \frac{\hbar^2}{2m_e E_0} \frac{d(h\nu)}{h\nu} g_{\text{ff}}(\nu), \quad (2.41)$$

where $E_0 = m_e v_0^2/2$ is the kinetic energy of the free electron, and the Gaunt factor g_{ff} is the correction term between the result of the classical electrodynamics and that of the quantum mechanics. The energy emitted for the unit volume and the unit time is given by

$$W_{\text{em}}(\nu, E_0)d\nu = h\nu nn_H v_0 d\sigma_{\text{ff}}(\nu) = \frac{2^7 \pi^2}{3\sqrt{3}} \left(\frac{e^2}{\hbar c}\right)^3 Z^2 (nn_H a_0^3) E_{\text{Ry}}^{3/2} \sqrt{E_0} g_{\text{ff}}(\nu) d\nu, \quad (2.42)$$

where $a_0 \equiv \hbar^2/(m_e e^2)$ is the Bohr radius, and $E_{\text{Ry}} \equiv 2\pi^2 e^4 m_e / h^2$ is the Rydberg energy unit.

Under the assumption that the energy of electrons follows the Maxwell distribution, we obtain the emissivity from the gas with a single temperature T by averaging W_{em} with $\mathcal{F}_{\text{M}}(E)$.

$$\begin{aligned} \epsilon_{\text{ff}}(\nu, T) d\nu &= \frac{\int_{\hbar\nu}^{\infty} dE_0 \mathcal{F}_{\text{M}}(E_0; T) W_{\text{em}}(\nu, E_0) d\nu}{\int_0^{\infty} dE_0 \mathcal{F}_{\text{M}}(E_0; T)} \\ &= \frac{64\pi}{3\sqrt{3}} nn_H \left(\frac{\pi}{2k_{\text{B}} m_e^3}\right)^{1/2} \left(\frac{e^2}{c}\right)^3 \frac{\exp(-h\nu/k_{\text{B}}T)}{\sqrt{T}} Z^2 \langle g_{\text{ff}} \rangle d\nu. \end{aligned} \quad (2.43)$$

The cooling function of the thermal bremsstrahlung emission is given by integrating $\epsilon_{\text{ff}}(\nu, T)$ over ν :

$$\begin{aligned} \Lambda_{\text{brems}}(T) &= \int_0^{\infty} \epsilon_{\text{ff}}(\nu, T) / (nn_H) d\nu \\ &= \frac{16}{3\sqrt{3}} \left(\frac{2\pi k_{\text{B}}}{\hbar^3 m_e^3}\right)^{1/2} \sqrt{T} Z^2 G_{\text{ff}} \\ G_{\text{ff}} &\equiv \int_0^{\infty} e^{-u} \langle g_{\text{ff}} \rangle(u) du, \end{aligned} \quad (2.44)$$

where $u \equiv h\nu/(k_{\text{B}}T)$. The factor G_{ff} is the averaged Gaunt factor (Sutherland, 1999). Because G_{ff} is insensitive to temperature, Λ_{brems} is approximately proportional to \sqrt{T} .

Free-bound transitions is the capturing process of a free electron to a bound states. We have already introduce free-bound processes in §2.2.3 as the recombination continuum which arise from the process described in equation (2.29). The two-photon process is a spontaneous transition into a virtual level between the two quantum states (Breit & Teller, 1940). Two photons with energy E_1 and E_2 will be emitted such that $E_1 + E_2 = E_{\text{AB}}$, where E_{AB} is the energy gap between two states. In the temperature range of the ICM, two-photon processes have little contribution to the X-ray spectrum as shown in Figure 2.5.

2.3.3 Temperature Measurement by the X-ray Spectroscopy

On the assumption of the CIE, the spectrum from the thermal plasma is dependent on temperature and metallicity. We have already shown that the thermal bremsstrahlung spectrum approximately obeys $\exp(-E/k_{\text{B}}T)/\sqrt{T}$, which is the main component of the ICM spectra. It is also possible to calculate each line intensity from temperature and metallicity if assuming the CIE. In reality, the intrinsic spectrum $f_{\text{int}}(E)$ is distorted by the Galactic absorption. Then, the resulting spectrum $f(E)$ is expressed as

$$f(E) dE = \exp(-\sigma_{\text{gal}}(E) N_{\text{H}}) f_{\text{int}}(E) dE, \quad (2.45)$$

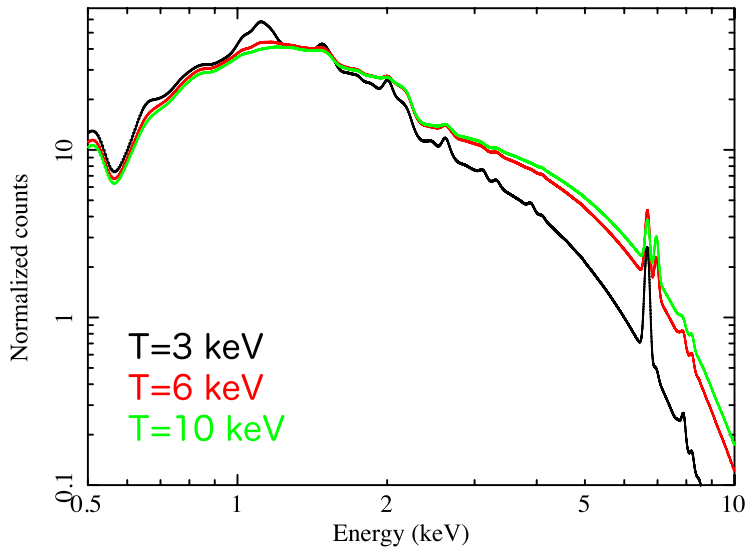


Figure 2.6: Example of X-ray spectra from the thermal plasma under the CIE. Each color indicates the different gas temperature : $T = 3$ keV (black), 6 keV (red), and 10.0 keV (green). These spectra are created by XSPEC *fakeit* command (Arnaud, 1996) assuming MEKAL model. The galactic absorption with $N_H = 3 \times 10^{20} \text{ cm}^{-2}$ and the response function of SUZAKU satellite are included.

where N_H is the column density of hydrogen and $\sigma_{gal}(E)$ is the absorption cross section. In addition, the detector response must be considered. Therefore, the spectroscopic temperature, T_{spec} , is measured by fitting the observed spectrum to the thermal plasma model with the Galactic absorption and the distortion by the detector response function. Figure 2.6 displays three model spectra from thermal plasma with different temperatures: $T = 3$ keV , 6 keV, and 10 keV.

We note that there are several useful models that calculate the thermal plasma spectra under the CIE:

- Raymond-Smith model (Raymond & Smith, 1977)
- MEKAL model (Mewe et al., 1985, 1986; Kaastra, 1992; Liedahl et al., 1995)
- APEC model (Smith et al., 2001)

In this thesis, we use MEKAL as the thermal plasma model under the CIE.

2.4 The Sunyaev-Zel'dovich Effect

A photon originated from CMB gets the energy by the inverse Compton scattering with high energy electrons in the ICM when passing through the cluster. The SZE is a spectral distortion of the CMB spectrum by this process (Sunyaev & Zeldovich, 1970, 1972).

Let us denote the energy distribution of CMB $\mathcal{F}_\nu(\nu, t)$ as a function of the frequency ν . The initial distribution before passing through the cluster obeys the Planck distribution,

$$\mathcal{F}_\nu(t=0) = \left[\exp\left(\frac{h\nu}{k_B T_{\text{CMB}}}\right) - 1 \right]^{-1}, \quad (2.46)$$

where $T_{\text{CMB}} (\approx 2.7 \text{ K})$ is the CMB temperature. The evolution equation of the energy distribution during passing through the cluster is provided by a non-relativistic Fokker-Planck approximation to the exact kinetic equation called the Kompaneets equation (Kompaneets, 1957),

$$\frac{\partial \mathcal{F}_\nu(t)}{\partial t} = n\sigma_{\text{T}}c \left(\frac{k_B T_e}{m_e c^2}\right) \frac{1}{\nu^2} \frac{\partial}{\partial \nu} \left\{ \nu^4 \frac{\partial \mathcal{F}_\nu(t)}{\partial \nu} + \nu^3 \left(\frac{h\nu}{k_B T_e}\right) \mathcal{F}_\nu(t) [\mathcal{F}_\nu(t) + 1] \right\}, \quad (2.47)$$

where T_e and m_e is the electron temperature and mass, respectively. The first term of the right hand is much larger than the second one because $h\nu \ll k_B T_e$. Ignoring the second term, the equation (2.47) reduces to

$$\begin{aligned} \frac{\partial \mathcal{F}_x(y)}{\partial y} &= \frac{1}{x^2} \frac{\partial}{\partial x} \left(x^4 \frac{\partial \mathcal{F}_x(y)}{\partial x} \right) \\ x &\equiv \frac{h\nu}{k_B T_{\text{CMB}}}; \quad y \equiv \int_0^t n\sigma_{\text{T}} \frac{k_B T_e}{m_e c^2} c dt, \end{aligned} \quad (2.48)$$

where we assume $T_e \gg T_{\text{CMB}}$, y is the Compton y -parameter. The initial spectrum (Eq. [2.46]) is rewritten by $\mathcal{F}_x(0) = (e^x - 1)^{-1}$. Then, the distortion of the energy distribution is calculated by the Taylor expansion.

$$\begin{aligned} \Delta \mathcal{F}_x &\equiv \mathcal{F}_x(y) - \mathcal{F}_x(0) \approx \left[\frac{\partial \mathcal{F}_x(y)}{\partial y} \Big|_{y=0} \right] y \\ &= \frac{y}{x^2} \frac{\partial}{\partial x} \left(x^4 \frac{\partial \mathcal{F}_x(0)}{\partial x} \right) \\ &= \frac{y x e^x}{(e^x - 1)^2} \left[x \coth\left(\frac{x}{2}\right) - 4 \right]. \end{aligned} \quad (2.49)$$

Then, the change of the spectral intensity is

$$\begin{aligned} \Delta I &= i_0 y g(x) \\ g(x) &\equiv \frac{x^4 e^x}{(e^x - 1)^2} \left[x \coth\left(\frac{x}{2}\right) - 4 \right]. \\ i_0 &\equiv 2 \frac{(k_B T_{\text{CMB}})^3}{(hc)^2}. \end{aligned} \quad (2.50)$$

Figure 2.7 shows the spectrum distortion by the SZE (left) and $\Delta I_\nu / (i_0 y)$ (right). As shown in Figure 2.7, the intensity is diminished (amplified) in the lower (upper) side of a particular frequency $\nu_c \approx 218 \text{ GHz}$ which satisfies $g(h\nu_c / k_B T_{\text{CMB}}) = 0$. On the Rayleigh-Jeans approximation $x \rightarrow 0$, the relative intensity change is directly proportional to y :

$$\begin{aligned} \frac{\Delta I}{I} &= \frac{i_0 y g(x)}{i_0 x^3 \mathcal{F}_x(0)} = \frac{y x e^x}{(e^x - 1)} \left[x \coth\left(\frac{x}{2}\right) - 4 \right] \\ &= -2y \quad (\text{if } x \rightarrow 0). \end{aligned} \quad (2.51)$$

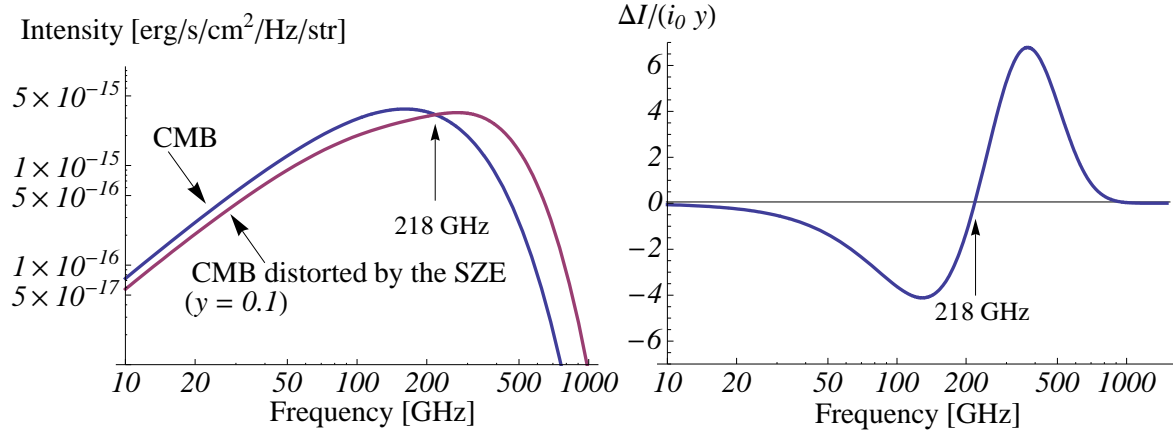


Figure 2.7: Distortion of the CMB spectrum by the SZE (left panel). Blue and red lines are undistorted and distorted spectrum by the SZE. To demonstrate the effect, we set $y = 0.1$. This value is about 1000 times larger than that of a typical massive cluster. Right panel shows $\Delta/(i_0 y)$ as a function of frequency.

For the β model (Eq. [2.16]), the radial profile of the y -parameter is obtained as

$$\begin{aligned}
 y(\theta) &= \frac{k_B \sigma_T}{m_e c^2} \int_{-\infty}^{\infty} dl n[r'(l)] T[r'(l)] \\
 &= \frac{n_0 \sigma_T k_B T_{cl} r_c G(\beta/2)}{m_e c^2} \left[1 + \left(\frac{\theta}{\theta_c} \right)^2 \right]^{-(3/2)\beta + \frac{1}{2}} \\
 r'(l) &\equiv \sqrt{l^2 + (d_A \theta)^2}.
 \end{aligned} \tag{2.52}$$

Considering current observations of the SZE (e.g. see Figure 2.1), in particular, y -parameter at the center

$$y(0) = \frac{n_0 \sigma_T k_B T_{cl} r_c G(\beta/2)}{m_e c^2}, \tag{2.53}$$

is important quantity for cosmological applications.

In the above discussion, we neglected the relativistic effect and the multiple scattering. The relativistic correction is important for high temperature clusters ($T_{cl} = 10 - 20$ keV), and have been studied by many authors (e.g. Rephaeli, 1995; Itoh et al., 1998; Nozawa et al., 1998; Sazonov & Sunyaev, 1998; Nozawa et al., 1998). Itoh et al. (2001) have studied the effect of the multiple scattering. They concluded that the contribution is safely neglected for the observed galaxy clusters.

Chapter 3

Lognormal Model for Inhomogeneity in the ICM

3.1 Improvements in Physical Modeling of the ICM

Recent progress both in numerical simulations and observations has improved physical modeling of the ICM beyond a simple isothermal and spherical approximation for a variety of astrophysical and cosmological applications such as the temperature profile (e.g. Markevitch et al., 1998; Allen et al., 2001, see §2.2.2) and non-spherical effects (e.g. Lee & Suto, 2003, 2004). However, no physical model has been proposed for the statistical nature of underlying inhomogeneities in the ICM. In this chapter, we explore the nature of the density and temperature inhomogeneity of the ICM using cosmological hydrodynamic simulations. The aim of this chapter is to establish the model of inhomogeneities based on the analysis of clusters in the cosmological hydrodynamic simulations. The lognormal model proposed in this chapter provides the basis of this thesis.

3.2 Cosmological Hydrodynamic Simulation

The results presented in this section have been obtained by using the final output of the Smoothing Particle Hydrodynamic (SPH) simulation of the local universe performed by Dolag et al. (2005). The initial conditions were similar to those adopted by Mathis et al. (2002) in their study (based on a pure N-body simulation) of structure formation in the local universe. The simulation assumes a spatially-flat Λ cold dark matter (Λ CDM) universe with $\Omega_0 = 0.3$, $h = H_0/100 \text{ km s}^{-1} \text{ Mpc}^{-1} = 0.7$, an rms density fluctuation amplitude $\sigma_8 = 0.9$ and $\Omega_b = 0.04$. The numbers of dark matter and SPH particles are ~ 50 million each within a high-resolution sphere of radius ~ 110 Mpc, which is embedded in a periodic box of ~ 343 Mpc on a side that is filled with nearly 7 million low-resolution dark matter particles. The simulation is designed to reproduce the matter distribution of the local universe by adopting initial conditions based on the Infrared Astronomical Satellite (IRAS) galaxy distribution smoothed on a scale of 7 Mpc (see Mathis et al., 2002, for detail).

The run has been carried out with GADGET-2 (Springel, 2005), a new version of the parallel Tree-SPH simulation code GADGET (Springel et al., 2001). The code uses an entropy-conserving

formulation of SPH (Mathis et al., 2002), and allows a treatment of radiative cooling, heating by a UV background, and star formation and feedback processes. The latter is based on a sub-resolution model for the multiphase structure of the interstellar medium (Springel & Hernquist, 2003); in short, each SPH particle is assumed to represent a two-phase fluid consisting of cold clouds and ambient hot gas.

The code also follows the pattern of metal production from the past history of cosmic star formation (Tornatore et al., 2004). This is done by computing the contributions from both Type-II and Type-Ia supernovae and energy feedback and metals are released gradually in time, accordingly to the appropriate lifetimes of the different stellar populations. This treatment also includes in a self-consistent way the dependence of the gas cooling on the local metallicity. The feedback scheme assumes a Salpeter IMF (Salpeter, 1955) and its parameters have been fixed to get a wind velocity of $\approx 480 \text{ km s}^{-1}$. In a typical massive cluster the SNe (II and Ia) add to the ICM as feedback $\approx 2 \text{ keV}$ per particle in an Hubble time (assuming a cosmological mixture of H and He); ≈ 25 per cent of this energy goes into winds. A more detailed discussion of cluster properties and metal distribution within the ICM as resulting in simulations including the metal enrichment feedback scheme can be found in Tornatore et al. (2004). The simulation provides the metallicities of the six different species for each SPH particle.

The gravitational force resolution (i.e. the comoving softening length) of the simulations has been fixed to be 14 kpc (Plummer-equivalent), which is comparable to the inter-particle separation reached by the SPH particles in the dense centers of our simulated galaxy clusters.

Among the most massive clusters formed within the simulation we extracted six mock galaxy clusters, contrived to resemble A3627, Hydra, Perseus, Virgo, Coma, and Centaurus, respectively. We choose the six massive clusters identified as Coma, Perseus, Virgo, Centaurus, A3627, and Hydra. Figure 3.1 shows projected surface density maps of these simulated clusters. Table 3.1 lists the observed and simulated values of the total mass and the radius of these clusters.

First, we extract a $3h^{-1}$ Mpc cubic region around the center of a simulated cluster and divide it into 256^3 cells so that the size of each cell is approximately equal to the gravitational softening length mentioned above. The center of each cluster is assigned so that the center of a sphere with radius $1h^{-1}$ Mpc lies at the center of mass of dark matter and baryon within the sphere.

The gas density and temperature of each mesh point (labeled by I) are calculated using the SPH particles as

$$\rho_I = \sum_{i=1}^{N_{gas}} m_i W_s(|\mathbf{r}_I - \mathbf{r}_i|, h_i), \quad (3.1)$$

$$T_I = \sum_{i=1}^{N_{gas}} \frac{m_i T_i}{\rho_i} W_s(|\mathbf{r}_I - \mathbf{r}_i|, h_i), \quad (3.2)$$

where \mathbf{r}_I is the position of the mesh point, W_s denotes the smoothing kernel, and m_i , \mathbf{r}_i , h_i , T_i , and ρ_i are the mass associated with the hot phase, position, smoothing length, temperature, and density associated with the hot gas phase of the i -th SPH particle, respectively. We adopt the

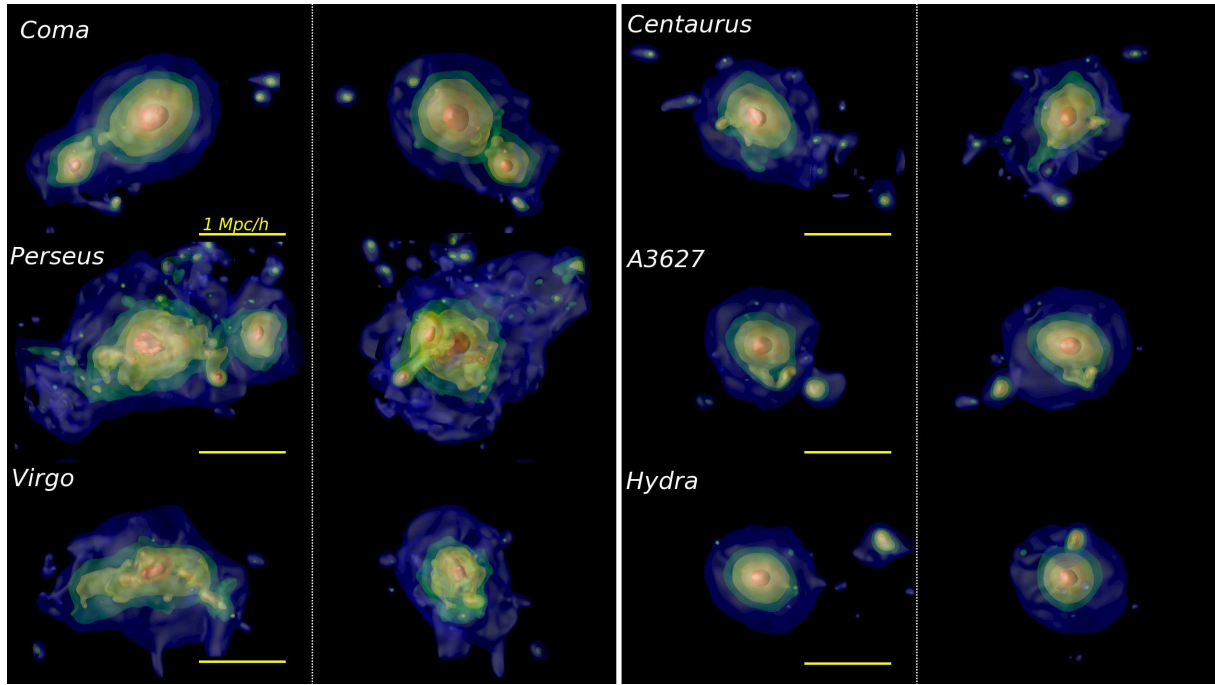


Figure 3.1: Projected surface density maps of the six simulated clusters. Five different ($n_e = 3 \times 10^{-3}, 1 \times 10^{-3}, 5 \times 10^{-4}, 3 \times 10^{-4},$ and 1×10^{-4} [cm^{-3}]) isodensity surfaces are indicated with different colors (red, orange, yellow, green, and blue, respectively). The left panels of each cluster indicate the view from our galaxy. The right panels are the projection of each simulated cluster as seen by a distant observer located to the “right” of each panel on the left. The horizontal yellow lines indicate the physical size of $1 h^{-1} \text{Mpc}$.

smoothing kernel:

$$W_s(|\mathbf{r}_I - \mathbf{r}_i|, h_i) = \frac{1}{\pi h_i^3} \begin{cases} 1 - (3/2)u^2 + (3/4)u^3 & \text{if } 0 \leq u \leq 1 \\ (2 - u)^3/4 & \text{if } 1 \leq u \leq 2 \\ 0 & \text{otherwise,} \end{cases} \quad (3.3)$$

where $u \equiv |\mathbf{r}_I - \mathbf{r}_i|/h_i$.

It should be noted that the current implementation of the SPH simulation results in a small fraction of SPH particles that have unphysical temperatures and densities. This is shown in the temperature – density scatter plot of Figure 3.2. The red points correspond to SPH particles that should be sufficiently cooled, but not here because of the limited resolution of the simulation. Thus if they satisfy the Jean criterion,

$$h_i > \frac{c_s}{\sqrt{\pi G \rho_i}}, \quad (3.4)$$

where c_s is the sound speed, and the criterion

$$\rho_i > 100 \bar{\rho}_b, \quad (3.5)$$

Table 3.1: Properties of the six simulated clusters and observed clusters.

Simulation							
	A3627	Hydra	Perseus	Virgo	Coma	Centaurus	
$M_{200}[10^{14}h^{-1}M_{\odot}]$	2.2	1.8	6.7	3.1	4.3	2.5	
$r_{200} [h^{-1} \text{ Mpc}]$	1.1	1.0	1.6	1.2	1.4	1.1	
β	0.69	0.70	0.64	0.60	0.74	0.69	
γ	1.15	1.22	1.09	1.15	1.17	1.17	
$\sigma_{\text{LN}, T}$	0.159	0.133	0.316	0.286	0.159	0.178	
$\sigma_{\text{LN}, n}$	0.240	0.180	0.518	0.446	0.434	0.239	
Observation							
	A3627	Hydra	Perseus	Virgo	Coma	Centaurus	Ref
$M_{200}[10^{14}h^{-1}M_{\odot}]$	*4.6 ^{+0.81} _{-0.58}	1.90 ^{+0.38} _{-0.33}	9.08 ^{+2.13} _{-1.52}	2.04 ^{+0.28} _{-0.21}	4.97 ^{+0.68} _{-0.57}	6.97 ^{+1.22} _{-1.25}	1,*2
$r_{200} [h^{-1} \text{ Mpc}]$	*1.26	1.22	2.05	1.26	1.64	0.89	1,*2
$T_{\text{spec}} [\text{keV}]$	5.62 ^{+0.12} _{-0.11}	3.82 ^{+0.20} _{-0.17}	6.42 ^{+0.06} _{-0.06}	† 2.5 ^{+0.04} _{-0.05}	8.07 ^{+0.29} _{-0.27}	3.69 ^{+0.05} _{-0.04}	3,†4
$N_{\text{H}} [10^{20}\text{cm}^{-2}]$	21.7	4.79	13.9	2.58	0.93	8.1	5

References.–(1)Girardi et al. (1998);(2)Reiprich & Böhringer (2002a);(3)Ikebe et al. (2002);
(4)Shibata et al. (2001);(5)Dickey & Lockman (1990)

they should be regarded as simply cold clumps without retaining the hot gas nature (see section 2.2 of Yoshikawa et al. (2001) for a detailed description).

In contrast, the blue points represent the SPH particles that have experienced the cooling catastrophe, and have significantly high cold gas fraction (larger than 10 percent). In either case, they are not supposed to contribute the X-ray emission and the SZE. Thus we remove their spurious contribution to the X-ray emission, the temperature estimate of the ICM and the SZE throughout the thesis. Specifically we follow Borgani et al. (2004), and exclude particles (red points) with $T_i < 3 \times 10^4 \text{K}$ and $\rho_i > 500\rho_c\Omega_b$, where ρ_c is the critical density, and particles (blue points) with more than ten percent mass fraction of the cold phase. While the total mass of the excluded particles is very small ($\sim 1\%$), they occupy a specific region in the ρ - T plane and leave some spurious signal due to high density, in particular for blue points.

3.3 Lognormal Distributions of Temperature and Density

Since clusters in general exhibit inhomogeneities over various scales, we begin with segregating the large-scale gradient and the small-scale fluctuations of the gas density and temperature.

For the large-scale gradient, we use the azimuthally-averaged radial profile of the gas temperature and density shown in Figure 3.3. We divide the simulated clusters into spherical shells with a width of $67h^{-1} \text{ kpc}$ and calculate the average temperature $\bar{T}(r)$ and density $\bar{n}(r)$ in each shell.

The density profile $\bar{n}(r)$ and the temperature profile $\bar{T}(r)$ are fitted to the conventional β model (Eq. [2.16]) and the polytropic model (Eq. [2.24]), respectively. The simulated profiles

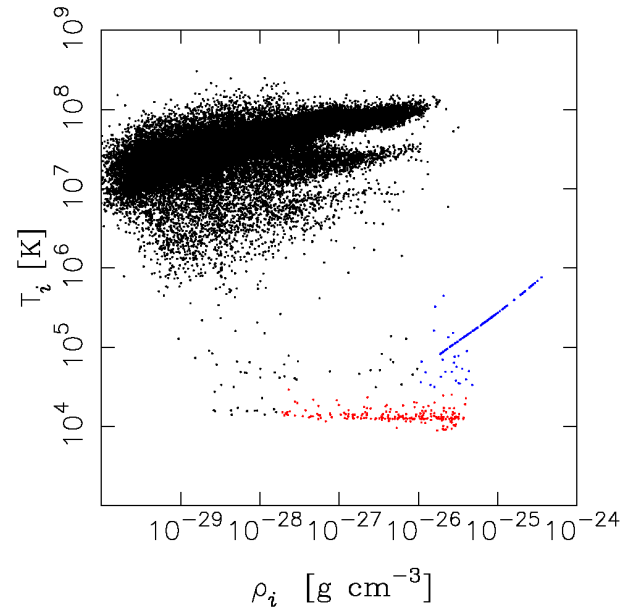


Figure 3.2: Scatter plots of temperatures and densities of SPH particles. Red and blue points indicate particles with unphysical temperatures and densities which are removed in computing the X-ray emission.

show reasonable agreement with the above models. The best-fit values of β and γ are listed in Table 3.1. The range of γ is approximately 1.1-1.2.

In addition to their radial gradients, the gas density and temperature have small-scale fluctuations. Figure 3.4 illustrates the distributions of the gas density and temperature in each radial shell normalized by their averaged quantities, \bar{T} and \bar{n} , respectively. Despite some variations among different shells, we find a striking similarity in the overall shape of the distributions. They approximately follow the lognormal distribution given by

$$P_{\text{LN}}(\delta_x; \sigma_{\text{LN},x}) d\delta_x = \frac{1}{\sqrt{2\pi}\sigma_{\text{LN},x}} \exp \left[-\frac{\left(\log \delta_x + \sigma_{\text{LN},x}^2/2\right)^2}{2\sigma_{\text{LN},x}^2} \right] \frac{d\delta_x}{\delta_x}, \quad (3.6)$$

where $\delta_x \equiv x/\bar{x}$ and x denotes T or n ($\delta_T \equiv T/\bar{T}, \delta_n \equiv n/\bar{n}$). In Appendix A, we summarize the statistical properties of the lognormal distribution. For simplicity, we neglect the variations among different shells and fit the distribution for the whole cluster within r_{200} (solid line) by the above equation (dashed line). The best-fit values of $\sigma_{\text{LN},T}$ and $\sigma_{\text{LN},n}$ are listed in Table 3.1.

Although the mesh size ($d_{\text{mesh}} = 3 \text{ h}^{-1} \text{ Mpc}/256 \approx 12 \text{ h}^{-1} \text{ kpc}$) we choose is comparable to the inter-particle separation reached by the SPH particles in the dense centers of our simulated galaxy clusters, we check the validity of our selection of the mesh size. Figure 3.5 shows the distributions through the mesh points of within $r = r_{200}$ for different selections of the mesh size, $d_{\text{mesh}} \approx 12 \text{ kpc/h}$ (solid line) and 24 kpc/h (dashed line). Because these distributions are almost identical, the mesh size we choose is reasonable.

By artificially smoothing the density and temperature fields, we investigate the scale dependence of fluctuations. For the smoothing function, we choose the three-dimensional Gaussian filter with the standard deviation σ . Figure 3.6 shows the distributions of fluctuations for the smoothed temperature and density fields. The distributions for $\sigma \geq 0.1 \text{ Mpc/h}$ become steeper than that without smoothing ($\sigma = 0 \text{ Mpc/h}$). Therefore, the fluctuations with a scale larger than $\sim 0.1 \text{ Mpc}$ dominate the PDF for the simulated clusters.

We also investigate the correlation of δ_T and δ_n . We pick up two clusters, ‘‘Hydra’’ and ‘‘Perseus’’, which show the most uncorrelated and the most correlated clusters, respectively. Figure 3.7 shows the contours of the joint distribution of $\delta_T = T(\mathbf{r})/\bar{T}(r)$ and $\delta_n = n(\mathbf{r})/\bar{n}(r)$ for all the mesh points within r_{200} for these clusters, together with that expected from the model assuming the joint PDF, $P(\delta_n, \delta_T) = P_{\text{LN}}(\delta_n)P_{\text{LN}}(\delta_T)$. For the log-normal distributions, $P_{\text{LN}}(\delta_n)$ and $P_{\text{LN}}(\delta_T)$, we have used the fits shown as the dashed line in Figure 3.4. The joint distribution agrees well with the model for both cases, while the deviation is somewhat larger in ‘‘Perseus’’ for which the model gives poorer fits to the underlying temperature and density distribution in Figure 3.4. If the cluster is spherically symmetric and the ICM is in hydrostatic equilibrium, we expect that n are correlated with T as $\delta_n \delta_T = 1$. We do not find such correlations in Figure 3.7.

The small-scale fluctuations mentioned above are not likely an artifact of the SPH scheme. We apply the similar analysis to the data of grid-based simulations (D.Ryu, private communication). The simulation assumes a spatially-flat Λ CDM universe with $\Omega_0 = 0.27$, $h = H_0/100 \text{ km s}^{-1} \text{ Mpc}^{-1} = 0.7$, an rms density fluctuation amplitude $\sigma_8 = 1.2$ and $\Omega_b = 0.043$. The spatial resolution (195.3 kpc/h) of the grid-based simulation is worse than that of the SPH

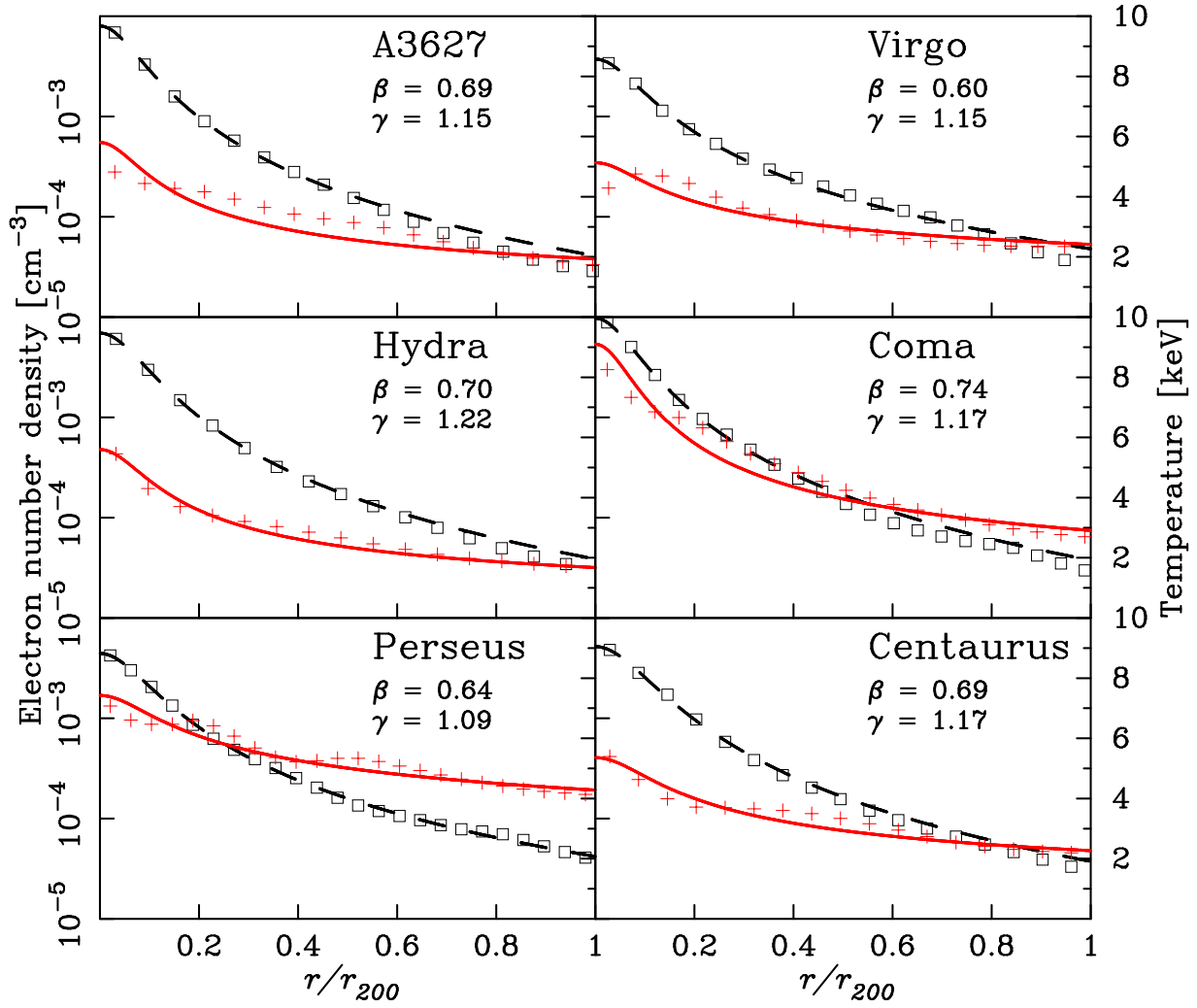


Figure 3.3: The radial profile of simulated clusters. Square provides the (electron number) density profile and dashed line is its fitting line assuming the β model. Plus shows the temperature profile and solid line is its fitting line assuming the polytropic model. Each square and plus point corresponds to the shell with a width of $67h^{-1}$ kpc.

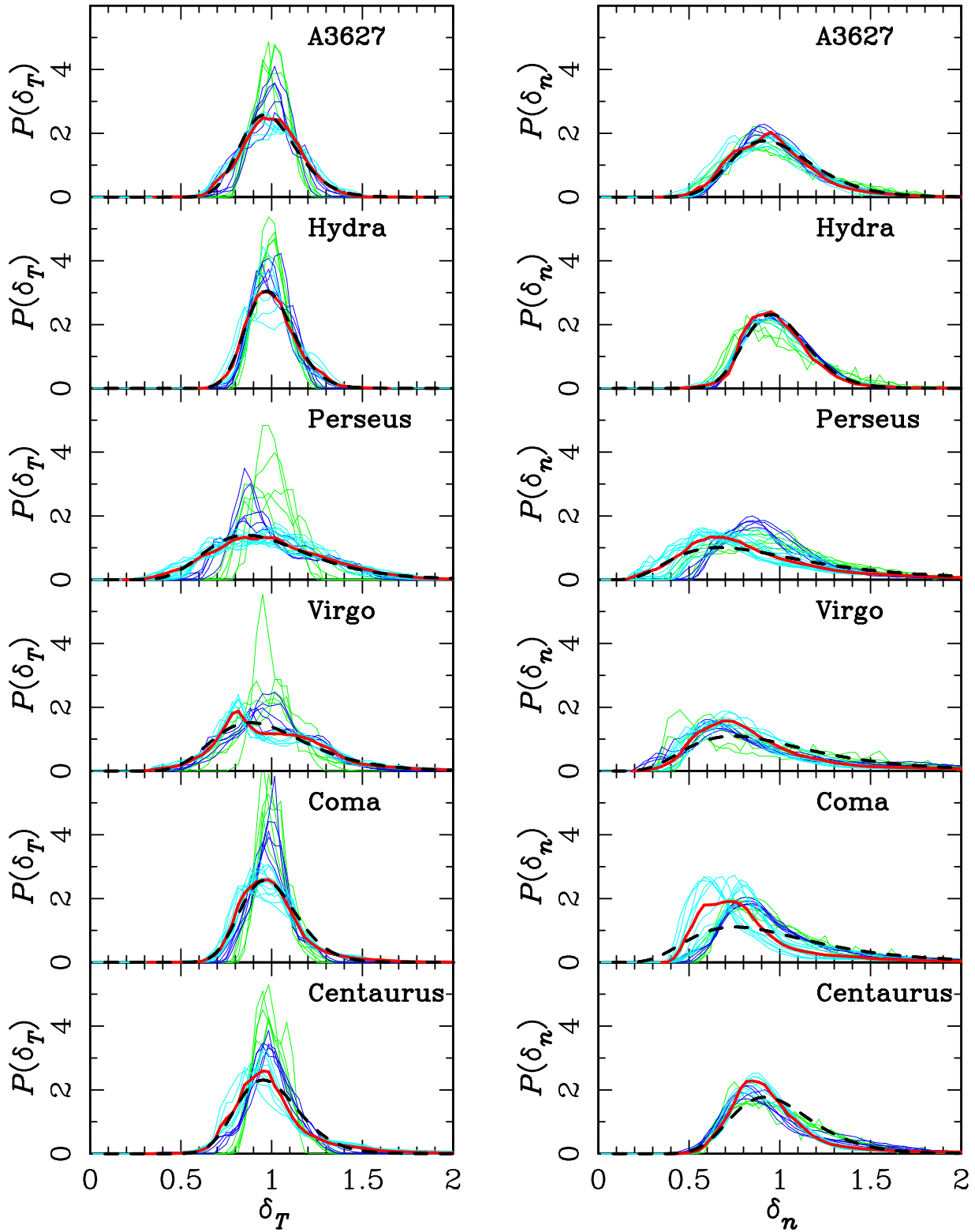


Figure 3.4: The distribution of $\delta_T \equiv T/\bar{T}$ and $\delta_n \equiv n/\bar{n}$. Thick solid lines present the distribution throughout the mesh points of within $r = r_{200}$. Dashed lines are fitting lines of the log-normal distribution. Thin solid lines are the distribution of the shells each $67h^{-1}$ kpc distance from the center. Each color indicates different radial interval: $r < 335h^{-1}$ kpc (green), $335h^{-1}$ kpc $< r < 670h^{-1}$ kpc (blue), and $r > 675h^{-1}$ kpc (cyan).

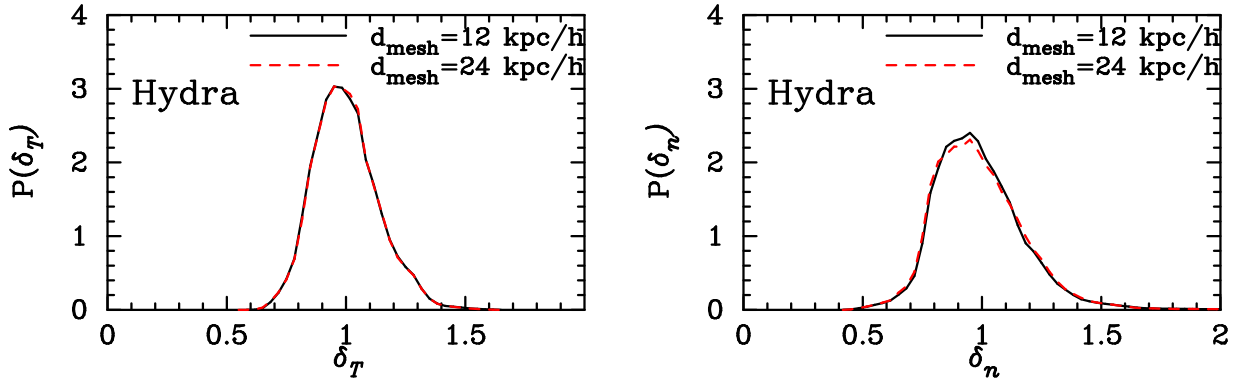


Figure 3.5: The distribution of δ_T (left panel) and δ_n (right panel) within r_{200} for two selections of the mesh size d_{mesh} . Solid and dashed lines indicates $d_{\text{mesh}} = 12 h^{-1} \text{ kpc}$ and $d_{\text{mesh}} = 24 h^{-1} \text{ kpc}$, respectively. We pick up “Hydra” cluster.

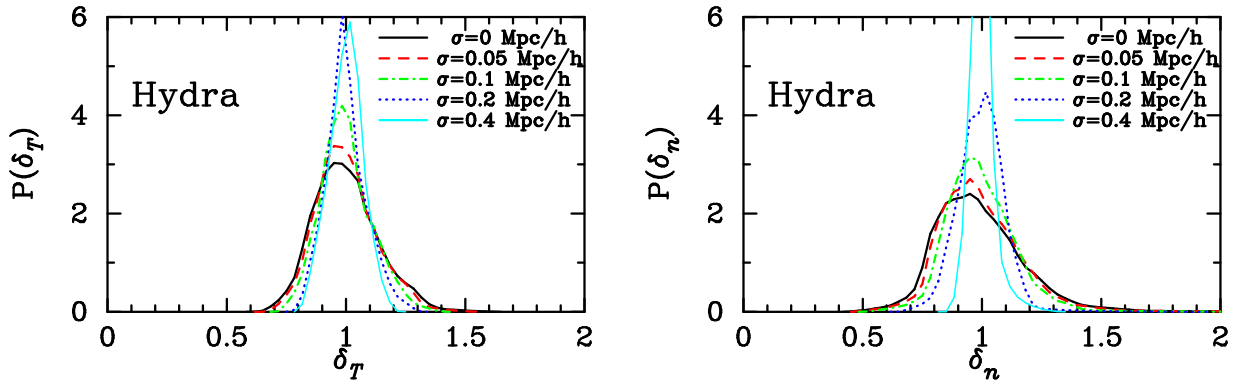


Figure 3.6: The scale dependence of δ_T (left panel) and δ_n (right panel). Each color indicates different smoothing scale: Black, red, green, blue, and cyan correspond to $\sigma = 0$ (without smoothing), 0.05, 0.1, 0.2, and 0.4 Mpc/h, respectively. We pick up “Hydra” cluster.

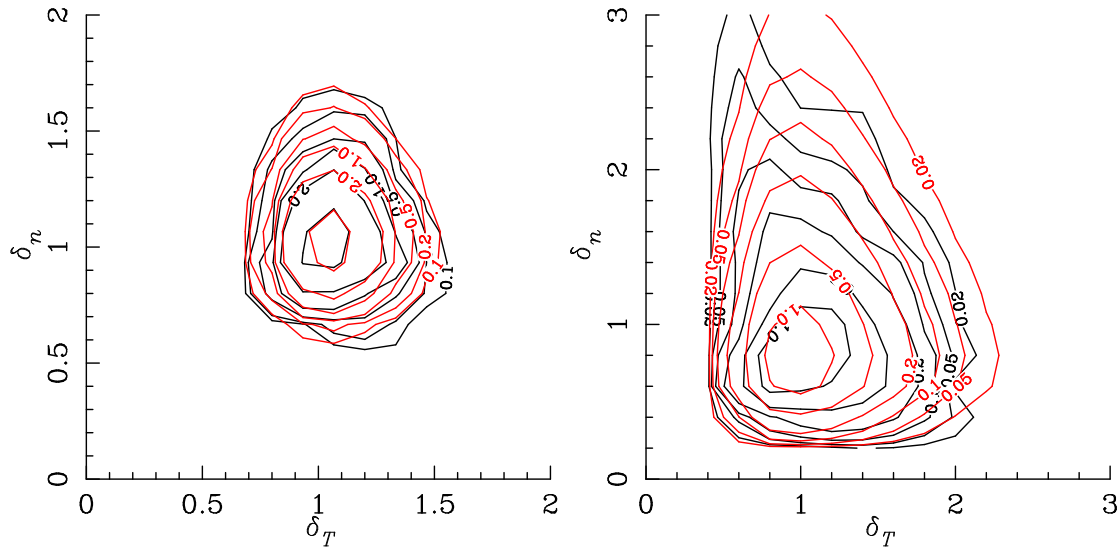


Figure 3.7: The contour map of the joint probability $P(\delta_T, \delta_n)$ within r_{200} (black contour). Red contour indicates the theoretical line of $P(\delta_T)P(\delta_n)$. Left panel shows the case of “Hydra”, Right panel ”Perseus”.

simulations. We cannot obtain enough number of the mesh points in each radial shell. Therefore, we obtain only the distribution throughout the mesh points of within $r = r_{200}$. Figure 3.8 indicates the distribution of $\delta_T \equiv T/\bar{T}$ and $\delta_n \equiv n/\bar{n}$ for two clusters in the grid-based simulation. Despite the noisy behavior due to poor statistics, they approximately follow the lognormal distribution. Thus, the log-normal nature of the fluctuations is physical, rather than numerical.

The triaxial clusters (without fluctuation) also have the distribution around the azimuthally-averaged radial profile. One might consider possibility that the lognormal feature can be explained by the triaxial profile alone. In Appendix B, we calculate the distribution of the triaxial model around the azimuthally-averaged density and temperature. The density and temperature distributions for the different sets of axis ratio are presented in Figure B.2 and Figure B.3, respectively. The resulting distributions have the different shape from the lognormal function. The lognormal feature we found cannot be explained by the triaxial model alone.

3.4 Power Spectra of Density and Temperature Fluctuations

We also investigate the power spectra of the density and temperature inhomogeneities. The power spectra of the fluctuations are crucial for the fluctuation of the projected value, such as the X-ray surface brightness (chapter 6). We extract 100^3 cells of δ_n and δ_T around the center of the simulated cluster and obtain the power spectra. The distance from the center to the corner of the 100^3 cells is ~ 1.0 Mpc/h which is approximately equal to the virial radius of the simulated clusters ($r_{\text{vir}} = 1.0\text{-}1.6$ Mpc/h).

Figure 3.9 shows the power spectra for each simulated cluster for both δ_n (upper panel) and δ_T (lower panel). In each panel a simple power law, $\mathcal{P}(k) \propto k^{-3}$ (dotted line), is also plotted

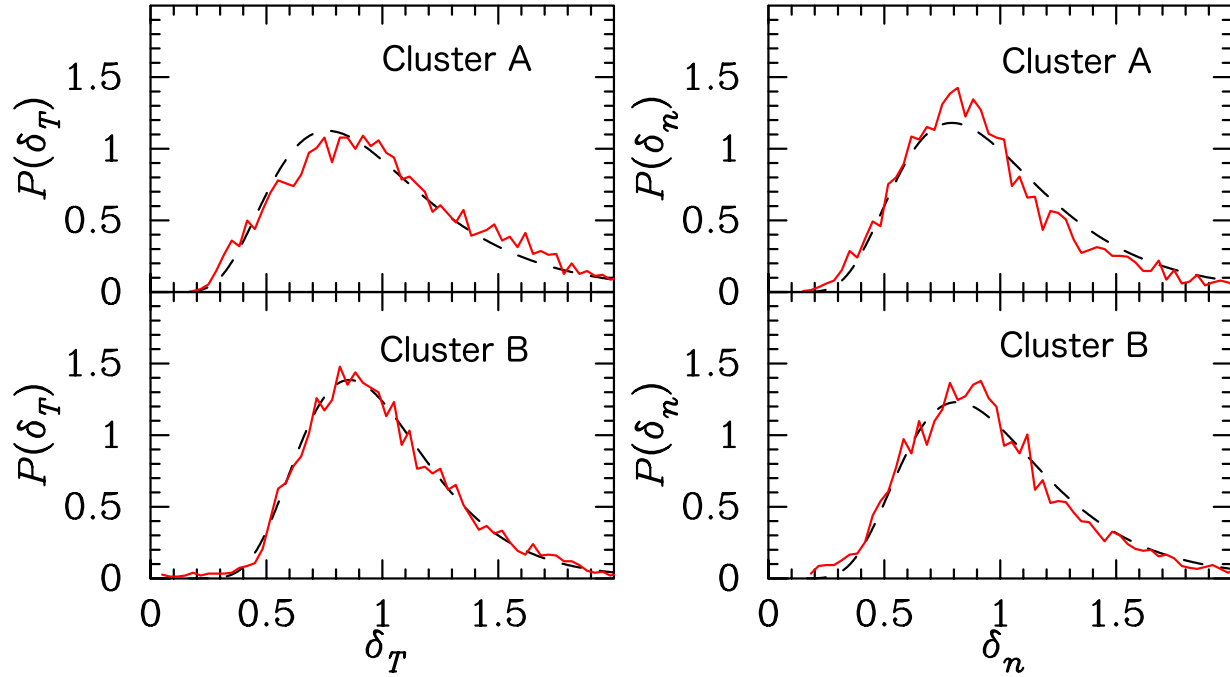


Figure 3.8: The distribution of $\delta_T \equiv T/\bar{T}$ and $\delta_n \equiv n/\bar{n}$ for two clusters in the grid-based simulations. Solid lines (red) present the distribution throughout the mesh points of within $r = r_{200}$. Dashed lines (black) are fitting lines of the log-normal distribution.

for comparison. The power spectra for both the density and temperature are relatively well approximated by a single power law.

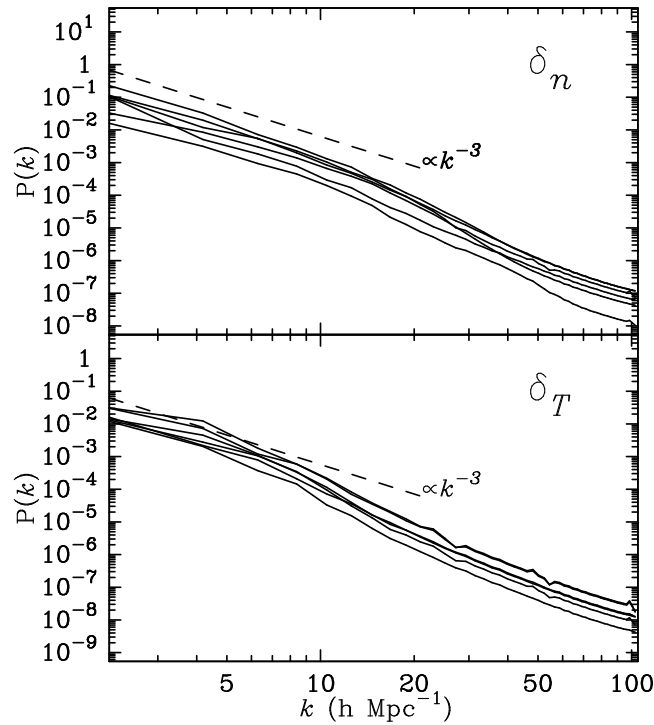


Figure 3.9: The power spectra of δ_n (upper) and δ_T (lower) of the six simulated clusters. Dashed lines indicate $\mathcal{P}(k) \propto k^{-3}$.

3.5 Summary

In this chapter, we have explored the nature of the inhomogeneity of the ICM using the cosmological hydrodynamic simulations. We have found that the local inhomogeneities of the gas temperature and density, after corrected for the global radial profiles, have nearly a universal distribution that resembles the lognormal function. Because both clusters in the SPH and the grid-based simulation show the lognormal feature, we conclude that the lognormal nature is physical, rather than numerical.

Chapter 4

Temperature of Galaxy Clusters

4.1 Different Definitions of Cluster Temperature

The temperature of the ICM is one of the most important of the quantities that characterize a cluster. It is closely related to the total mass of clusters of galaxies. Conventionally, many cosmological applications assume that the ICM is isothermal, and use one representative temperature, T_{cl} . However, T_{cl} is not well-defined when ICM has the internal structure. This becomes a serious problem in interpreting observations, properly. In X-ray observations, the spectroscopic temperature, T_{spec} , is estimated by fitting the thermal continuum and the emission lines of the spectrum (§2.3.3). In the presence of inhomogeneities in the ICM, the temperature so measured is inevitably an *averaged* quantity over a finite sky area and the line-of-sight.

In general, the cluster temperature, T_{cl} , can be written as

$$T_{\text{cl}} \equiv \frac{\int WTdV}{\int WdV}. \quad (4.1)$$

The choice of the weight function, W , leads to several different definitions for specific temperatures. By choosing W to gas density n , equation (4.1) becomes the mass-weighted temperature,

$$T_{\text{mw}} \equiv \frac{\int nTdV}{\int ndV}. \quad (4.2)$$

This definition is directly related to the total thermal energy of the gas ($E \propto M_{\text{gas}}T_{\text{mw}}$) and the cluster mass (e.g., Mathiesen & Evrard, 2001; Nagai et al., 2007). Though challenging, it will be observable either by high-resolution X-ray spectroscopic observations of nearby clusters (Vikhlinin et al., 2006; Nagai et al., 2007) or by a combination of the lower resolution X-ray spectroscopy and the Sunyaev-Zel'dovich imaging observations (Komatsu et al., 1999, 2001; Kitayama et al., 2004).

In order to reproduce T_{spec} (§2.3.3) from equation (4.1), it is natural that one chooses the weight function as the X-ray emissivity $W = \Lambda_X(T)n^2$. It has been conventionally assumed that T_{spec} is approximately equal to the emission-weighted temperature,

$$T_{\text{ew}} \equiv \frac{\int n^2\Lambda_X(T)TdV}{\int n^2\Lambda_X(T)dV}, \quad (4.3)$$

where n is the gas number density, T is the gas temperature, and Λ_X is the cooling function. Mazzotta et al. (2004), however, have pointed out that T_{spec} is systematically lower than T_{ew} . The authors have proposed an alternative definition for the average, *spectroscopic-like temperature*, as

$$T_{\text{sl}} \equiv \frac{\int n^2 T^{a-1/2} dV}{\int n^2 T^{a-3/2} dV}. \quad (4.4)$$

They find that T_{sl} with $a = 0.75$ reproduces T_{spec} within a few percent for simulated clusters hotter than a few keV, assuming Chandra or XMM-Newton detector response functions. Rasia et al. (2005) performed a more systematic study of the relation between T_{ew} and T_{sl} using a sample of clusters from SPH simulations and concluded that $T_{\text{sl}} \sim 0.7 T_{\text{ew}}$. Kay et al. (2007a) also confirmed the relation though the value $T_{\text{sl}}/T_{\text{ew}} \sim 0.8$ is slightly larger than one obtained by Rasia et al. (2005). Vikhlinin (2006) generalize T_{sl} down to ICM temperatures of ~ 0.5 keV and to generic values of the metal abundance. It should be noted that T_{ew} is not directly observable, although it is easily obtained from simulations. We emphasize again that the understanding of above bias is important to confront observational data with theory. As noted by Rasia et al. (2005), it could result in an offset in the mass-temperature relation for clusters of galaxies. Shimizu et al. (2006) studied its impact on the estimation of σ_8 . The authors perform the statistical analysis using the latest X-ray cluster sample and find that $\sigma_8 \sim 0.76 \pm 0.01 + 0.50(1 - \alpha_M)$, where $\alpha_M = T_{\text{spec}}/T_{\text{ew}}$. The systematic difference of $T_{\text{spec}} \sim 0.7 T_{\text{ew}}$ can thus shift σ_8 by ~ 0.15 . Furthermore, its bias should be taken into consideration for study of systematics of the Hubble constant measurement using the SZE and X-rays analysis. In chapter 5, we investigate the origin of this systematics based on an observable quantity, T_{spec} . We summarize the various definitions of cluster temperature above described in Table 4.1.

Table 4.1: Different definitions of cluster temperature T_{cl} .

	symbol	definition
mass-weighted temperature	T_{mw}	$W = n$ (Eq. [4.2])
emission-weighted temperature	T_{ew}	$W = n^2 \Lambda_X(T)$ (Eq. [4.3])
spectroscopic-like temperature	T_{sl}	$W = n^2 T^{a-3/2}$ (Eq. [4.4])
spectroscopic temperature	T_{spec}	by fitting spectra to the plasma model (§2.3.3)

In this chapter, we apply the lognormal model of the ICM inhomogeneity to the spectroscopic temperature of galaxy clusters. The aim of this chapter is to examine the recently reported systematic bias of the temperature estimate using the lognormal model and the global radial profiles.

4.2 Mock Observation of the Simulated Clusters

The discrepancy between T_{ew} and T_{sl} for simulated clusters have been systematically investigated by Rasia et al. (2005). However, they did not directly confirm the discrepancy between T_{ew} and

T_{spec} . Therefore, we start from directly comparing T_{sl} and T_{ew} with T_{spec} using the cosmological hydrodynamical simulation. The simulated clusters used in this section are the same ones described in §3. We compute the photon flux $f(E)$ from the mesh points within radius r_{200} from the cluster center as

$$f(E) dE \propto \exp(-\sigma_{\text{gal}}(E)N_H) \times \sum_{I \in r_{200}} \frac{\rho_I^2}{4\pi(1+z_{\text{cl}})^4} \left(\frac{x_H}{m_p^2}\right) p_\epsilon(T_I, Z, E(1+z_{\text{cl}})) dE(1+z_{\text{cl}}),$$

where z_{cl} denotes the redshift of the simulated cluster, x_H is the hydrogen mass fraction, m_p is the proton mass and $p_\epsilon(T_I, Z, E)$ [erg s⁻¹ cm³ keV⁻¹] is the normalized emission coefficient assuming CIE. Given the fact that the major question that we addressed is not the accurate estimate of T_{spec} or T_{sl} , but the systematic difference between the two, we decided to avoid the unnecessary complication and simply to assume the constant metallicity. Therefore we adopt a constant metallicity of $Z = 0.3 Z_\odot$ in constructing mock spectra above. We calculate $p_\epsilon(T_I, Z, E)$ using SPEX 2.0 (Kaastra et al., 1996). The term $\exp(-\sigma_{\text{gal}}N_H)$ represents the galactic extinction (see §2.3.3); N_H is the column density of hydrogen and $\sigma_{\text{gal}}(E)$ is the absorption cross section of Morrison & McCammon (1983). Since we are interested in the effect due to the spectrum distortion, not statistical error, we adopt a long exposure time as the total photon counts $\mathcal{N} = \int_{E=0.5 \text{ keV}}^{E=10 \text{ keV}} Ef(E) dE \sim 500,000$. In this thesis, we consider mock observations using *Chandra* and *XMM-Newton*, thus we neglect a peculiar velocity of the cluster and a turbulent velocity in ICM because of insufficient energy resolution of *Chandra* ACIS-S3 and *XMM-Newton* MOS1 detector.

The mock observed spectra are created by XSPEC version 12.0 (Arnaud, 1996). We consider three cases for the detector response corresponding to 1) perfect response, 2) *Chandra* ACIS-S3, and 3) *XMM-Newton* MOS1. In the first case, we also assume no galactic extinction ($N_H = 0$) and refer to it as an “IDEAL” case. In the second and third cases, we adopt an observed value to N_H listed in Table 3.1 and redistribute the photon counts of the detector channel according to RMF (redistribution matrix file) of ACIS-S3 and MOS1 using the *rejection method*.

Figure 4.1 illustrates the mock spectra of “Virgo” and “Perseus” using RMF of ACIS-S3. Unless stated otherwise, we fit the spectra by an absorbed single-temperature MEKAL model in the energy band 0.5-10.0 keV. We define the spectroscopic temperature, T_{spec} , as the best-fit temperature provided by this procedure. Since the spatial resolution of the current simulations is not sufficient to fully resolve the cooling central regions, a single-temperature model yields a reasonable fit to the mock spectra. For comparison, we also plot the spectra for a single temperature corresponding to the “emission weighted” value of the mesh points within r_{200} :

$$T_{\text{ew}}^{\text{sim,m}} = \frac{\sum_{I \in r_{200}} \rho_I^2 T_I \Lambda_X(T_I)}{\sum_{I \in r_{200}} \rho_I^2 \Lambda_X(T_I)}. \quad (4.5)$$

We calculate the cooling function $\Lambda_X(T)$ using SPEX 2.0 assuming CIE, the energy range of 0.5-10.0 keV, and the metallicity $0.3Z_\odot$. The difference between T_{spec} and $T_{\text{ew}}^{\text{sim,m}}$ is clearly distinguishable on the spectral basis in the current detectors. We provide T_{spec} and $T_{\text{ew}}^{\text{sim,m}}$ for the six simulated clusters in Table 4.2.

Figure 4.2 shows the relation between T_{spec} and T_{ew} for our sample of simulated clusters. It is well represented by a linear relation $T_{\text{spec}} = kT_{\text{ew}} + l$ with the fitted values of $k = 0.84, l = 0.34$

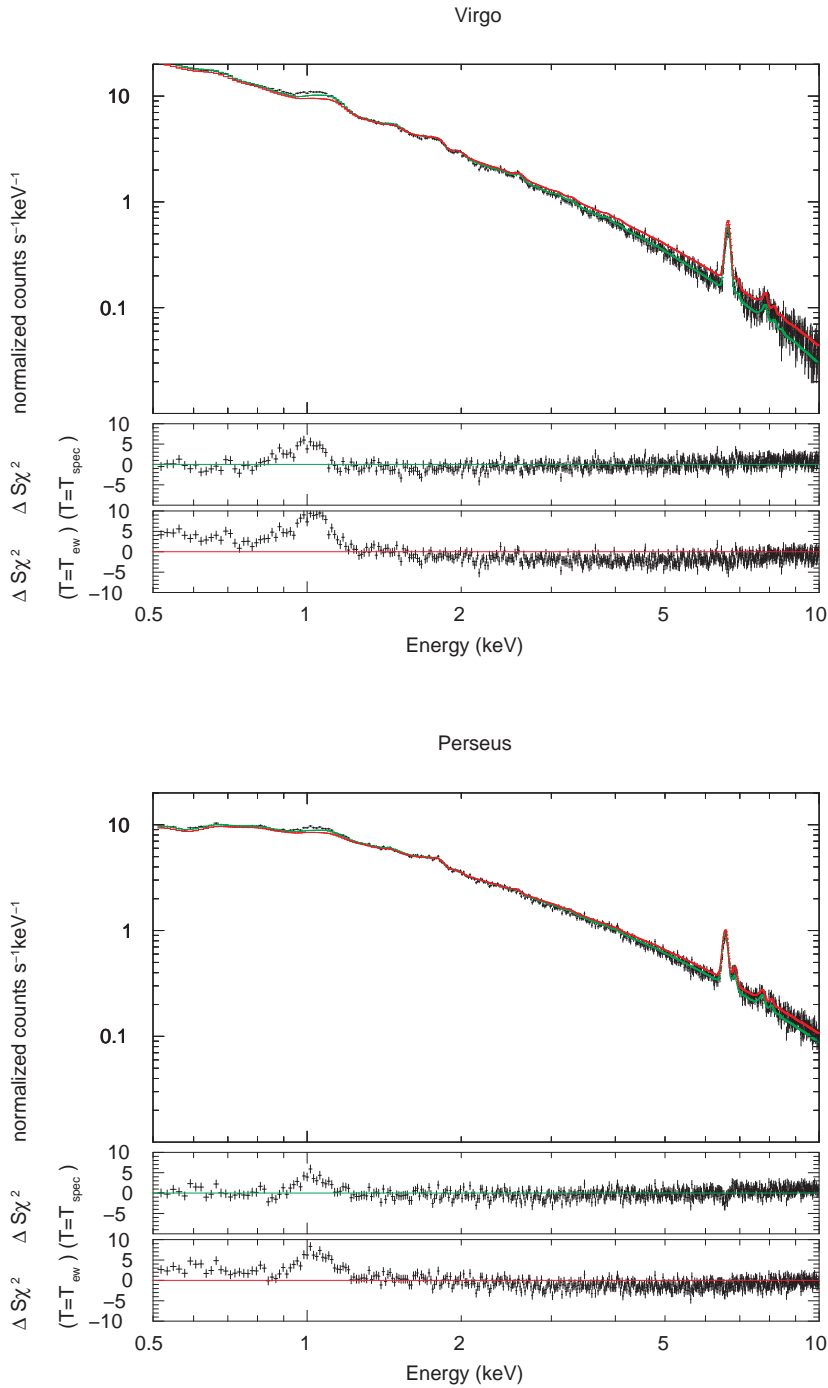


Figure 4.1: The examples of the mock spectrum of two simulated clusters. The top panel shows the results for “Virgo” and the bottom panel for “Perseus.” Black marks are the mock spectra. Green line provides the best-fit spectrum, Red line is that of a single temperature thermal model with the temperature $T = T_{\text{ew}}^{\text{sim,m}}$. Each panel has two residuals in terms of sigmas with error bar of size one. Upper one is the residual of the best-fit spectrum ($T = T_{\text{spec}}$). Lower one is that of the thermal model with the emission weighted temperature ($T = T_{\text{ew}}^{\text{sim,m}}$).

Table 4.2: Temperature of the six simulated clusters and observed clusters.

	Simulation					
	A3627	Hydra	Perseus	Virgo	Coma	Centaurus
T_{spec} (IDEAL) [keV] (0.5-10.0 keV)	4.1	3.9	5.0	3.3	6.1	3.9
T_{spec} (ACIS) [keV] (0.5-10.0 keV)	4.1	3.9	5.0	3.3	6.0	4.0
T_{spec} (MOS) [keV] (0.5-10.0 keV)	4.0	3.8	5.0	3.3	6.0	4.0
T_{spec} (IDEAL) [keV] (0.1-2.4 keV)	4.0	3.7	4.7	3.1	5.9	3.9
T_{spec} (IDEAL) [keV] (2.0-10.0 keV)	4.1	4.0	5.4	3.6	6.5	4.0
$T_{\text{ew}}^{\text{sim,m}}$ [keV]	4.2	4.1	5.7	3.7	6.7	4.2
$T_{\text{sl}}^{\text{sim,m}}$ [keV]	4.0	3.8	4.7	3.2	5.9	3.9
κ_{sim} (mesh-wise)	0.95	0.92	0.84	0.86	0.88	0.95
κ_{sim} (particle-wise)	0.88	0.89	0.70	0.75	0.84	0.86
κ^{RP}	0.97	0.94	0.98	0.94	0.96	0.97

(IDEAL), $k = 0.84, l = 0.36$ (ACIS) and $k = 0.85, l = 0.31$ (MOS), respectively. In the range of temperatures corresponding to rich clusters, the spectroscopic temperature T_{spec} is systematically lower than T_{ew} by 10 – 20 %.

We note that the above bias should depend on the energy band in which T_{spec} is evaluated. In order to demonstrate it quantitatively, we also list in Table 4.2 the fitted values of T_{spec} from the 0.1-2.4 keV and 2.0-10.0 keV data, respectively. Because the exponential tail of the thermal bremsstrahlung spectrum from hotter components has negligible contribution in the softer band, the bias tends to increase and decrease in the softer and harder bands, respectively.

4.2.1 Spectroscopic-Like Temperature

In order to better approximate T_{spec} , Mazzotta et al. (2004) proposed a “spectroscopic-like temperature”; they found that equation (4.4) with $a = 0.75$ reproduces T_{spec} in the 0.5-10.0 keV band within a few percent. Throughout this thesis, we adopt $a = 0.75$ when we estimate the spectroscopic-like temperature quantitatively. In Figure 4.2, we also plot this quantity computed from the mesh points within r_{200} :

$$T_{\text{sl}}^{\text{sim,m}} = \frac{\sum_{I \in r_{200}} \rho_I^2 T_I^{0.25}}{\sum_{I \in r_{200}} \rho_I^2 T_I^{-0.75}}. \quad (4.6)$$

As indicated in the bottom panel, $T_{\text{sl}}^{\text{sim,m}}$ reproduces T_{spec} within 6 % for all the simulated clusters in our sample. Given this agreement, we hereafter use $T_{\text{sl}}^{\text{sim,m}}$ to represent T_{spec} , and express the bias in the spectroscopic temperature by

$$\kappa_{\text{sim}} \equiv T_{\text{sl}}^{\text{sim,m}} / T_{\text{ew}}^{\text{sim,m}}. \quad (4.7)$$

Table 4.2 provides κ_{sim} (mesh-wise) for the six simulated clusters. The range of κ_{sim} (mesh-wise) is approximately 0.8-0.9. While κ_{sim} is systematically lower than unity, the value is somewhat higher than the results of Rasia et al. (2005), $T_{\text{sl}} \sim 0.7T_{\text{ew}}$. This is likely due to the different

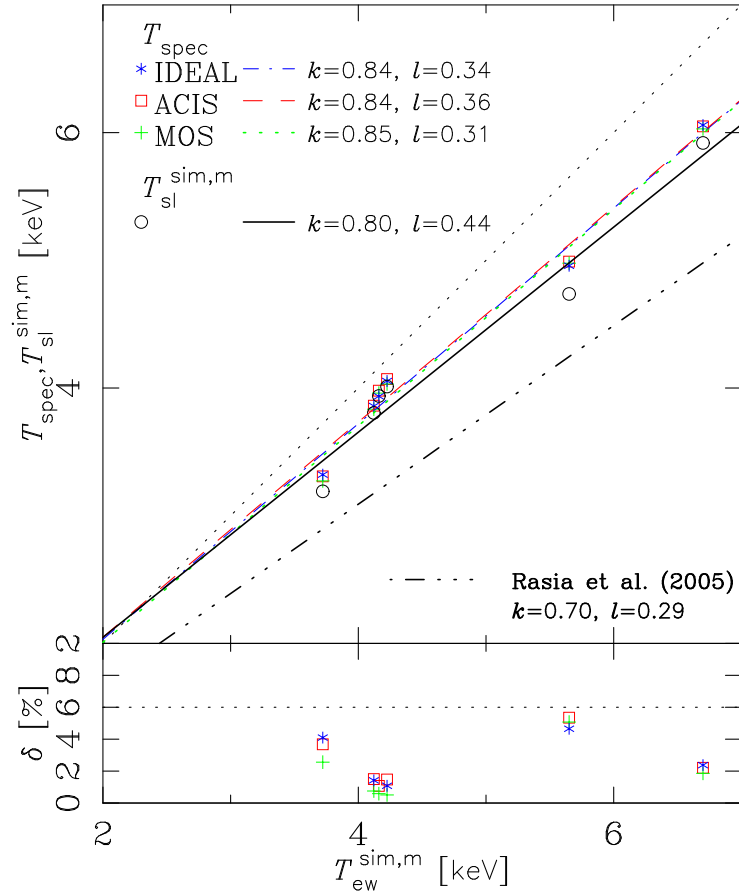


Figure 4.2: The upper panel shows the relation of $T_{\text{ew}}^{\text{sim,m}}$ to T_{spec} (asterisk shows IDEAL, square ACIS, and plus MOS) and $T_{\text{sl}}^{\text{sim,m}}$ (open circle). The lower panel shows the difference between T_{spec} and $T_{\text{sl}}^{\text{sim,m}}$: $\delta \equiv 100(T_{\text{spec}}/T_{\text{sl}}^{\text{sim,m}} - 1)[\%]$, where T_{spec} is the best-fit temperature of the mock spectra and $T_{\text{sl}}^{\text{sim,m}}$ is given by equation (4.6).

physics incorporated in the simulations and the difference in how T_{sl} and T_{ew} are computed from the simulation outputs. The major difference of the physics is the amplitude of the wind velocity employed; Rasia et al. (2005) used have a feedback with weaker wind of 340km s^{-1} , while our current simulations adopt a higher value of 480km s^{-1} . Because weaker wind cannot remove small cold blobs effectively, the value of $T_{\text{sl}}/T_{\text{ew}}$ of Rasia et al. (2005) is expected to be larger.

To show the difference of the temperature computation scheme explicitly, we also list in Table 4.2 the values of $\kappa_{\text{sim}} \equiv T_{\text{sl}}^{\text{sim,p}}/T_{\text{ew}}^{\text{sim,p}}$ (particle-wise) computed in the ‘‘particle-wise’’ definitions used in Rasia et al. (2005):

$$T_{\text{ew}}^{\text{sim,p}} = \frac{\sum_{i \in r_{200}} m_i \rho_i \Lambda_X(T_i) T_i}{\sum_{i \in r_{200}} m_i \rho_i \Lambda_X(T_i)}, \quad (4.8)$$

and

$$T_{\text{sl}}^{\text{sim,p}} = \frac{\sum_{i \in r_{200}} m_i \rho_i T_i^{0.25}}{\sum_{i \in r_{200}} m_i \rho_i T_i^{-0.75}}, \quad (4.9)$$

(see also Borgani et al., 2004). In practice, the emission-weighted and spectroscopic-like temperatures defined in equation (4.8) and equation (4.9) are sensitive to a small number of cold (and dense) SPH particles present, while their contribution is negligible in the mesh-wise definitions, equation (4.5) and equation (4.6). As in Rasia et al. (2005), we have removed the SPH particles below a threshold temperature $T_{\text{lim}} = 0.5$ keV to compute κ_{sim} (particle-wise). Table 4.2 indicates that κ_{sim} (particle-wise) tends to be systematically smaller than κ_{sim} (mesh-wise). Even adopting $T_{\text{lim}} = 0.01$ keV makes κ_{sim} (particle-wise) smaller only by a few percent.

Given the limit of the particle-wise definitions mentioned above, we use the mesh-wise definitions of the emission-weighted temperature ($T_{\text{ew}}^{\text{sim,m}}$) and the spectroscopic-like temperature ($T_{\text{sl}}^{\text{sim,m}}$) given in equation (4.5) and (4.6), respectively, in the following sections.

4.3 Analytical Model

Based on the distributions of gas density and temperature described in chapter 3, we develop an analytical model to describe the contributions of the *radial profile* (RP) and the *local inhomogeneities* (LI) to the bias in the spectroscopic temperature.

To describe the emission-weighted and spectroscopic-like temperatures in simple forms, let us define a quantity:

$$\begin{aligned} A_\alpha &\equiv \int n(\mathbf{r})^2 T(\mathbf{r})^\alpha d\mathbf{r}, \\ &= \int_0^R r^2 dr \int d\Omega n^2(\mathbf{r}) T^\alpha(\mathbf{r}), \end{aligned} \quad (4.10)$$

where the second line is for the spherical coordinate and R denotes the maximum radius considered here (we adopt $R = r_{200}$). Using this quantity, we can write down T_{sl} via equation (4.4) as

$$T_{\text{sl}}^{\text{model}} = A_{a-1/2}/A_{a-3/2}. \quad (4.11)$$

When the temperature is higher than ~ 3 keV, the cooling function is dominated by the thermal bremsstrahlung; $\Lambda_X \approx \Lambda_{\text{brems}} \propto \sqrt{T}$ (§2.3.2; Eq. [2.44]). We find that substitution \sqrt{T} for $\Lambda_X(T)$ yields only $\sim 1\%$ difference for the simulated clusters. In the present model, we adopt for simplicity the thermal bremsstrahlung cooling function, $\Lambda_X \propto \sqrt{T}$, and then equation (4.3) reduces to

$$T_{\text{ew}}^{\text{model}} = A_{3/2}/A_{1/2}. \quad (4.12)$$

When evaluating equation (4.10), we replace the spatial average with the ensemble average:

$$\int d\Omega n^2(\mathbf{r})T^\alpha(\mathbf{r}) = 4\pi[\bar{n}(r)]^2[\bar{T}(r)]^\alpha \int \int \delta_n^2 \delta_T^\alpha P(\delta_n, \delta_T; r) d\delta_n d\delta_T, \quad (4.13)$$

where $P(\delta_n, \delta_T; r)$ is a joint probability density function at r , $\bar{n}(r)$ and $\bar{T}(r)$ are the average profile defined by

$$\bar{n}(r) \equiv \frac{1}{4\pi} \int d\Omega n(\mathbf{r})|_{|\mathbf{r}|=r} \quad (4.14)$$

$$\bar{T}(r) \equiv \frac{1}{4\pi} \int d\Omega T(\mathbf{r})|_{|\mathbf{r}|=r}, \quad (4.15)$$

where Ω indicates the solid angle. Assuming further that the temperature inhomogeneity is uncorrelated with that of density, i.e. $P(\delta_n, \delta_T; r) = P(\delta_n; r)P(\delta_T; r)$, we obtain

$$A_\alpha = 4\pi \int_0^R r^2 [\bar{n}(r)]^2 [\bar{T}(r)]^\alpha dr \int_0^\infty \delta_n^2 P(\delta_n; r) d\delta_n \int_0^\infty \delta_T^\alpha P(\delta_T; r) d\delta_T. \quad (4.16)$$

The average quantities for the lognormal distribution are given in Appendix A (Eq. [A.10]). Then, we obtain

$$\int_0^\infty \delta_T^\alpha P(\delta_T; r) d\delta_T = \exp\left[\frac{\alpha(\alpha-1)\sigma_{\text{LN},T}(r)^2}{2}\right], \quad (4.17)$$

$$\int_0^\infty \delta_n^2 P(\delta_n; r) d\delta_n = \exp[\sigma_{\text{LN},n}(r)^2]. \quad (4.18)$$

If $\sigma_{\text{LN},T}$ and $\sigma_{\text{LN},n}$ are independent of the radius ($\sigma_{\text{LN},T}(r) = \sigma_{\text{LN},T}$, $\sigma_{\text{LN},n}(r) = \sigma_{\text{LN},n}$), equation (4.16) reduces to

$$A_\alpha = \exp(\sigma_{\text{LN},n}^2) \exp\left[\frac{\alpha(\alpha-1)}{2} \sigma_{\text{LN},T}^2\right] \times 4\pi \int_0^R r^2 [\bar{n}(r)]^2 [\bar{T}(r)]^\alpha dr. \quad (4.19)$$

Using the above results, $T_{\text{sl}}^{\text{model}}$ and $T_{\text{ew}}^{\text{model}}$ are expressed as

$$T_{\text{sl}}^{\text{model}} = A_{a-1/2}/A_{a-3/2} = T_{\text{sl}}^{\text{RP}} \exp\left[\left(a - \frac{3}{2}\right) \sigma_{\text{LN},T}^2\right], \quad (4.20)$$

$$T_{\text{ew}}^{\text{model}} = A_{3/2}/A_{1/2} = T_{\text{ew}}^{\text{RP}} \exp\left(\frac{1}{2} \sigma_{\text{LN},T}^2\right), \quad (4.21)$$

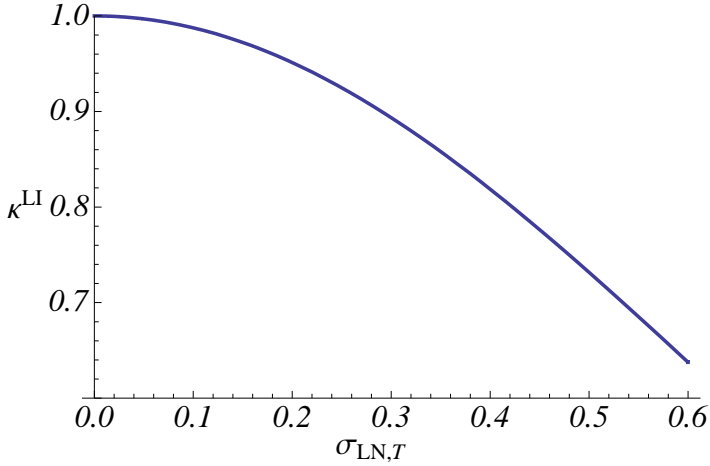


Figure 4.3: The shape of $\kappa^{\text{LI}}(\sigma_{\text{LN},T})$ adopting $a = 0.75$. In the case of $\sigma_{\text{LN},T} = 0.1$ and 0.3 , $\kappa^{\text{LI}} \sim 0.99$ and 0.89 , respectively (See Table 4.2).

where $T_{\text{sl}}^{\text{RP}}$ and $T_{\text{ew}}^{\text{RP}}$ are defined as

$$T_{\text{sl}}^{\text{RP}} \equiv \frac{\int_0^R r^2 [\bar{n}(r)]^2 [\bar{T}(r)]^{(a-1/2)} dr}{\int_0^R r^2 [\bar{n}(r)]^2 [\bar{T}(r)]^{(a-3/2)} dr}, \quad (4.22)$$

$$T_{\text{ew}}^{\text{RP}} \equiv \frac{\int_0^R r^2 [\bar{n}(r)]^2 [\bar{T}(r)]^{3/2} dr}{\int_0^R r^2 [\bar{n}(r)]^2 [\bar{T}(r)]^{1/2} dr}. \quad (4.23)$$

As expected, $T_{\text{sl}}^{\text{model}}$ and $T_{\text{ew}}^{\text{model}}$ reduce to $T_{\text{sl}}^{\text{RP}}$ and $T_{\text{ew}}^{\text{RP}}$ in the absence of local inhomogeneities ($\sigma_{\text{LN},T} = 0$). Note that equations (4.20) and (4.21) are independent of $\sigma_{\text{LN},n}$. This holds true as long as the density distribution $P(\delta_n)$ is independent of r .

The ratio of $T_{\text{sl}}^{\text{model}}$ and $T_{\text{ew}}^{\text{model}}$ is now written as

$$\kappa_{\text{model}} \equiv T_{\text{sl}}^{\text{model}}/T_{\text{ew}}^{\text{model}} = \kappa^{\text{RP}} \kappa^{\text{LI}}, \quad (4.24)$$

where κ^{RP} and κ^{LI} denote the bias due to the radial profile and the local inhomogeneities,

$$\kappa^{\text{RP}} \equiv T_{\text{sl}}^{\text{RP}}/T_{\text{ew}}^{\text{RP}}, \quad (4.25)$$

and

$$\kappa^{\text{LI}} \equiv \exp [(a-2) \sigma_{\text{LN},T}^2], \quad (4.26)$$

respectively.

Figure 4.3 shows κ^{LI} for a fiducial value of $a = 0.75$ as a function of $\sigma_{\text{LN},T}$. The range of $\sigma_{\text{LN},T}$ of simulated clusters, $0.1 < \sigma_{\text{LN},T} < 0.3$, (Table 3.1) corresponds to $0.99 > \kappa^{\text{LI}} > 0.89$.

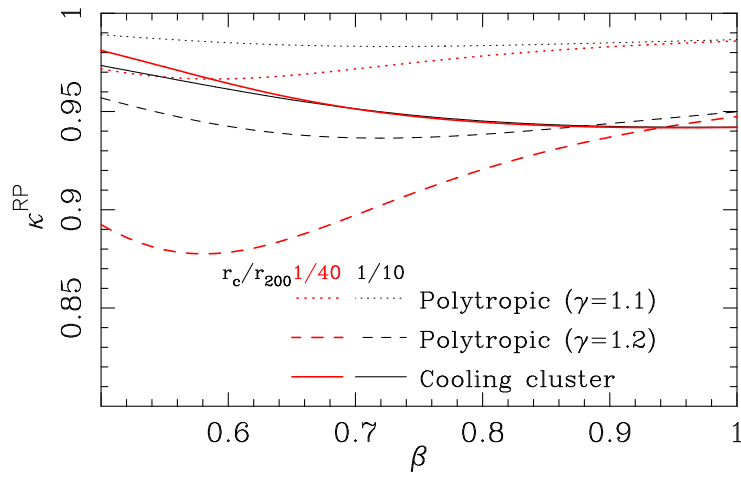


Figure 4.4: The bias due to the radial profile κ^{RP} (Eq.[4.25]) assuming the β model and two temperature models. We assume that the density profile is given by the β model. We consider three temperature models: the polytropic model (dotted line provides $\gamma = 1.1$, dashed line $\gamma = 1.2$) and the cooling cluster model (solid line). We assume the two case of r_c/r_{200} . One is $r_c/r_{200} = 1/10$ (black line). Another is $r_c/r_{200} = 1/40$ (red line).

In the case of the β model density profile (Eq.[2.16]) and the polytropic temperature profile (Eq.[2.24]), $T_{\text{sl}}^{\text{RP}}$ and $T_{\text{ew}}^{\text{RP}}$ are expressed as

$$\kappa^{\text{RP}} = T_{\text{sl}}^{\text{RP}}/T_{\text{ew}}^{\text{RP}}, \quad (4.27)$$

$$T_{\text{sl}}^{\text{RP}} = J(\beta, \gamma, r_c/R; a - 3/2) T_0, \quad (4.28)$$

$$T_{\text{ew}}^{\text{RP}} = J(\beta, \gamma, r_c/R; 1/2) T_0, \quad (4.29)$$

where we define

$$J(\beta, \gamma, q_J; x_J) \equiv \frac{{}_2F_1(3/2, 3\beta[1 + (x_J + 1)(\gamma - 1)/2]; 5/2; -1/q_J^2)}{{}_2F_1(3/2, 3\beta[1 + x_J(\gamma - 1)/2]; 5/2; -1/q_J^2)}, \quad (4.30)$$

where ${}_2F_1(\alpha, \beta; \gamma; \zeta)$ is the hyper geometric function.

Figure 4.4 shows κ^{RP} as a function of β for various choices of γ and r_c/r_{200} . Given that a number of observed clusters exhibit a cool core, we also plot the cooling cluster model (Eq. [2.25]). For the range of parameters considered here, κ^{RP} exceeds 0.9. This implies that the bias in the spectroscopic temperature is not fully accounted for by the global temperature and density gradients alone; local inhomogeneities should also make an important contribution to the bias.

4.4 Comparison with Simulated Clusters

We now examine the extent to which the analytical model described in the previous section explains the bias in the spectroscopic temperature. The departure in the radial density and temperature distributions from the β model and the polytropic model results in up to 7 % errors in the values of $T_{\text{ew}}^{\text{RP}}$ and $T_{\text{sl}}^{\text{RP}}$. Since our model can be applied to arbitrary $\bar{n}(r)$ and $\bar{T}(r)$, we hereafter use for these quantities the radially averaged values calculated directly from the simulation data. We combine them with $\sigma_{\text{LN}, T}$ in Table 3.1 to obtain $T_{\text{sl}}^{\text{model}}$ (Eq.[4.20]) and $T_{\text{ew}}^{\text{model}}$ (Eq.[4.21]).

Figure 4.5 compares $T_{\text{sl}}^{\text{model}}$ and $T_{\text{ew}}^{\text{model}}$ against $T_{\text{sl}}^{\text{sim}, \text{m}}$ and $T_{\text{ew}}^{\text{sim}, \text{m}}$ (Eq.[4.6] and Eq.[4.5]), respectively. For all clusters except ‘‘Perseus’’, the model reproduces within 10 percent accuracy the temperatures averaged over all the mesh points of the simulated clusters.

Given the above agreement, we further plot κ_{model} against κ_{sim} in Figure 4.6. The difference between κ_{sim} and κ_{model} is kept within ~ 10 % in all the cases. Considering the simplicity of our current model, the agreement is remarkable. In all the clusters, both κ^{RP} and κ^{LI} are greater than κ_{sim} , indicating that their combination is in fact responsible for the major part of the bias in the spectroscopic temperature.

In § 4.3, we assumed that n and T are uncorrelated based on the result of §3.3, i.e., $P(\delta_n, \delta_T) = P(\delta_n)P(\delta_T)$. We examine this assumption in more detail. Although the effects of the correlation is hard to model in general, we can show that it does not change the value of $\kappa_{\text{model}} \equiv T_{\text{sl}}^{\text{model}}/T_{\text{ew}}^{\text{model}}$ as long as the joint probability density function follows the bivariate log-normal distribution:

$$P_{\text{BLN}}(\delta_n, \delta_T; \sigma_{\text{LN}, n}; \sigma_{\text{LN}, T}) d\delta_n d\delta_T = \frac{(1 - \rho'^2)^{-1/2}}{2\pi\sigma_{\text{LN}, n}\sigma_{\text{LN}, T}} \exp\left[-\frac{A^2 - 2\rho'AB + B^2}{2(1 - \rho'^2)}\right] \frac{d\delta_n}{\delta_n} \frac{d\delta_T}{\delta_T}, \quad (4.31)$$

where $\rho' \equiv \log[\rho(\exp\sigma_{\text{LN}, n}^2 - 1)^{1/2}(\exp\sigma_{\text{LN}, T}^2 - 1)^{1/2} + 1]/\sigma_{\text{LN}, T}\sigma_{\text{LN}, n}$, $A \equiv \log(\delta_n) + \sigma_{\text{LN}, n}^2/2$, $B \equiv \log(\delta_T) + \sigma_{\text{LN}, T}^2/2$, and ρ is the correlation coefficient between n and T . In Appendix

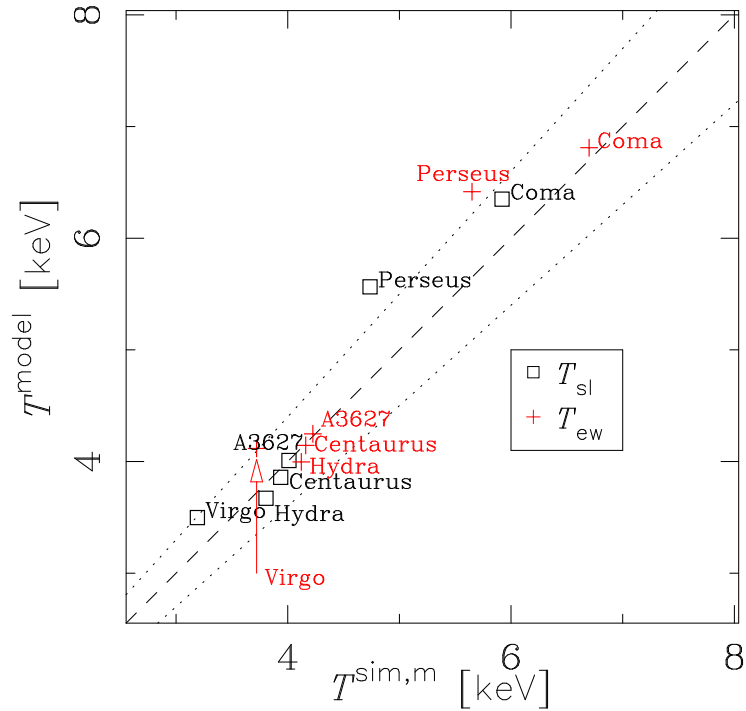


Figure 4.5: The emission weighted and spectroscopic like temperature provided our model and the simulation. Dashed line shows $T_{ew}^{sim,m} = T_{ew}^{model}$ or $T_{sl}^{sim,m} = T_{sl}^{model}$. Dotted lines show $T_{ew}^{sim,m}/T_{ew}^{model} - 1 = \pm 0.1$ or $T_{sl}^{sim,m}/T_{sl}^{model} - 1 = \pm 0.1$. In all clusters except “Perseus”, the temperatures of the model reproduce that of the simulation within 10 percent.

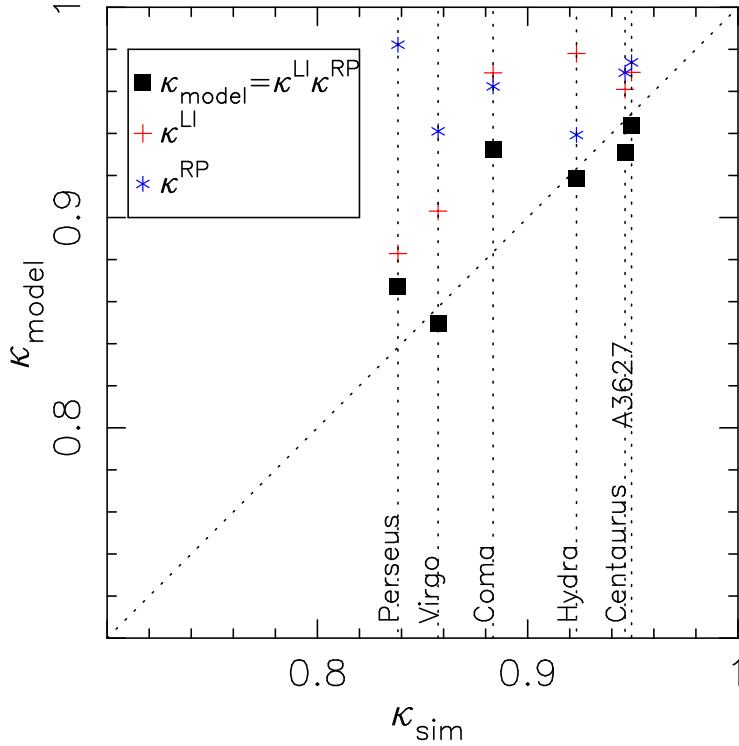


Figure 4.6: The bias factor κ provided our model and the simulation. Squares show κ_{model} . Asterisks and crosses show κ^{RP} and κ^{LI} which are calculated from our model. In all cases, κ_{model} is kept within $\sim 10\%$.

A.2, we summarize the nature of the bivariate lognormal function. Adopting $\rho = 0$ yields $P_{\text{BLN}}(\delta_n, \delta_T; \sigma_{\text{LN}, n}; \sigma_{\text{LN}, T}) = P_{\text{LN}}(\delta_n; \sigma_{\text{LN}, n}) P_{\text{LN}}(\delta_T; \sigma_{\text{LN}, T})$. The marginal probability density function of density and that of temperature are equal to $P_{\text{LN}}(\delta_n; \sigma_{\text{LN}, n})$ and $P_{\text{LN}}(\delta_T; \sigma_{\text{LN}, T})$, respectively. Using $P_{\text{BLN}}(\delta_n, \delta_T; \sigma_{\text{LN}, n}; \sigma_{\text{LN}, T})$, we obtain $T_{\text{sl}}^{\text{model}}$, $T_{\text{ew}}^{\text{model}}$ as

$$T_{\text{sl}}^{\text{model}} = T_{\text{sl}}^{\text{RP}} \exp \left[\left(a - \frac{3}{2} \right) \sigma_{\text{LN}, T}^2 + 2\rho' \sigma_{\text{LN}, T} \sigma_{\text{LN}, n} \right] \quad (4.32)$$

$$T_{\text{ew}}^{\text{model}} = T_{\text{ew}}^{\text{RP}} \exp \left(\frac{1}{2} \sigma_{\text{LN}, T}^2 + 2\rho' \sigma_{\text{LN}, T} \sigma_{\text{LN}, n} \right). \quad (4.33)$$

Although both $T_{\text{sl}}^{\text{model}}$ and $T_{\text{ew}}^{\text{model}}$ increase with the correlation coefficient, $\kappa_{\text{model}} \equiv T_{\text{sl}}^{\text{model}} / T_{\text{ew}}^{\text{model}}$ remains the same as that given by equation (4.26).

4.5 Mass-weighted Temperature

In this chapter, we have focused on the difference between T_{spec} (T_{sl}) and T_{ew} , which is most relevant to X-ray spectral analysis. Furthermore we discuss the mass-weighted temperature, T_{mw} (Eq. [4.2]) in this section. On the assumption that δ_T and δ_n are independent, T_{mw} is

not dependent on the local inhomogeneity, but on the radial density and temperature profiles. Therefore, we can write T_{mw} as

$$T_{\text{mw}}^{\text{model}} \equiv \frac{\int_0^R r^2 \bar{n}(r) \bar{T}(r) dr}{\int_0^R r^2 \bar{n}(r) dr}. \quad (4.34)$$

The triangle symbols in Figure 4.7 indicate $T_{\text{mw}}^{\text{model}}$ and the simulated mass-weighted temperature described as

$$T_{\text{mw}}^{\text{sim,m}} = \frac{\sum_{I \in r_{200}} \rho_I T_I}{\sum_{I \in r_{200}} \rho_I}. \quad (4.35)$$

As shown in Figure 4.7, T_{mw} is well reproduced by equation (4.34). Because the simulated clusters have a trend that temperature increases in the inner radius (Fig. 3.3), T_{ew} and T_{sl} , which are proportional to density squared, are larger than T_{mw} .

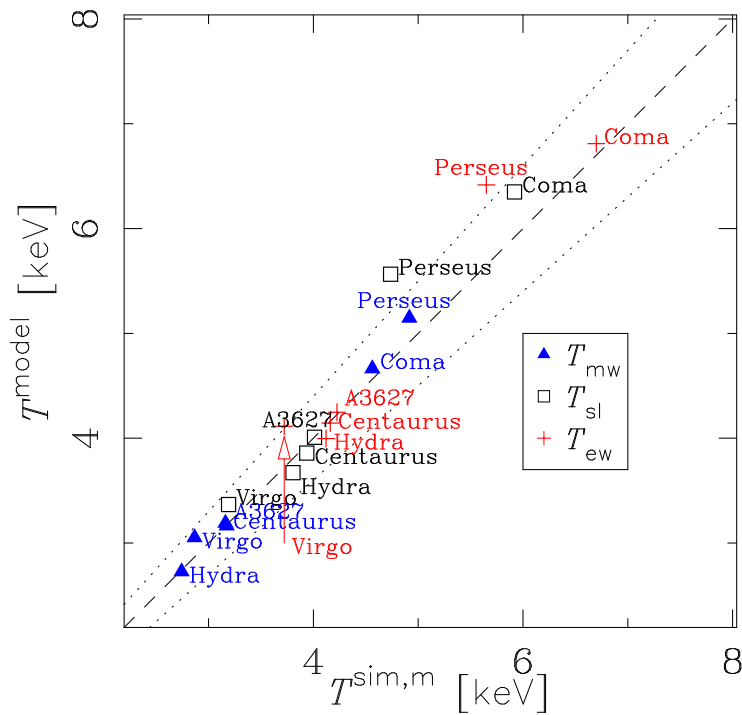


Figure 4.7: The mass-weighted temperature provided our model and the simulation (filled triangles). The spectroscopic-like temperature (square) and the emission-weighted temperature (plus) are also shown. The dashed and dotted lines are the same as Figure 4.5.

In the case of the β model density profile (Eq.[2.16]) and the polytropic temperature profile (Eq.[2.24]), T_{mw} is expressed as

$$T_{\text{mw}}^{\text{model}} = \frac{{}_2F_1(3/2, 3\beta\gamma/2; 5/2; -1/q_J^2)}{{}_2F_1(3/2, 3\beta/2; 5/2; -1/q_J^2)} T_0. \quad (4.36)$$

In Figure 4.8, we plot T_{mw} , T_{ew} and T_{sl} as a function of β for the polytropic profile (Eq. [2.24]) and the cooling cluster model (Eq. [2.25]). Because the inner region is cooler (hotter) for the polytropic model (the cooling cluster model), T_{ew} and T_{sl} are larger (smaller) than T_{mw} for the wide range of β . Thus the mass-weighted temperature is highly sensitive to the radial profile.

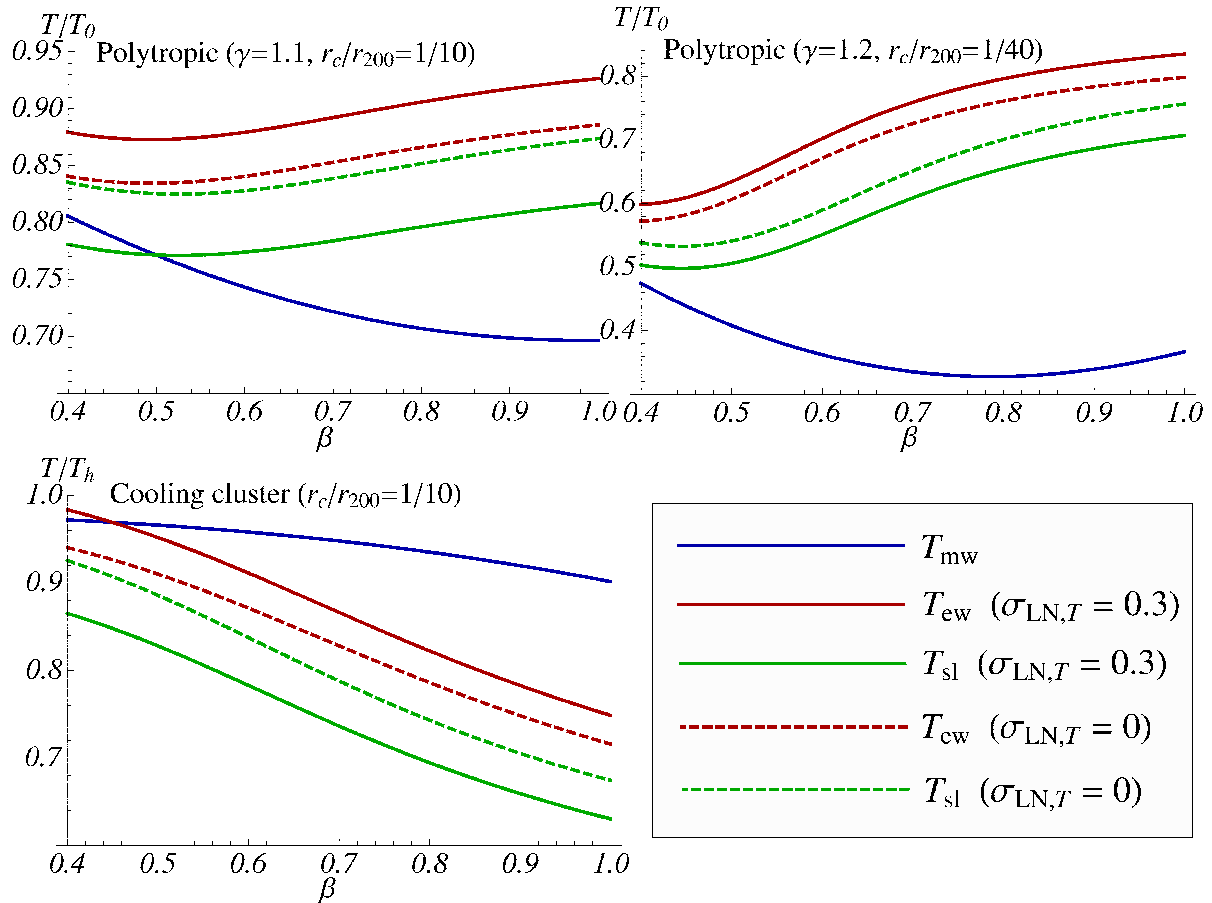


Figure 4.8: The relation of T_{mw} , T_{ew} and T_{sl} for the β model. Each color shows the different definition of temperature (blue, red, and green correspond to T_{mw} , T_{ew} , and T_{sl} , respectively). Left and right top panels indicates the polytropic model of the temperature profile, while bottom left panel is the cooling cluster model with $(T_h - T_l)/T_l = 1.5$ and $\mu = 2$. Each temperature is normalized by the central temperature T_0 for the polytropic model or the temperature at an infinite limit T_h for the cooling cluster model.

4.6 Summary

In this chapter, we have explored the origin of the bias in the spectroscopic temperature of simulated galaxy clusters discovered by Mazzotta et al. (2004). Using the independent simulations data, we have constructed mock spectra of clusters, and confirmed their results; the spectroscopic

temperature is systematically lower than the emission-weighted temperature by 10-20% and that the spectroscopic-like temperature defined by equation (4.4) approximates the spectroscopic temperature to better than $\sim 6\%$.

With the lognormal approximation of inhomogeneities described in §3, we have developed an analytical model that explains the bias in the spectroscopic temperature. Based on this model, we have found that not only the radial profiles but also the local inhomogeneities are largely responsible for the above mentioned bias of cluster temperatures. We conclude that the multi-phase nature of the ICM plays an essential role in producing the systematic bias in spectroscopic temperature.

Chapter 5

The Hubble Constant Measurement from the Sunyaev-Zel'dovich effect

5.1 Discrepancy between the Hubble Constant Estimates from Clusters and Other Observations

Galaxy clusters constitute an important cosmological probe, in particular in determining the Hubble constant H_0 through the combined analysis of the SZE and X-ray observations. Recent high-resolution X-ray and radio observations enable one to construct a statistical sample of clusters for the H_0 measurement. Carlstrom et al. (2002) compiled the previous results of 38 distance determination to 26 different galaxy clusters, and obtained $H_0 = 60 \pm 3 \text{ km s}^{-1} \text{ Mpc}^{-1}$ (Reese et al., 2002; Uzan et al., 2004, but see Bonamente et al. 2006). Despite its relatively large individual errors, the mean value of H_0 estimated from the SZE and X-ray appears systematically lower than those estimated with the distance to Cepheids and the CMB anisotropy (Table 5.1).

Table 5.1: The Hubble constant estimates from different observations

Observation	H_0 [$\text{km s}^{-1} \text{ Mpc}^{-1}$]	Reference
Galaxy clusters	60 ± 3	Carlstrom et al. (2002)
The distance to Cepheids	72 ± 8	Freedman et al. (2001)
The CMB anisotropy	73 ± 3	Spergel et al. (2007)

Although possible systematic errors in the H_0 measurement from the SZE, including the finite extension, clumpiness, asphericity, and non-isothermality, have been extensively studied by several authors (Inagaki et al., 1995; Kobayashi et al., 1996; Yoshikawa et al., 1998; Hughes & Birkinshaw, 1998; Birkinshaw, 1999; Wang & Fan, 2006), they were not able to identify any systematic error that affects the estimate of H_0 by 10-15 percent. Therefore it has been generally believed that the reliability of H_0 from the SZE is dominated by the statistics. Given that, the 10-15 percent underestimate bias mentioned above, if real, needs to be explained in terms

of additional ICM physics, such as inhomogeneity, beyond the simple models used in previous studies.

In this chapter, we apply the lognormal model of the ICM inhomogeneity to the Hubble constant measurement from the SZE and X-ray. The aim of this chapter is to examine the systematic error of the Hubble constant measurement on the basis of the lognormal model and the temperature underestimate bias described in chapter 4.

5.2 Estimating H_0 from the SZE in the Spherical Isothermal β Model

A conventional estimate of H_0 from the SZE is based on the assumptions that the gas temperature is isothermal, $T(r) = T_{\text{cl}}$ ($= \text{const.}$), and that the gas density follows the β model (Eq. [2.16]). These approximations are insufficient to model the full complexity of real galaxy clusters. It has been (implicitly) assumed that the average over a number of clusters should significantly reduce the resulting error in the estimate of H_0 . While we quantitatively argue below that this is not the case, we summarize here the commonly adopted estimator for H_0 in the spherical isothermal β model (Inagaki et al., 1995; Kobayashi et al., 1996).

In this idealistic model, the X-ray surface brightness and y -parameter of SZE at an angle θ from the center of cluster are given by equations (2.21) and (2.52). Here, we show these equations again:

$$S_x(\theta) = \frac{\Lambda_X(T_{\text{cl}})x_H n_0^2 r_c G(\beta)}{4\pi(1+z)^4} \left[1 + \left(\frac{\theta}{\theta_c} \right)^2 \right]^{-3\beta + \frac{1}{2}} \quad (5.1)$$

$$y(\theta) = \frac{n_0 \sigma_T k_B T_{\text{cl}} r_c G(\beta/2)}{m_e c^2} \left[1 + \left(\frac{\theta}{\theta_c} \right)^2 \right]^{-\frac{3}{2}\beta + \frac{1}{2}}, \quad (5.2)$$

where $G(\beta)$ is the function defined by equation (2.22).

Combining equations (5.1) and (5.2), one can eliminate n_0 and estimate the core radius as

$$r_{\text{c,iso}\beta}(T_{\text{cl}}) = \frac{y(0)^2}{S_x(0)} \frac{m_e^2 c^4 x_H \Lambda_X(T_{\text{cl}})}{4\pi(\sigma_T k T_{\text{cl}})^2 (1+z)^4} \frac{G(\beta)}{[G(\beta/2)]^2}, \quad (5.3)$$

where $S_x(0)$ and $y(0)$ denote the values at $\theta = 0$, the line-of-sight through the center of the galaxy cluster. Note that the right-hand-side of equation (5.3) is written entirely in terms of observable quantities.

Equation (5.3) corresponds to the estimate of the core radius along the line-of-sight. If the cluster is spherically symmetric, it should be equal to the core radius in the plane of the sky. With the assumption, the measured angular core radius, $\theta_{\text{c,fit}}$, is related to the physical core radius simply by

$$r_{\text{c,fit}} = \theta_{\text{c,fit}} d_A(z) \quad (5.4)$$

with $d_A(z)$ being the angular diameter distance of the cluster at z . Equations (5.3) and (5.4) may be combined to estimate the angular diameter distance to the cluster (Silk & White, 1978):

$$d_{A,\text{est}}(z) \equiv \frac{r_{c,\text{iso}\beta}}{\theta_{c,\text{fit}}}. \quad (5.5)$$

If one obtains $d_{A,\text{est}}(z)$ for a number of clusters at different redshifts, one can estimate cosmological parameters by fitting to the angular diameter distance vs. redshift relation, $d_A(z)$. In what follows, however, we consider the above methodology for the purpose of estimating H_0 . Thus following Inagaki et al. (1995), we introduce the ratio of the estimated to the true value of H_0 :

$$f_H = \frac{d_A}{d_{A,\text{est}}} = \frac{H_{0,\text{est}}}{H_{0,\text{true}}} = \frac{r_\perp}{r_\parallel}. \quad (5.6)$$

Equations (5.3) and (5.4) provide commonly used estimators for the radius of clusters along and perpendicular to the line-of-sight, r_\parallel , and r_\perp , respectively, but they are model-dependent and ill-defined for generic non-spherical clusters. We come back to this issue below (§§5.4 and 5.5). Note that $f_H > 1$ (< 1) corresponds to overestimating (underestimating) the true H_0 .

Given the approximations underlying the spherical isothermal β model, it is not surprising that f_H for an individual cluster deviates from unity. A more relevant question is whether the average over a number of clusters, $\langle f_H \rangle$, is still systematically larger or smaller than unity. If such systematic errors exist, can we correct for them by identifying their physical origin? This is what we address in this chapter.

In fact there have been several previous attempts toward the same goal, mainly utilizing numerically simulated galaxy clusters (Inagaki et al., 1995; Yoshikawa et al., 1998; Sulkanen, 1999). They concluded that departure from the sphericity and the isothermality of clusters results in $f_H \neq 1$, but after averaging over a sample the systematic errors are relatively small, $|\langle f_H \rangle - 1| \approx 5\%$. Our analysis below is different from the previous ones in adopting the spectroscopic temperature, T_{spec} , for T_{cl} . Indeed T_{cl} is a somewhat ambiguous quantity for actual clusters (not isothermal). It has been common in this field to assume that the emission-weighted temperature T_{ew} (Eq. [4.3]) is approximately equal to T_{spec} (the above integration is carried out over the entire cluster volume). Thus, the previous conclusion is entirely based on the assumption that $T_{\text{cl}} = T_{\text{ew}}$. As seen in chapter 4, however, Mazzotta et al. (2004) and Rasia et al. (2005) pointed out that T_{spec} , estimated by fitting the thermal continuum and the emission lines of the X-ray spectrum, is systematically lower than T_{ew} . Furthermore, in chapter 4, we have shown that the difference between T_{ew} and T_{spec} could be explained through an analytic model of the temperature profile and inhomogeneities in the ICM. We evaluate f_H applying the model and then comparing the numerical simulations in the subsequent sections.

5.3 Analytic Modeling of Systematic Errors of H_0 for Spherical Clusters

Identifying possible systematic errors in the estimate of H_0 for realistic clusters is inevitably complicated. In order to address the problem as analytically as possible, we consider spherical clusters that follow the β model (Eq. [2.16]) and a polytropic temperature profile (Eq. [2.24])

but with lognormal density and temperature fluctuations. While the approach in this section is not entirely generic, it is useful in understanding the physical origin of systematic errors. The present analytic modeling is tested against numerically generated triaxial cluster samples in §5.4, and against those from cosmological hydrodynamic simulations in §5.5.

Our task here is to derive analytic expressions for more general cases, which correspond to equations (5.1) to (5.3) in the case of the isothermal β model. Let us consider first the effect of inhomogeneities in ICM. The X-ray surface brightness at the center of the cluster is written as an integral over the line-of-sight:

$$S_x(0) = \frac{1}{4\pi(1+z)^4} \int x_H n(\mathbf{r})^2 \Lambda_X(T(\mathbf{r})) dr. \quad (5.7)$$

In chapter 3, we have shown that the fluctuation fields defined as $\delta_n = n(\mathbf{r})/n(r)$ and $\delta_T = T(\mathbf{r})/T(r)$ are approximately independent and follow the r -independent log-normal PDF, $P_{\text{LN}}(\delta_n; \sigma_{\text{LN},n})$ and $P_{\text{LN}}(\delta_T; \sigma_{\text{LN},T})$ given by equation (3.6). The average of equation (5.7) over many independent lines-of-sight can then be computed by integrating over the log-normal PDFs. If we further assume that the cooling function, $\Lambda_X(T)$, is dominated by thermal bremsstrahlung (bolometric), $\Lambda_{\text{brems}}(T) \propto \sqrt{T}$, we can rewrite equation (5.7) as

$$\begin{aligned} S_x(0) &= \frac{1}{4\pi(1+z)^4} \int \delta_n^2 \delta_T^{1/2} P_{\text{LN}}(\delta_n) P_{\text{LN}}(\delta_T) d\delta_n d\delta_T \int x_H n(r)^2 \Lambda_{\text{brems}}(T(r)) dr \\ &= \frac{\exp(\sigma_{\text{LN},n}^2 - \sigma_{\text{LN},T}^2/8)}{4\pi(1+z)^4} \int x_H n(r)^2 \Lambda_{\text{brems}}(T(r)) dr. \end{aligned} \quad (5.8)$$

On the contrary, their fluctuations do not affect $y(0)$ because the integrand of the y -parameter is a linear function of both temperature and density. Thus the inhomogeneity effect is well described by the factor:

$$\chi_\sigma \equiv \exp(\sigma_{\text{LN},n}^2 - \sigma_{\text{LN},T}^2/8). \quad (5.9)$$

Assuming the polytropic model of temperature (Eq. [2.24]), we obtain

$$\begin{aligned} S_x(0) &= \chi_\sigma \frac{1}{4\pi(1+z)^4} \int x_H n(r)^2 \Lambda_{\text{brems}}(T(r)) dr \\ &= \chi_\sigma \frac{\Lambda_{\text{brems}}(T_0) x_H n_0^2 r_c G(\beta(\gamma+3)/4)}{4\pi(1+z)^4}, \end{aligned} \quad (5.10)$$

and

$$y(0) = \frac{n_0 \sigma_T k T_0 r_c G(\beta\gamma/2)}{m_e c^2}, \quad (5.11)$$

respectively. Therefore, the core radius in this model is written as

$$r_{c,\text{polyLN}} = \chi_\sigma \frac{y(0)^2}{S_x(0)} \frac{m_e^2 c^4 x_H \Lambda_{\text{brems}}(T_0)}{4\pi(\sigma_T k T_0)^2 (1+z)^4} \frac{G(\beta(\gamma+3)/4)}{[G(\beta\gamma/2)]^2}. \quad (5.12)$$

If one attempts to fit the X-ray surface brightness profile under the assumption of the isothermal β model, the fitted value of the β parameter should be

$$\beta_{\text{fit}} = \frac{\beta(\gamma + 3)}{4}, \quad (5.13)$$

since $\Lambda_{\text{brems}}[T(r)]n(r)^2 \propto T(r)^{1/2}n(r)^2 \propto [n(r)^{(\gamma+3)/4}]^2$. In addition, the fitted temperature should be equal to the spectroscopic temperature T_{spec} . Thus the estimated core radius is given by equation (5.3):

$$r_{\text{c,iso}\beta}(T_{\text{spec}}) = \frac{y(0)^2 m_e^2 c^4 x_{\text{H}} \Lambda_{\text{brems}}(T_{\text{spec}})}{S_{\text{x}}(0) 4\pi(\sigma_{\text{T}} k T_{\text{spec}})^2 (1+z)^4} \frac{G(\beta_{\text{fit}})}{[G(\beta_{\text{fit}}/2)]^2}. \quad (5.14)$$

Therefore the systematic bias in the estimate of the Hubble constant in this particular model should be

$$\begin{aligned} f_{\text{H,polyLN|iso}\beta} &= \frac{r_{\text{c,polyLN}}}{r_{\text{c,iso}\beta}(T_{\text{spec}})} = \chi_{\sigma} \frac{\Lambda_{\text{brems}}(T_0)/T_0^2}{\Lambda_{\text{brems}}(T_{\text{spec}})/T_{\text{spec}}^2} \frac{G(\beta(\gamma + 3)/4)}{[G(\beta\gamma/2)]^2} \frac{[G(\beta_{\text{fit}}/2)]^2}{G(\beta_{\text{fit}})} \\ &= \chi_{\sigma} \frac{\Lambda_{\text{brems}}(T_0)/T_0^2}{\Lambda_{\text{brems}}(T_{\text{spec}})/T_{\text{spec}}^2} \left[\frac{G(\beta(\gamma + 3)/8)}{G(\beta\gamma/2)} \right]^2 \equiv \chi_{\sigma} \chi_{\text{T}}(T_{\text{spec}}), \end{aligned} \quad (5.15)$$

where we define χ_{T} to express the effect of the temperature structure in the ICM.

It may be more instructive to rewrite equation (5.15) as

$$f_{\text{H,polyLN|iso}\beta} = \chi_{\sigma} \chi_{\text{T}}(T_{\text{ew}}) \frac{\chi_{\text{T}}(T_{\text{spec}})}{\chi_{\text{T}}(T_{\text{ew}})}, \quad (5.16)$$

since T_{cl} was often assumed to be equal to T_{ew} . Equation (5.16) makes it clear that the systematic bias in the estimate of H_0 results from three major effects; χ_{σ} due to inhomogeneities in the ICM, $\chi_{\text{T}}(T_{\text{ew}})$ representing the temperature structure assuming that $T_{\text{cl}} = T_{\text{ew}}$, and finally $\chi_{\text{T}}(T_{\text{spec}})/\chi_{\text{T}}(T_{\text{ew}})$ coming from the difference between the spectroscopic and the emission-weighted temperatures of the ICM.

Those three factors can be expressed in an approximate but analytic fashion as follows. If we adopt the log-normal PDF for the density and temperature inhomogeneities in the ICM, $\chi_{\sigma} = \exp(\sigma_{\text{LN},n}^2 - \sigma_{\text{LN},T}^2/8)$ (Eq.[5.9]). As shown in Table 3.1, cosmological hydrodynamic simulations indicate that $\sigma_{\text{LN},n} \approx 0.2\text{--}0.5$ and $\sigma_{\text{LN},T} \approx 0.2\text{--}0.3$. Thus $\chi_{\sigma} \approx 1.04\text{--}1.3$. The second factor can be estimated by using the analytical relation of T_0 and T_{ew} given by equations (4.29) and (4.30):

$$T_{\text{ew}}/T_0 = \exp(\sigma_{\text{LN},T}^2/2) J(\beta, \gamma, r_c/r_{\text{vir}}; 1/2), \quad (5.17)$$

where $J(\beta, \gamma, q_J; x_J)$ is the function defined by equation (4.30), and we assume that the cluster has a finite extension and $n(r) = 0$ for radius r beyond the virial radius of the cluster, r_{vir} . Just for simplicity, we neglect the term, $\exp(\sigma_{\text{LN},T}^2/2)$, which represents the temperature inhomogeneity because it is relatively small for $\sigma_{\text{LN},T} \approx 0.2 - 0.3$. If we further adopt $\Lambda_{\text{brems}}(T) \propto \sqrt{T}$ then $\chi_{\text{T}}(T_{\text{ew}})$ reduces to

$$\chi_{\text{T}}(T_{\text{ew}}) \approx \left(\frac{T_{\text{ew}}}{T_0} \right)^{1.5} \frac{[G(\beta(\gamma + 3)/8)]^2}{[G(\beta\gamma/2)]^2}$$

$$= J(\beta, \gamma, r_c/r_{\text{vir}}; 1/2)^{1.5} \frac{[G(\beta(\gamma+3)/8)]^2}{[G(\beta\gamma/2)]^2}. \quad (5.18)$$

The result is plotted in Figure 5.1 for typical values of the parameters, and indicates that $\chi_{\text{T}}(T_{\text{ew}})$ ranges from 0.8 to 1.0 for $\beta = 0.5 - 0.8$ and $\gamma = 1.1 - 1.2$.

Similarly the third factor can be approximated as

$$\chi_{\text{spec-ew}} \equiv \frac{\chi_{\text{T}}(T_{\text{spec}})}{\chi_{\text{T}}(T_{\text{ew}})} = \frac{T_{\text{spec}}^2}{T_{\text{ew}}^2} \frac{\Lambda_{\text{brems}}(T_{\text{ew}})}{\Lambda_{\text{brems}}(T_{\text{spec}})} \approx \left(\frac{T_{\text{spec}}}{T_{\text{ew}}} \right)^{1.5}. \quad (5.19)$$

Several studies confirmed the systematic underestimate of the spectroscopic temperature relative to the emission-weighted temperature, $T_{\text{spec}}/T_{\text{ew}} = 0.8 - 0.9$ from cosmological hydrodynamic simulations (Table 4.2; Rasia et al., 2005; Kay et al., 2007b). If $T_{\text{spec}}/T_{\text{ew}} = 0.8$ (0.9), for instance, $\chi_{\text{spec-ew}}$ amounts to 0.7 (0.85).

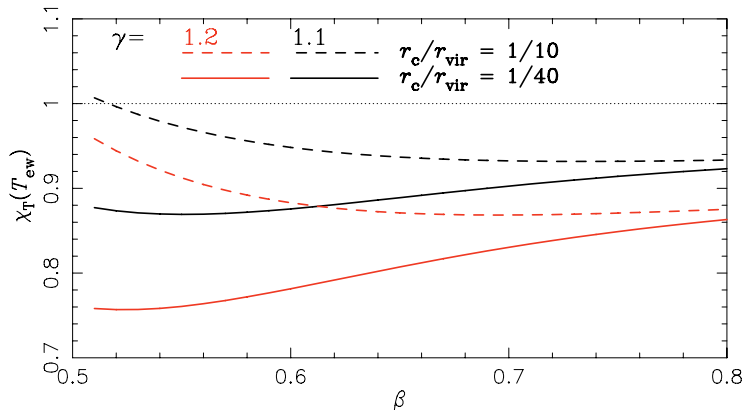


Figure 5.1: The bias of H_0 due to the temperature profile (Eq.5.18) as a function of β . Dashed and solid curves correspond to the cases that core radius is 10 percent and 2.5 percent of the virial radius, respectively. Red and black colors indicate the polytropic index $\gamma = 1.2$ and 1.1, respectively.

5.4 Numerical Modeling of Systematic Errors of H_0 for Inhomogeneous and Triaxial Clusters

So far, we have only considered spherical clusters, but asphericity is another important source of error in the estimation of H_0 . The errors are expected to be significantly reduced by averaging over a statistical sample of clusters randomly oriented with respect to our line-of-sight. Nevertheless, if clusters preferentially take either prolate or oblate shapes, for instance, the residual errors may not be entirely negligible. Thus, we address the effect of asphericity on the basis of the triaxial approximation for the cluster ICM (Hughes & Birkinshaw, 1998; Jing & Suto, 2002; Lee & Suto, 2003, 2004).

To quantitatively investigate the combined effects of gas inhomogeneity and asphericity, we numerically create three sets of cluster samples and perform mock observations of Monte-Carlo

realizations. The first is spherical, but include random gas density and temperature fluctuations according to the log-normal distribution. The second is triaxial without the fluctuations. Both the first and the second samples assume isothermality ($\gamma = 1$). The third set corresponds to the model described in chapter 3 except for added asphericity; the log-normal fluctuations, the polytropic temperature structure, and the triaxiality are included. We call these sample sets *model clusters* in order to distinguish them from *simulated clusters* extracted from cosmological hydrodynamic simulations (§5.5).

Each model cluster is constructed on 512^3 grid points within a $6 \text{ h}^{-1}\text{Mpc}$ cubic region around the center. We first create spherically symmetric clusters with gas density profiles following equation (2.16), with $\beta = 0.65$, $r_c = 100 \text{ h}^{-1}\text{kpc}$, and $n_0 = 10^{-2} \text{ cm}^{-3}$. The gas is fiducially isothermal with $T = 5 \text{ keV}$; we also consider the case of polytropic temperature profile with $T_0 = 7 \text{ keV}$ and $\gamma = 1.2$. We then add random fluctuations of gas density and temperature according to the r -independent log-normal distributions. The X-ray emissivity is computed with SPEX version 2.0 assuming CIE, an energy range of $0.5 - 10.0 \text{ keV}$ and a constant metallicity of $0.3Z_\odot$. Triaxial model clusters are constructed simply by stretching spherical clusters along the three axis directions by a factor of λ_a , λ_b , and λ_c , respectively.

In mock observations, we extract the quantities necessary to compute $r_{c,\text{iso}\beta}(T_{\text{cl}})$ and $r_{c,\text{fit}}$ via equations (5.3) and (5.4) in the following manner. We first fit the projected profiles of $S_x(\theta)$ with a functional form $S_x(0)[1 + (r/r_{c,\text{fit},S_x})^2]^{-3\beta_{\text{fit}}+1/2}$ from $r = 0$ to $r = 1 \text{ h}^{-1}\text{Mpc}$ over 1024 random LOSs toward each cluster. For each LOS, we also compute $y(0)$ and, unless otherwise stated, use it directly in our analysis. We discuss other methods of obtaining $y(0)$ in §5.5.2. As will be described below, the gas temperature T_{cl} is obtained by either fitting the mock X-ray spectra or simply using the input temperature, depending on the purpose of the analysis. We use the template of the spectral energy distribution computed using SPEX 2.0 assuming collisional ionization equilibrium, an energy range of $0.5 - 10.0 \text{ keV}$ and a constant metallicity of $0.3Z_\odot$. Assuming that $r_{\parallel} = r_{c,\text{iso}\beta}(T_{\text{cl}})$ and $r_{\perp} = r_{c,\text{fit},S_x}$, we calculate f_H for each LOS.

To quantify the bias due to the projection effect, we also compute the volume-averaged radial profile of the gas density, directly from the grid data within the radius $1 \text{ h}^{-1}\text{Mpc}$. By fitting the profile to the β model, we obtain the estimated core radius $r_{c,\text{fit},3\text{D}}$, which is independent of LOS. We compare the values of f_H using $r_{\perp} = r_{c,\text{fit},3\text{D}}$ and r_{c,fit,S_x} in the discussion that follows.

Figure 5.2a shows the mean and rms values of f_H for spherical clusters with no temperature gradient. We consider two cases for the log-normal density and temperature fluctuations with $(\sigma_{\text{LN},n}, \sigma_{\text{LN},T}) = (0.5, 0.0)$ and $(0.5, 0.3)$. The latter set corresponds to the typical value for the simulated cluster (Table 3.1). To present the bias produced solely by gas inhomogeneities, we here adopt for T_{cl} the volume averaged temperature instead of fitting the mock X-ray spectra. It is evident that the fluctuations in gas density yield $f_H \sim 1.3$ (i.e. overestimating H_0 by $\sim 30\%$), while those in gas temperature do not contribute significantly to the bias. The mean value of f_H is in good agreement with our analytical expectation χ_σ (dashed horizontal lines). The bias due to the projection is $\sim 10\%$.

The bias produced by ellipsoidal shapes is displayed in Figure 5.2b for the two sets of the axis ratio ($\lambda_a : \lambda_b : \lambda_c = 0.6 : 0.7 : 1$ and $0.9 : 0.9 : 1$). These sets are the typical values of the simulated cluster. Again, to present the bias solely from asphericity, the gas is assumed to be isothermal without any fluctuations and we adopt $T_{\text{cl}} = T_0$ in computing f_H . The average bias is relatively small ($\lesssim 15\%$) and that due to the projection is $\sim 3\%$. These results indicate that

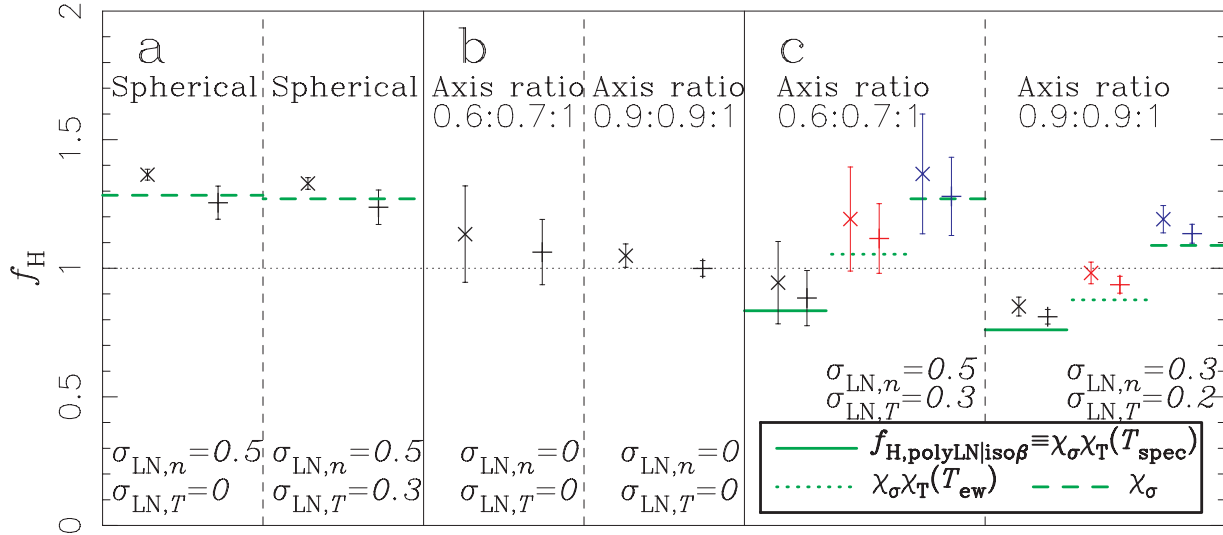


Figure 5.2: The average and rms of f_H of the model clusters; (a) spherical clusters with gas inhomogeneities and no temperature gradient, (b) ellipsoidal and isothermal clusters, and (c) ellipsoidal clusters with temperature gradient and gas inhomogeneities. Crosses and pluses denote f_H adopting $r_{\perp} = r_{c,\text{fit},\text{Sx}}$ and $r_{\perp} = r_{c,\text{fit},\text{3D}}$, respectively. Thick horizontal lines indicate analytical estimations for χ_{σ} (dashed), $\chi_{\sigma}\chi_{\text{T}}(T_{\text{ew}})$ (dotted), and $\chi_{\sigma}\chi_{\text{T}}(T_{\text{spec}})$ (solid). In panel (c), black symbols indicate f_H using $r_{c,\text{iso}\beta}(T_{\text{cl}} = T_{\text{spec}})$, red symbols $r_{c,\text{iso}\beta}(T_{\text{cl}} = T_{\text{ew}})$, and blue symbols $r_{c,\text{poly}\beta}$, which correspond to the isothermal fit with $T = T_{\text{spec}}$, the isothermal fit with $T = T_{\text{ew}}$, and the polytropic fit, respectively (see the main text for details).

the bias due to asphericity, after averaging over a statistical sample of clusters, is smaller than that from gas inhomogeneity.

Figure 5.2c illustrates the bias in a more realistic case; we create ellipsoidal clusters with a polytropic temperature profile and fluctuations. Two sets of axis ratio ($\lambda_a : \lambda_b : \lambda_c = 0.6 : 0.7 : 1$ and $0.9 : 0.9 : 1$) are chosen adopting $(\sigma_{\text{LN},n}, \sigma_{\text{LN},T}) = (0.5, 0.3)$ and $(0.3, 0.2)$, respectively. In this panel, we show the values of f_H based on the following three methods, so as to understand clearly the physical origin of the overall bias in the H_0 estimation.

The first method (black symbols in Fig. 5.2c) corresponds to the most conventional case of using the isothermal β -model and the spectroscopic temperature T_{spec} . To obtain T_{spec} we fit the mock X-ray spectra from the central ($r < 1 \text{ h}^{-1}\text{Mpc}$) region of each cluster using XSPEC assuming a single temperature MEKAL model. We assume the perfect response, and ignore its effect on the spectral temperature (§4.2). Clearly, the value of H_0 is *underestimated* by ~ 10 -20%. This is in good agreement with our analytical estimation for $f_{\text{H,polyLN|iso}\beta} = \chi_\sigma \chi_{\text{T}}(T_{\text{spec}})$ for a spherical cluster (solid horizontal lines). To obtain $\chi_{\text{T}}(T_{\text{spec}})$, we compute the volume-averaged profile of the density and the temperature. These profile are fitted to equation (2.16) and equation (2.24) taking $n_0, r_{\text{c,fit,3D}}, \beta, T_0$ and γ as free parameters. We use the adopted values $(\sigma_{\text{LN},n}, \sigma_{\text{LN},T}) = (0.5, 0.3)$ and $(0.3, 0.2)$ to compute χ_σ .

The second method (red symbols in Fig. 5.2c) aims to mimic previous numerical studies of the H_0 bias (Inagaki et al., 1995; Yoshikawa et al., 1998) and adopts the isothermal β -model and the emission-weighted temperature T_{ew} . We obtain T_{ew} by directly summing up the temperature of each grid point from the central ($r < 1 \text{ h}^{-1}\text{Mpc}$) region. Also plotted for comparison is an analytical estimate $\chi_\sigma \chi_{\text{T}}(T_{\text{ew}})$ (dotted lines). The values of χ_σ and $\chi_{\text{T}}(T_{\text{ew}})$ are computed as described above. In this case, χ_σ and $\chi_{\text{T}}(T_{\text{ew}})$ practically cancel each other, and f_H is close to unity, consistent with the previous findings of Inagaki et al. (1995) and Yoshikawa et al. (1998). This shows that the absence of the bias in previous studies is simply an artifact of using T_{ew} , which is systematically larger than T_{spec} .

The third method (blue symbols in Fig. 5.2c) attempts to eliminate the bias due to the temperature gradient by using the polytropic profile to estimate the core radius (Ameglio et al., 2006) :

$$r_{\text{c,poly}\beta} = \frac{y(0)^2}{S_x(0)} \frac{m_e^2 c^4 x_{\text{H}} \Lambda_{\text{X}}(T_0)}{4\pi(\sigma_{\text{T}} k T_0)^2 (1+z)^4} \frac{G(\beta\gamma/4 + 3\beta/4)}{[G(\beta\gamma/2)]^2}, \quad (5.20)$$

where we adopt T_0 and γ from fitting the volume-averaged temperature profile of the model clusters. The value of β is obtained from equation (5.13) using β_{fit} and γ . The value of f_H so obtained should represent the bias arising from sources *other than* the spectral fitting and the temperature gradient. Given the good agreement with the analytical estimate for χ_σ (dashed lines), we conclude that the bias in this case is dominated by the effect from gas inhomogeneities.

In summary, there are three major sources for the bias of H_0 ; the spectral fitting, the temperature gradient, and local density fluctuations. The first two lead to an *underestimate* while the latter leads to an *overestimate* of H_0 . In every case studied here, the bias due to asphericity is much smaller than any of these three.

5.5 Comparison with Clusters from Cosmological Hydrodynamic Simulations

We now compare the bias described in the previous section with simulated clusters described in § 3.2.

We perform mock observations over 1024 LOSs for each simulated cluster in a manner similar to that described in §5.4 except for the following points. First, we compute T_{spec} and T_{ew} within the virial radius instead of $1 \text{ h}^{-1}\text{Mpc}$. Second, we use the fitted value of $\sigma_{\text{LN},n}$ and $\sigma_{\text{LN},T}$ in calculating χ_σ of the analytical model.

Table 5.2: Axis ratio and the ratio of $\langle r_{\text{c,fit,Sx}} \rangle$ and $r_{\text{c,fit,3D}}$ of the six simulated clusters.

	λ_a/λ_c	λ_b/λ_c	$\langle r_{\text{c,fit,Sx}} \rangle / r_{\text{c,fit,3D}}$
Coma	0.59	0.64	1.03 ± 0.14
Perseus	0.49	0.61	1.04 ± 0.18
Virgo	0.44	0.61	1.16 ± 0.31
Centaurus	0.68	0.78	1.03 ± 0.13
A3627	0.79	0.83	1.08 ± 0.06
Hydra	0.84	0.93	1.03 ± 0.05

5.5.1 Results

Figure 5.3 displays a set of histograms of f_H for the simulated Coma cluster. The same analysis is done for the other five clusters. Histograms in different colors correspond to the symbols of the same color in Figure 5.2c, and indeed show similar trends for each component of the bias. Since the physical length of clusters along the LOS is not symmetrically distributed around its mean, the corresponding histograms of f_H are skewed positively. In Appendix C, we compute the distribution for the two extreme cases, the prolate and the oblate ellipsoids, and find that they yield positively and negatively skewed distributions, respectively. Indeed this is consistent with the fact that the simulated Coma is nearly prolate (Table 5.2).

The (simple arithmetic) mean, $\langle f_H \rangle$ is plotted in Figure 5.4 for six simulated clusters. The quoted error bars indicate 1σ standard deviation from the mean. Except for the simulated Virgo cluster, $\langle f_H \rangle$ is below unity, i.e., H_0 is *underestimated*. It is remarkable that a simple analytical model for systematic effects (solid, dotted and dashed horizontal lines) described in §5.3 can reproduce the bias in the simulated clusters.

We have made sure that the bias from other sources is minor; first, if a cluster has a finite extension and is bounded within the virial radius, the value of $\langle f_H \rangle$ becomes smaller by $\lesssim 5\%$ (open circles in Fig. 5.4). Second, we compute the axis ratio ($\lambda_a < \lambda_b < \lambda_c$) of each simulated cluster, basically following the method of Jing & Suto (2002), but using the gas density not the dark matter density. The isodensity surfaces corresponding to the gas densities of $n_e = 3 \times 10^{-3}$, 1×10^{-3} , 5×10^{-4} , 3×10^{-4} , and $1 \times 10^{-4} \text{ [cm}^{-3}\text{]}$ are shown in Figure 3.1. After eliminating substructures, the axis ratio is calculated by diagonalizing the inertial tensor of each surface.

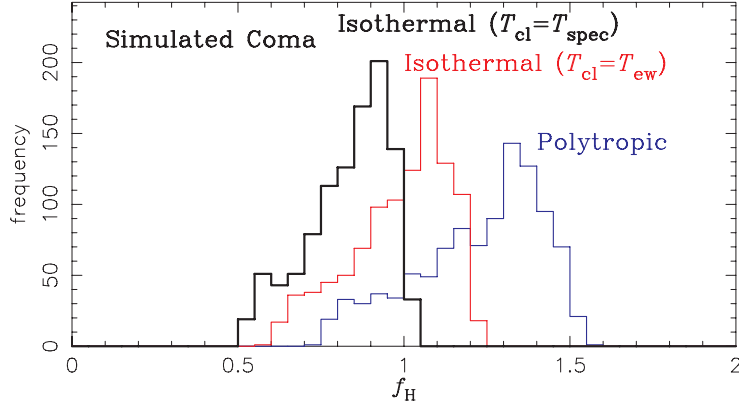


Figure 5.3: Distribution of f_H over 1024 LOSs for the simulated Coma cluster. Black, red and blue histograms indicate the results for the isothermal fit with $T = T_{\text{spec}}$, the isothermal fit with $T = T_{\text{ew}}$, and the polytropic fit, respectively.

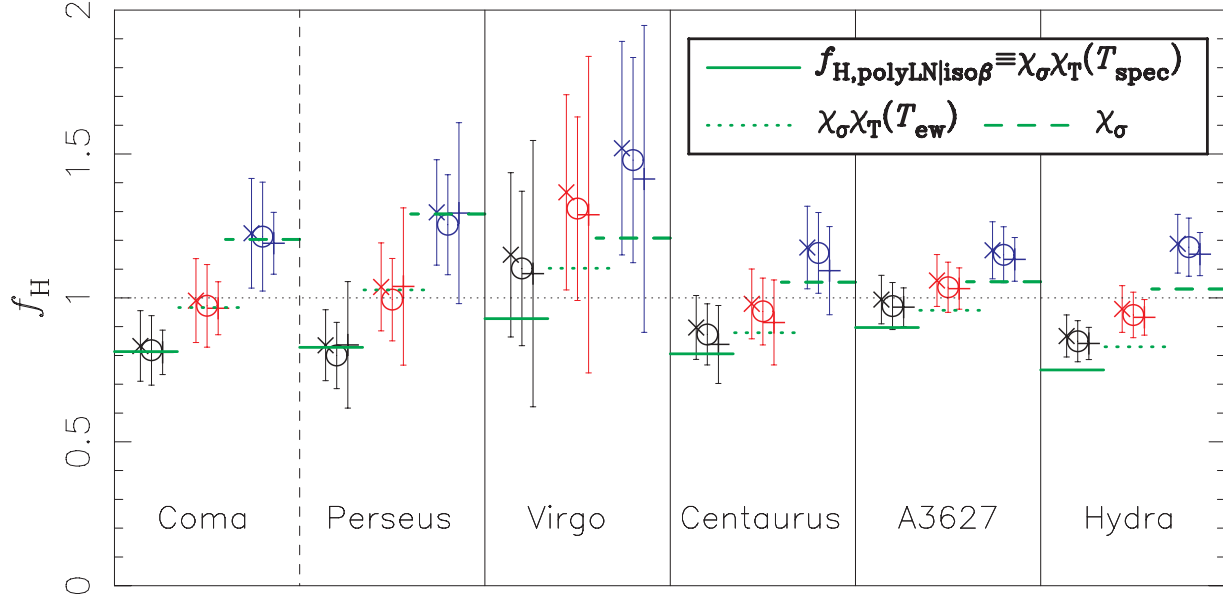


Figure 5.4: The average and rms of f_H for the six simulated clusters. Black, red and blue symbols with error-bars indicate the results for the isothermal fit with $T = T_{\text{spec}}$, the isothermal fit with $T = T_{\text{ew}}$, and the polytropic fit, respectively. Crosses and pluses denote f_H adopting $r_{\perp} = r_{\text{c,fit,Sx}}$ and $r_{\perp} = r_{\text{c,fit,3D}}$, respectively. Open circles indicate f_H adopting $r_{\perp} = r_{\text{c,fit,Sx}}$ but assuming that the clusters are not extended beyond the virial radius. Thick green horizontal lines indicate analytical estimations for χ_{σ} (dashed), $\chi_{\sigma}\chi_T(T_{\text{ew}})$ (dotted), and $\chi_{\sigma}\chi_T(T_{\text{spec}})$ (solid).

The averaged axis ratios of the five different density regions (Table 5.2) are similar to the typical value adopted in §5.4. Therefore, we conclude that the spherical approximation itself is not a major source of the bias for the simulated cluster. Finally, the bias due to the projection is small (crosses and pluses in Fig. 5.4). We list in Table 5.2 the average values of r_{c,fit,S_x} over 1024 LOSs relative to $r_{c,\text{fit},3D}$. The ratio is unity within 10 % (except for Virgo that has a relatively large dispersion), and basically all are consistent with unity within the uncertainty.

It is interesting to emphasize here that the shape of the distribution of f_H reflects the shape of clusters from the perspective of measuring the three-dimensional shape of clusters (Serenio et al., 2006, e.g.). If all clusters had the same shape, the observation of one cluster toward *multiple directions* might correspond to that of *multiple clusters* toward each LOS. Of course, the real shapes vary from cluster to cluster. However, if clusters tend to be prolate (oblate) preferentially, the distribution of $H_{0,\text{est}}$ should be skewed positively (negatively) as shown in Appendix C. Therefore, independently of the knowledge of real value of $H_{0,\text{true}}$, the statistical information about the shape distribution may be obtained *in principle* from the distribution of $H_{0,\text{est}}$.

5.5.2 Comparison with previous studies

The above results are consistent with the previous results of $f_H \sim 1$ with $T_{\text{cl}} = T_{\text{ew}}$ (Inagaki et al., 1995; Yoshikawa et al., 1998). On the other hand, Ameglio et al. (2006) explored the bias of d_A using the cosmological hydrodynamic simulations, and reported that H_0 is *overestimated* by more than a factor of two if one adopts the isothermal β model. This is opposite to our conclusion here, and we found that this should be ascribed to the sensitivity of f_H to the adopted values of $y(0)$, i.e., $f_H \propto d_{A,\text{est}}^{-1} \propto y^{-2}(0)$ as explained below.

Ameglio et al. (2006) obtained $y(0)$ by fitting the noise-less profile of $y(\theta)$ up to R_{500} fixing other β -model parameters from the X-ray profile, while we directly use the projected values of $y(0)$ in the simulation data. The difference between these two methods is apparent in Figure 5 (right panel) of Ameglio et al. (2006); their fit (solid line) was affected largely by the data points at large radii and yielded a value of $y(0)$ smaller by $\sim 50\%$ than the actual data. This enhances the value of f_H by more than a factor of 2, and indeed accounts for their apparently opposite conclusions. We have checked that other differences between their analysis and ours (the use of mass-weighted temperature for T_{cl} and the removal of the cluster central region) do not affect the results significantly.

As far as the bias in the previous SZE observations is concerned, we believe that our method is more relevant to what has been done with the real data, because these observations were not capable of constraining the radial profile of the y -parameter up to large radii with high S/N (see Komatsu et al., 2001; Kitayama et al., 2004, for the currently highest angular-resolution observation of the SZE).

We have further made sure that the effects of the finite spatial resolution of the observations and the central cooling region, which were neglected in our preceding analysis, are minor; first, we have evaluated $y(0)$ by fitting $y(\theta)$ within a radius of $100 h^{-1}\text{kpc}$ and $200 h^{-1}\text{kpc}$. These approximately correspond to the typical angular resolution of the SZE observation (~ 1 minute) at $z = 0.1$ and $z = 0.3$, respectively. The values of β and θ_c are fixed from the X-ray profile. For the six simulated clusters, the resulting values of f_H differ from our initial analysis (see Fig. 5.4) by -6% to $+7\%$ ($+2\%$ on average) for $r < 100h^{-1}\text{kpc}$, and by -3% to $+10\%$ ($+5\%$ on average)

for $r < 200h^{-1}\text{kpc}$.

Second, we have also performed the fitting separately for the X-ray and SZE profiles. The values of S_x , β and θ_c are evaluated by fitting $S_x(\theta)$ with equation (5.1), while that of $y(0)$ is obtained by fitting $y(\theta)$ with equation (5.2) independently of the X-ray profile. As a result, the values of f_H differ from those of Figure 5.4 by -6% and $+1\%$ (-3% on average).

Note that observationally there are several different ways to evaluate $y(0)$, $S_x(0)$, β and θ_c . A conventional method is to fit the X-ray imaging data $S_x(\theta)$ first. Then the SZ image is fitted to obtain $y(0)$ assuming the values of β and θ_c from the X-ray data. Our analysis procedure adopted here follows the conventional method. While Reese et al. (2002) have determined d_A from the joint fit to the X-ray and SZE imaging data, the result is almost equivalent to the conventional method since the X-ray imaging data have a much higher S/N than the SZE data.

5.6 Summary

In this chapter, we have considered various possible systematic errors of H_0 from the combined analysis of the SZE and X-ray observations. In particular we addressed the validity and limitation of the spherical isothermal β model in estimating H_0 , which has been used widely as a reasonable approximation after averaging over a number of clusters. We introduced the ratio of the estimated to the true Hubble constant, f_H , to characterize the systematic errors. We constructed an analytic model for f_H , and identified three important sources for the systematic errors; density and temperature inhomogeneities in the ICM, the temperature profile, and departures from sphericity. Except for the non-spherical effect, the most important analytical expression that summarizes our conclusion is equation (5.16), or equivalently,

$$\frac{H_{0,\text{est}}}{H_{0,\text{true}}} = \chi_\sigma \chi_T(T_{\text{ew}}) \chi_{\text{spec-ew}}. \quad (5.21)$$

In our analytic model discussed in §5.3, the inhomogeneity bias, χ_σ , the non-isothermality bias, $\chi_T(T_{\text{ew}})$, and the temperature bias $\chi_{\text{spec-ew}}$ are given by equations (5.9), (5.18), and (5.19), respectively.

While the above model prediction is fairly general, the net value of f_H sensitively depends on the degree of the inhomogeneity and multi-phase temperature structure of real ICM. Our simulated cluster sample implies that $\chi_\sigma \approx (1.1-1.3)$, $\chi_T(T_{\text{ew}}) \approx (0.8-1)$, $\chi_{\text{spec-ew}} \approx (0.8-0.9)$, and therefore $\langle f_H \rangle \approx (0.8-0.9)$. Given the result of Reese et al. (2002), this is certainly indicative, but may need to be interpreted with caution because the result is critically dependent on the reliability of the adopted numerically simulated clusters as representative samples of clusters observed in the real universe. Exactly for this reason, we attempt more direct comparison of our model prediction against observed cluster samples in the next chapter.

Chapter 6

Reconstructing 2D fluctuations from 2D observation

6.1 Complex Structure in X-ray Clusters

Recent observations of galaxy clusters have revealed a rich variety of structural complexity. Recent X-ray satellites with their improved angular resolution, collecting area, and simultaneous spectral measurement capabilities have unveiled complex temperature structure (e.g., Markevitch et al., 2000; Furusho et al., 2001), shock fronts (e.g., Jones et al., 2002), cold fronts (e.g., Markevitch et al., 2000), and X-ray holes (e.g., Fabian et al., 2002). Both X-ray and lensing observations of galaxy clusters reveal that clusters are frequently undergoing mergers (e.g., Briel et al., 2004). With such various and sundry structural complexities may galaxy clusters reliably be used as cosmological probes ?

The complex structure seen in galaxy clusters motivates our investigation of the ICM inhomogeneity. In this thesis, however, we have taken a statistical approach to modeling the inhomogeneity rather than directly modeling such complex phenomena as shocks, cold fronts, etc. Motivated by results from the cosmological hydrodynamic simulations, we have proposed the lognormal model of inhomogeneity in the ICM in chapter 3. Using the lognormal model, we have found that local inhomogeneities of the ICM play an essential role in producing the systematic bias between spectroscopic and emission weighted temperatures (§4) and the Hubble constant measurement (§5). Throughout the previous chapters, the lognormal model has been motivated by and applied only to clusters from cosmological hydrodynamic simulations. Therefore it is crucial to see if inhomogeneities in real galaxy clusters also show the lognormal signature. In reality, this is not a straightforward task since one can observe clusters in X-rays only through their projection over the line of sight. Thus we develop a method of extracting statistical information of the three-dimensional properties of fluctuations from the two-dimensional X-ray surface brightness.

In this chapter, we compare the lognormal model of the ICM directly with X-ray observation of the cluster. We develop a method of extracting statistical information of the three-dimensional properties of fluctuations from the two-dimensional X-ray surface brightness. First we use idealistic synthetic clusters to examine the projection effect, and then apply the method to a real cluster,

Abell 3667. Finally, we perform the similar analysis to simulated clusters from the cosmological hydrodynamic simulation.

6.2 Synthetic Clusters

Cosmological hydrodynamic simulations provide a useful test-bed for exploring cluster structure. Simulated clusters exhibit complex density and temperature structure akin to that of real galaxy clusters. The resolution of our current simulations, however, is limited, especially when compared to the resolution available from current generation X-ray satellites. The (maximum) resolution of the SPH simulations described in §3.2, is $d_{\text{grid}}/r_c \approx 0.1$ assuming $r_c \sim 100$ kpc. This is about one order of magnitude worse than that of the observational data we analyze (§6.3). In addition, we need to systematically survey the parameter space of $\sigma_{\text{LN},n}$ and α_n in order to relate the X-ray surface brightness fluctuations to the density fluctuations. Thus we create a set of synthetic clusters at higher resolution that have lognormal fluctuations around their mean profile. Analysis of mock observations of these synthetic clusters enables us to investigate the relation between the X-ray surface brightness and the statistical properties of the three-dimensional density fluctuations, namely $\sigma_{\text{LN},n}$ and α_n .

To construct the two-dimensional surface brightness profile from the three-dimensional density and temperature distribution, we also need the properties of the power spectra of the underlying density and temperature fluctuations. We adopt statistically isotropic fluctuations with a power-law type power spectrum for both the density fluctuations $P_n(k) \propto k^{\alpha_n}$ and the temperature fluctuations $P_T(k) \propto k^{\alpha_T}$. These assumptions are based on the results of the cosmological hydrodynamic simulations described in §3.4.

6.2.1 Method

The three-dimensional synthetic clusters are projected to obtain two dimensional X-ray surface brightness. In order to incorporate a power-law type power spectrum of spatial fluctuations into the synthetic clusters, we follow a similar methodology as that of several studies of the projection of the interstellar medium (Elmegreen, 2002; Fischera & Dopita, 2004). First a Gaussian random field with a power-law power spectrum is constructed and that field is mapped into a lognormal field. Therefore, our assumption for the power spectrum is adopted for the Gaussian field q as opposed to δ_n . However, we will verify that the ensemble average of the power spectra of q and δ_n ($\mathcal{P}_q(k) \propto k^{\alpha_q}$ and $\mathcal{P}_n(k) \propto k^{\alpha_n}$) have almost the same power-law indices, $\alpha_q \sim \alpha_n$.

We generate the lognormal density fluctuation field as follows. We first generate the real random fields, $a(\mathbf{k})$ and $b(\mathbf{k})$, in k -space, whose distribution functions obey

$$p(a)da = \frac{1}{\sqrt{\pi f(k)}} \exp\left[-\frac{a^2}{f(k)}\right] da, \quad p(b)db = \frac{1}{\sqrt{\pi f(k)}} \exp\left[-\frac{b^2}{f(k)}\right] db, \quad (6.1)$$

where $f(k) \equiv Ak^{\alpha_q}$. Then we compute $q(\mathbf{r})$, the Fourier transform of a complex field $\tilde{q}(\mathbf{k}) \equiv a(\mathbf{k}) + ib(\mathbf{k})$. With the additional conditions $a(\mathbf{k}) = a(-\mathbf{k})$ and $b(\mathbf{k}) = -b(-\mathbf{k})$, $q(\mathbf{r})$ becomes a real Gaussian random field, and its power spectrum, $\mathcal{P}_q(k)$, is equal to the input function

$f(k) \equiv Ak^{\alpha_q}$. The amplitude A is related to the variance of the Gaussian random field:

$$\sigma_g^2 \equiv 4\pi \int_{k_{\min}}^{k_{\max}} k^2 f(k) dk, \quad (6.2)$$

where k_{\min} and k_{\max} denote the minimum and maximum value of the wavenumber. Finally the lognormal deviate, $\delta_x(\mathbf{r})$, is obtained from the Gaussian deviate, $q(\mathbf{r})$, using the relation

$$\delta_x(\mathbf{r}) = \exp\left(\frac{\sigma_{\text{LN},x}}{\sigma_g} q(\mathbf{r}) - \frac{\sigma_{\text{LN},x}^2}{2}\right), \quad (6.3)$$

where $\sigma_{\text{LN},x}$ is the standard deviation of the lognormal field.

We construct synthetic clusters with average density given by the β model (Eq. [2.16]) and δ_n drawn from a lognormal distribution taking into account the power-law type power spectrum of spatial fluctuations. For simplicity, we first adopt a fiducial value of $\beta = 2/3$, and assume isothermality for the synthetic clusters. Later, we examine the effects of varying β and of temperature structure using the polytropic temperature profile (§ 6.2.3).

The density at an arbitrary point is given by

$$n(\mathbf{r}) = \delta_n \bar{n}(r). \quad (6.4)$$

The X-ray surface brightness profile is obtained by projecting the three-dimensional synthetic cluster down to two dimensions. For the isothermal case the projected X-ray surface brightness profile is

$$S_x(\mathbf{R}) \propto \int [n(\mathbf{r})]^2 dl, \quad (6.5)$$

where \mathbf{R} indicates the position on the projected plane and l is the projection of \mathbf{r} onto the line of sight direction.

Performing the procedure described above, we set up a cubic mesh of $n(\mathbf{r})$ in which our three-dimensional synthetic cluster is located with $N_{\text{grid}} = 512$ grid points along each axis. We choose the box size $L_{\text{box}} = 10 r_c$, which results in the distance between two adjacent grid points being $d_{\text{grid}} = 10 r_c / N_{\text{grid}} \sim 0.02 r_c$.

We fit the power spectrum of the δ_n field by a power-law spectrum so that $\mathcal{P}_n(\mathbf{k}) \propto k^{\alpha_n}$. We also fit the power spectrum of the square density field, $\delta_{nn} \equiv n^2 / \langle n^2 \rangle = \delta_n^2 \exp(-\sigma_{\text{LN},n}^2)$ (Appendix A.3), by the power-law $\mathcal{P}_{nn}(k) \propto k^{\alpha_{nn}}$, relevant to X-ray surface brightness since $S_x \propto \int dl \Lambda(T) n^2$. Throughout this chapter, the notation $\langle x \rangle$ is used to denote the ensemble average of quantity x over many clusters.

Figure 6.1 shows the fractional difference of the power-law spectral index of the density (α_n) and density squared fields (α_{nn}) compared to that of the Gaussian field (α_q). The change in the power-law index for the density and density squared distributions compared to the initial Gaussian field are small ($< 3\%$ and $< 13\%$, respectively), and therefore, $\alpha_q \sim \alpha_n \sim \alpha_{nn}$, consistent with the results of Fischera & Dopita (2004).

To quantify the relationship between the inhomogeneity of the density and the X-ray surface brightness, S_x , we introduce the X-ray surface brightness fluctuation from the average radial surface brightness profile $\bar{S}_X(R)$

$$\delta_{S_x}(\mathbf{R}) \equiv \frac{S_x(\mathbf{R})}{\bar{S}_X(R)}, \quad (6.6)$$

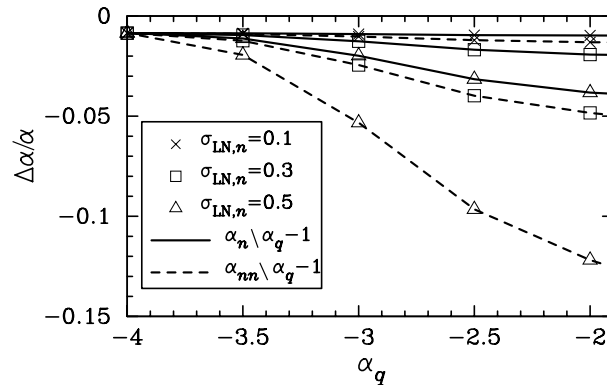


Figure 6.1: The fractional difference of the power-law spectral index of the density (α_n) and density squared fields (α_{nn}) compared to that of the Gaussian field (α_q). Solid and dashed lines indicate $\alpha_n/\alpha_q - 1$ (density) and $\alpha_{nn}/\alpha_q - 1$ (density squared), respectively. Each symbol indicates a different value of $\sigma_{\text{LN},n}$ (cross, square, and triangle correspond to $\sigma_{\text{LN},n} = 0.1, 0.3$, and 0.5 , respectively.) The power-law index of the density field is very close ($\lesssim 3\%$) to that of the Gaussian field used to generate the lognormal distribution and that of the square of the density is within $\sim 13\%$ for larger values of $\sigma_{\text{LN},n}$ and $\lesssim 5\%$ for smaller values ($\sigma_{\text{LN},n} \lesssim 0.3$).

where $R \equiv |\mathbf{R}|$. We define the average profile $\bar{S}_X(R)$ for an individual cluster by fitting the projected synthetic clusters to an isothermal β model

$$\bar{S}_X(R) = S_{X,0} \left[1 + \left(\frac{R}{r_{c,\text{fit}}} \right)^2 \right]^{-3\beta_{\text{fit}}+1/2}, \quad (6.7)$$

where $S_{X,0}$ is the central X-ray surface brightness, $r_{c,\text{fit}}$ is the core radius, and β_{fit} specifies the power-law index for the X-ray surface brightness distribution. These three parameters are derived from a model fit to each synthetic cluster. It is important to emphasize that the average in equation (6.7) is defined for *an individual cluster*. We note that even if we adopt directly the average X-ray surface brightness profile instead of a β model fit (Eq. [6.7]), the results are essentially the same. This is because the radial profile is well approximated by the β model for the synthetic clusters. However, for observations of real galaxy clusters, the β model approximation might break down and one should instead use an average of $S_x(\mathbf{R})$ directly in such cases. In §6.2.2, we will investigate the relation between the standard deviation of the X-ray surface brightness fluctuations, σ_{LN,S_x} , and that of the intrinsic density fluctuations, $\sigma_{\text{LN},n}$.

Here, we consider the relation of σ_{LN,S_x} and $\sigma_{\text{LN},n}$ for the *ensemble average* of clusters assuming that they all obey the β model with the same β , r_c , α_q and $\sigma_{\text{LN},n}$:

$$\langle S_X \rangle(R) \equiv \langle S_x(|\mathbf{R}|) \rangle, \quad (6.8)$$

$$\langle S_x(\mathbf{R}) \rangle \propto e^{\sigma_{\text{LN},n}^2} \int \bar{n}^2 dl, \quad (6.9)$$

where the exponential term of the right hand side of equation (6.9) comes from the second moment of the lognormal distribution (Eq. [A.7] in Appendix A). Although the ensemble average is

not an observable quantity, we can describe an analytical prediction of $\sigma_{\text{LN},S_x}(R)$ assuming the isothermal β model (Appendix D). In addition, one expects that $\overline{S_x} \sim \langle S_x \rangle$ if there is a large enough volume of the cluster compared with the size of fluctuations when calculating $\overline{S_x}$. In other words, the spatial average approaches the ensemble average. For these reasons, it is useful to consider the ensemble average. Using equations (6.8) and (6.9), we define the ensemble average of fluctuations in the X-ray surface brightness as

$$\delta_{S_x,\text{ens}}(\mathbf{R}) \equiv \frac{S_x(\mathbf{R})}{\langle S_x \rangle(R)}. \quad (6.10)$$

We note that the distribution of the square of density fluctuations, which is proportional to the local emissivity in the isothermal case, is also distributed according to the lognormal function with a lognormal standard deviation of $2\sigma_{\text{LN},n}$ if the density fluctuations follow the lognormal distribution with standard deviation $\sigma_{\text{LN},n}$ (Appendix A.3).

6.2.2 Statistical Analysis of the Synthetic Clusters

Here, we investigate the distribution of δ_{S_x} of the synthetic clusters and relate the observable quantities, σ_{LN,S_x} and α_{S_x} , to the underlying, $\sigma_{\text{LN},n}$ and α_n .

We examine the distribution of δ_{S_x} as a function of radial distance R from the cluster center. We first divide the δ_{S_x} field into shells of thickness $0.5r_c$. The distributions of δ_{S_x} within each shell, $p(\delta_{S_x}; R)$, averaged over 256 synthetic clusters are shown in Figure 6.2 for various values of α_q . We find that δ_{S_x} also approximately follows the lognormal distribution. The standard deviation of the logarithm of δ_{S_x} versus radius, $\sigma_{\text{LN},S_x}(R)$, constructed from the averaged shells is displayed in Figure 6.3. Two values of $\sigma_{\text{LN},n}$ are plotted, 0.1 (red) and 0.5 (black), in addition to using the average profile defined by both the β model (Eq. [6.7]; solid) and that for the ensemble (Eq. [6.9]; dotted). The analytic prediction (Eq. [D.13]; dashed) and the case including the temperature structure (§6.2.3; dot-dashed) are also plotted. At large R , $\sigma_{\text{LN},S_x,\text{ens}}(R)$ is approximately $\sigma_{\text{LN},S_x}(R)$ because the spatial average approaches the ensemble average due to the large volume used for averaging. However, the agreement is poor near the center, where the ensemble average is not a good approximation. Although only one value for α_q is shown, similar results are obtained for other values.

Figures 6.2 and 6.3 indicate that the probability density function is weakly dependent on the projected radius R . This radial dependence mainly comes from two competing effects. Consider first the case where the typical nonlinear scale of fluctuations is much smaller than the size of the cluster itself (shallow spectrum). As equation (A1) indicates, the surface brightness at R is given by

$$S_x(R) \propto \int \delta_{nn} \left[1 + \left(\frac{l^2}{r_c^2 + R^2} \right) \right]^{-3\beta} dl. \quad (6.11)$$

This implies that the mean value of $S_x(R)$ is effectively determined by the integration over the line of sight weighted towards the cluster center, roughly between $-\sqrt{r_c^2 + R^2}$ and $+\sqrt{r_c^2 + R^2}$. This is also true for the variance of $S_x(R)$. Since the effective number of independent cells contributing to the variance of $S_x(R)$ is smaller at smaller projected radii, σ_{LN,S_x} slightly increases for smaller R . This explains the behavior of the shallow spectra results for $\alpha_q = -2$ and -2.5 in Figure 6.2.

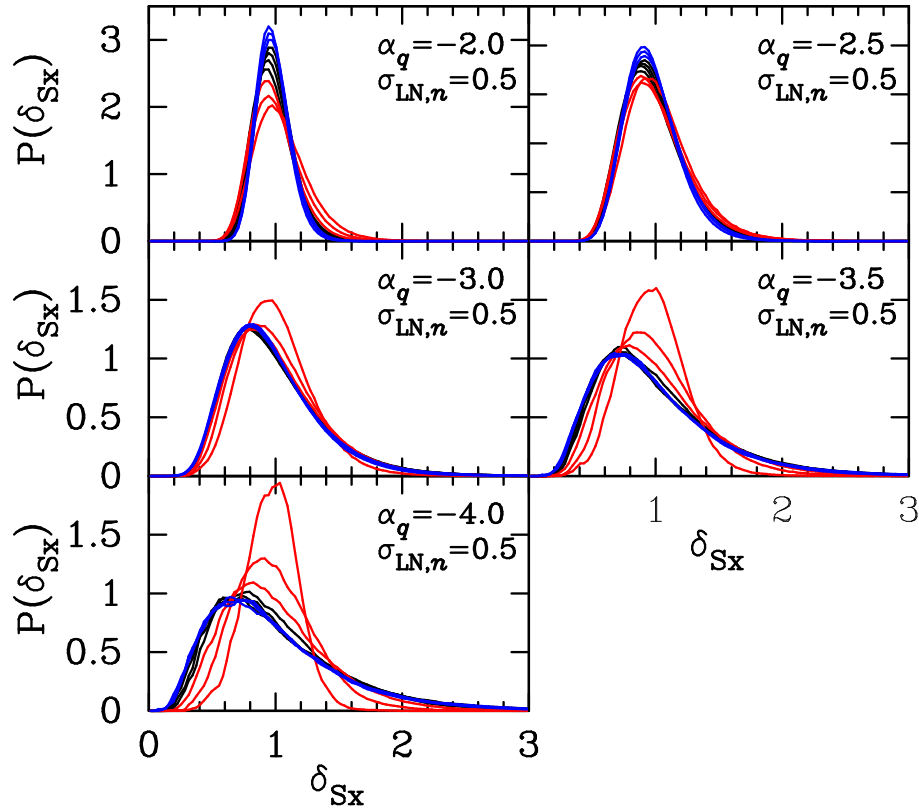


Figure 6.2: The probability distribution of the ensemble-averaged distribution of δ_{Sx} illustrating the radial dependence. The distributions in shells of thickness $0.5r_c$ are shown. Each color indicates a different radial interval: $R < 1.5r_c$ (red), $1.5r_c < R < 3.5r_c$ (black), and $R > 3.5r_c$ (blue).

On the contrary, if the typical nonlinear scale of fluctuations is comparable to or even larger than the cluster size (steep spectrum), the sampling at the central region significantly underestimates the real variance. So the $\sigma_{LN,Sx}$ should increase toward the outer region. This is seen in Figure 6.2 for the steeper spectra, $\alpha_q = -3.5$ and -4 .

Note the first effect is very small and the second effect becomes significant only when $\alpha_q < -3$. The cosmological hydrodynamic simulations imply that the typical value of α_q is -3 . Therefore we neglect the radial dependence of the δ_{Sx} field in the following analysis.

From actual observations, we obtain the δ_{Sx} map for an individual cluster, not the ensemble average. Therefore, we evaluate the distributions of δ_{Sx} in individual synthetic clusters. Figure 6.5 shows the PDF for five individual synthetic clusters (solid) along with the best-fit lognormal distributions (dashed). We neglect the radial dependence and use the distribution for the whole cluster within a diameter of $L_{\text{box}} = 10r_c$. Each color represents a different individual synthetic cluster and each panel shows a different value of the power-law index of the Gaussian field, α_q , with values between -2 and -4 . Even if the analysis is done for one cluster, the distribution approximately follows the lognormal distribution.

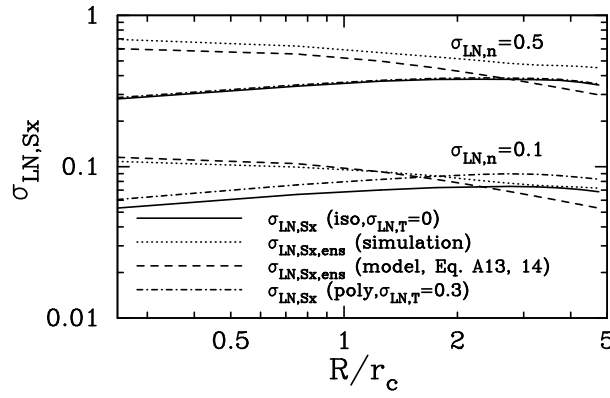


Figure 6.3: The radial dependence of the standard deviations of the logarithm of X-ray surface brightness, $\sigma_{\text{LN},\text{Sx}}$. Two values of $\sigma_{\text{LN},n}$ are plotted, 0.1 and 0.5, as indicated in the figure. Solid and dotted lines show $\sigma_{\text{LN},\text{Sx}}(R)$ calculated using the average profile defined by the β model (Eq. [6.7]) and the ensemble average (Eq. [6.9]), respectively. Dashed lines show the analytical prediction (Eq. [D.13]). Dash-dotted lines indicate the case including the temperature structure. Although we show results only for a single power-law index, $\alpha_q = -3.0$, similar results are obtained in other cases.

The noisy behavior for steeper spectra ($\alpha_q = -3.5, -4$) in Figure 6.5 is due to the presence of fluctuations on scales larger than that of the cluster, similar to the discussion above for Figure 6.2. In other words, steeper spectra ($\alpha_q < -3$) have relatively more larger scale fluctuations compared to shallower spectra ($\alpha_q > -3$). Cosmological hydrodynamic simulations suggest that $\alpha_q \approx 3$, placing galaxy clusters in the less noisy regime. We do not consider the noisy regime further.

The standard deviations of the logarithm of δ_{Sx} , $\sigma_{\text{LN},\text{Sx}}$, for the different sets of α_q (symbols) and $\sigma_{\text{LN},n}$ (colors) are shown in Figure 6.4. The relation between $\sigma_{\text{LN},n}$ and $\sigma_{\text{LN},\text{Sx}}$ is approximately linear (right panel) although the proportionality coefficient depends on α_q . Therefore, we can write

$$\sigma_{\text{LN},\text{Sx}} = Q(\alpha_q)\sigma_{\text{LN},n}. \quad (6.12)$$

We find that $Q(\alpha_q)$ can be approximated well by the following function

$$Q(\alpha_q) = \frac{c_1}{c_2 + |\alpha_q|^{-4}}. \quad (6.13)$$

We calculate the average of $\sigma_{\text{LN},\text{Sx}}/\sigma_{\text{LN},n}$ for each α_q over three different values of $\sigma_{\text{LN},n}$ ($\sigma_{\text{LN},n} = 0.1, 0.3$, and 0.5). By fitting $\sigma_{\text{LN},\text{Sx}}/\sigma_{\text{LN},n}(\alpha_q)$ using equation (6.13), we obtain $c_1 = 2.05 \times 10^{-2}$ and $c_2 = 1.53 \times 10^{-2}$.

Because $\sigma_{\text{LN},\text{Sx}}$ is strongly dependent on the power-law index α_q , the estimate of α_q from the δ_{Sx} map is crucial for interpreting the value of $\sigma_{\text{LN},\text{Sx}}$. Because α_q is an unobservable quantity, we investigate the relationship between the power spectra of δ_n and δ_{Sx} by fitting the power spectrum of δ_{Sx} under the assumptions of both statistical isotropy and a power law so that $\mathcal{P}_{\text{Sx}}(\mathbf{K}) \propto K^{\alpha_{\text{Sx}}}$, where \mathbf{K} indicates the two-dimensional wave vector.

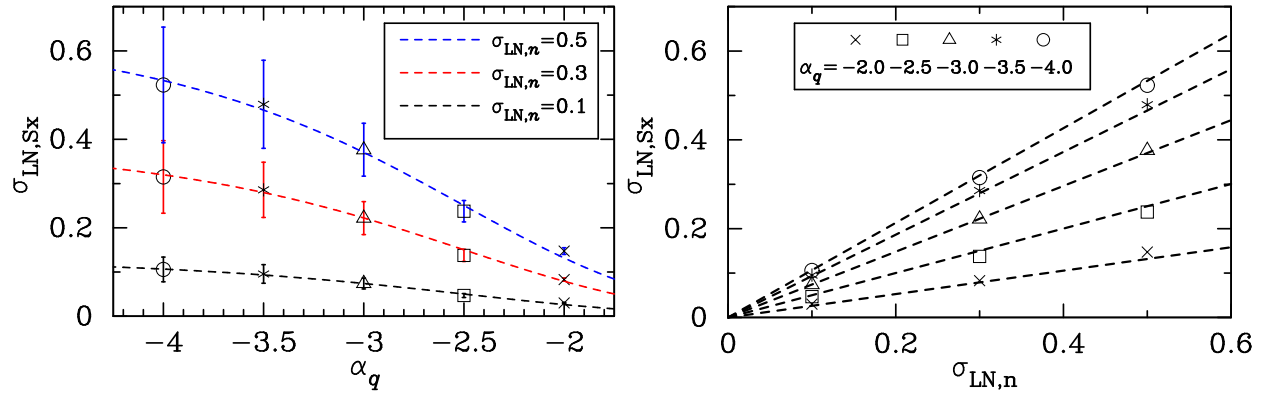


Figure 6.4: The average of σ_{LN,S_x} from the 256 synthetic cluster sample as functions of α_q (left) and $\sigma_{\text{LN},n}$ (right). The left panel also shows the standard deviation of σ_{LN,S_x} from the 256 synthetic clusters and black, red, and blue represent different values of $\sigma_{\text{LN},n}$, 0.1, 0.3, and 0.5, respectively. In both panels, symbols indicate values of α_q (cross, square, triangle, asterisk, and circle correspond to $\alpha_q = -2, -2.5, -3, -3.5,$ and -4 , respectively). Dashed lines show the best-fit approximately linear σ_{LN,S_x} - $\sigma_{\text{LN},n}$ relation (Eq. [6.12] and Eq. [6.13]) for each pair of $\sigma_{\text{LN},n}, \alpha_q$.

Figure 6.6 shows the power-law index of the X-ray surface brightness, α_{S_x} , as a function of its counterpart Gaussian field, α_q . Averages and standard deviations over 256 synthetic clusters are shown for three values of the standard deviation of the logarithm of density, $\sigma_{\text{LN},n}$, where crosses, squares, and triangles correspond to $\sigma_{\text{LN},n}$ of 0.1, 0.3, and 0.5, respectively. The dotted line corresponds to the relation $\alpha_{S_x} = \alpha_q$ and the solid line shows $\alpha_{S_x} = \alpha_q + 0.2$. We find that $\alpha_{S_x} \approx \alpha_q + 0.2$ and since $\alpha_q \approx \alpha_n$, this implies $\alpha_{S_x} \approx \alpha_n + 0.2$. This can be understood as follows. As we have seen in § 6.2.1, the difference between α_n and α_{nn} is relatively small ($\lesssim 13\%$ and often $\lesssim 5\%$). If one assumes δ_{S_x} is the projection of δ_{nn} (although this is only strictly true if the average of the surface brightness is defined by the ensemble average as Eq.[6.8]), δ_{S_x} can be described as

$$\delta_{S_x}(\Theta) = \int dl \delta_{nn} W(\Theta, l), \quad (6.14)$$

where Θ indicates celestial coordinates and $W(\Theta, l)$ is the window function. If we neglect the Θ -dependence of the window function and set $W(\Theta, l) = W(l)$, then $\mathcal{P}_{S_x}(\mathbf{K})$ can be written as

$$\mathcal{P}_{S_x}(\mathbf{K}) = \frac{1}{2\pi} \int dk_l \mathcal{P}_{nn}(\mathbf{k}) |\widetilde{W}(k_l)|^2, \quad (6.15)$$

where $\widetilde{W}(k_l)$ is the Fourier transform of $W(l)$. The assumption that the size of the cluster is much larger than the typical scales of the fluctuations yields $|\widetilde{W}(k_l)|^2 \sim 2\pi\delta(k_l)$, where $\delta(k_l)$ is the Dirac delta function, and therefore $K^{\alpha_{S_x}} \propto k^{\alpha_{nn}}$. Thus, we find $\alpha_n \sim \alpha_{nn} \sim \alpha_{S_x}$ ($\sim \alpha_q$).

In this section, we have found that, in principle, one can estimate the value of $\sigma_{\text{LN},n}$ from analysis of X-ray observations. From the observations one measures σ_{LN,S_x} and α_{S_x} and uses them to infer $\sigma_{\text{LN},n}$ using an empirical relation of $\alpha_q = \alpha_{S_x} - 0.2$. Therefore, one can estimate

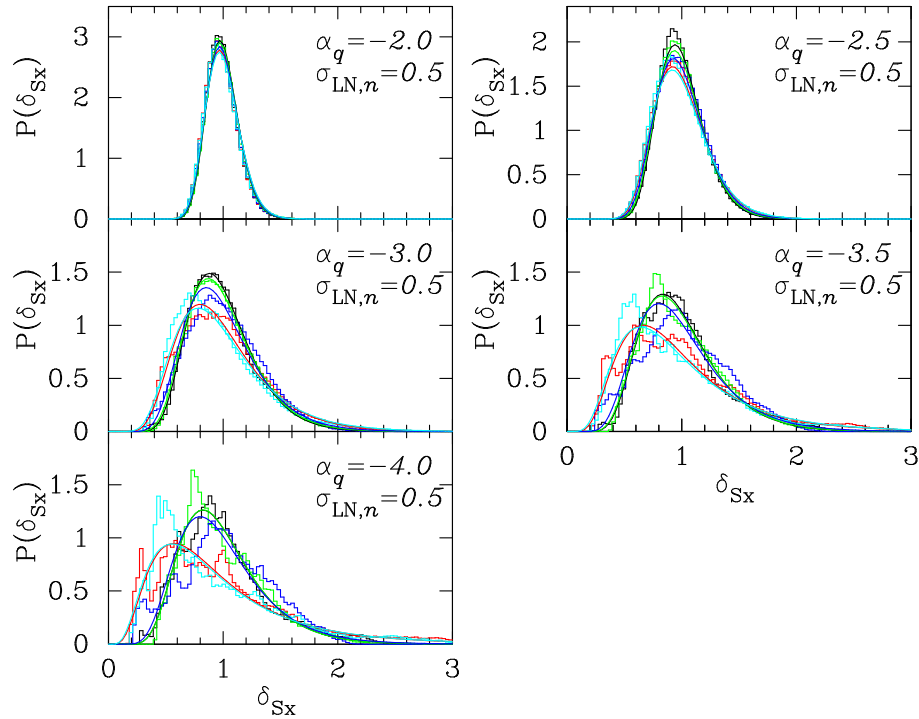


Figure 6.5: The probability distribution of δ_{Sx} for five individual synthetic clusters (solid) along with the best-fit lognormal distributions (dashed). Each color shows a different individual synthetic cluster. Each panel shows a different value of the power law index of the Gaussian field, α_q , between -2 and -4 as indicated in each panel.

the statistical nature of the intrinsic three dimensional fluctuations from two dimensional X-ray observations.

6.2.3 Potential Systematics

Using mock observations of isothermal β models we found a relation between the intrinsic inhomogeneity of the three dimensional cluster gas and the fluctuations in the X-ray surface brightness. We turn our attention to the effects of departures from this idealized model.

In the above description, we have fiducially assumed the β model with $\beta = 2/3$. We investigate two other cases, $\beta = 0.5$, and $\beta = 1.0$, in Figure 6.7, where we show $\sigma_{LN,Sx}$ as a function of α_q for different cases of β (colors). The corresponding fits using equation (6.12) are also shown. Although $\sigma_{LN,Sx}$ tends to increase as β , the change is relatively small ($< 10\%$).

In the above discussion, we assumed isothermality for the ICM. However, the X-ray surface brightness also depends on the underlying cluster temperature structure, including a non-isothermal average temperature profile and local inhomogeneity. We investigate these effects for the X-ray surface brightness distribution.

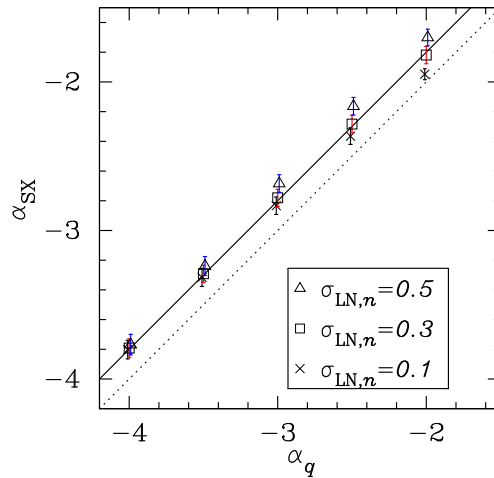


Figure 6.6: Comparison of the X-ray surface brightness (α_{SX}) and the input Gaussian field (α_q) power-law indices. Symbols and error bars indicate the average and the standard deviation, respectively, of α_{SX} for 256 samples for different sets of α_q and $\sigma_{\text{LN},n}$. Symbols correspond to different values of $\sigma_{\text{LN},n}$, with cross, square, and triangle symbols indicating $\sigma_{\text{LN},n} = 0.1, 0.3$, and 0.5 , respectively, and the relations $\alpha_{\text{SX}} = \alpha_q$ and $\alpha_{\text{SX}} = \alpha_q + 0.2$ are also shown (dotted and solid lines, respectively). We obtain α_{SX} for each individual synthetic cluster by fitting $\mathcal{P}_{\text{SX}}(\mathbf{K})$ of an individual cluster under the assumption of both statistical isotropy and a power-law ($\propto K^{\alpha_{\text{SX}}}$).

We assume a polytropic profile for the temperature radial distribution expressed as

$$\bar{T}(r) = T_0 \left(\frac{\bar{n}(r)}{n_0} \right)^{\gamma-1}, \quad (6.16)$$

with polytropic index $\gamma = 1.2$ and $T_0 = 6$ keV, which is the typical set of values in simulated clusters (§3). The ensemble average of the power spectrum of δ_T is assumed to have a power-law form ($\langle \mathcal{P}_T(k) \rangle \sim \mathcal{P}_q(k) \propto k^{\alpha_{q,T}}$). Because $\alpha_T \approx \alpha_{q,T}$ for the same reason as described in § 6.2.1 for density fluctuations, we fiducially adopt the power-law index $\alpha_{q,T} = -3$ based on the results of cosmological hydrodynamic simulations (for details see § 3.4).

We create the lognormal distribution δ_T for temperature fluctuations in the same manner as for the density fluctuations described in § 6.2.1. The temperature of an arbitrary point is assigned according to

$$T(\mathbf{r}) = \delta_T(\mathbf{r})\bar{T}(r). \quad (6.17)$$

We adopt $\sigma_{\text{LN},T} = 0.3$, because it is the typical value for simulated clusters (§3.3). In addition, we assume that δ_n and δ_T are distributed independently, following the results of §3. The X-ray surface brightness is given by

$$S_x(\mathbf{R}) \propto \int [n(\mathbf{r})]^2 \Lambda_x[T(\mathbf{r})] dl, \quad (6.18)$$

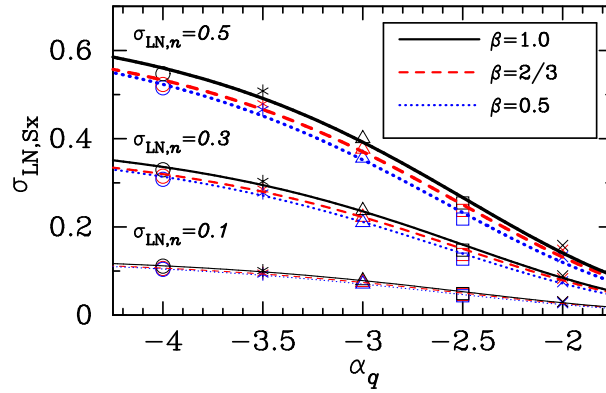


Figure 6.7: The average of σ_{LN,S_x} over the 256 synthetic clusters as a function of α_q for different values of the β model power-law index, β . Symbols correspond to different values of α_q as in Figure 6.4. Each color shows a different value of β (black, red, and blue correspond to $\beta = 1.0, 2/3$, and 0.5 , respectively). Solid, dashed, and dotted lines are fits using equation (6.12), corresponding to $\beta = 1.0, 2/3$, and 0.5 , respectively. The top, middle, and bottom sets of three different lines indicate $\sigma_{\text{LN},n} = 0.5, 0.3$, and 0.1 , respectively, as indicated in the figure.

where $\Lambda_X(T)$ is the X-ray cooling function. We calculate $\Lambda_X(T)$ in the energy range 0.5-10.0 keV using SPEX 2.0 (Kaastra et al., 1996) on the assumption of collisional ionization equilibrium and a constant metallicity of 30% solar abundances.

Examples of the distribution of δ_{S_x} in individual clusters are shown in Figure 6.8 (solid histogram) along with the best fit lognormal distributions (dashed lines). Each color corresponds to a different individual synthetic cluster. Although only one value for the power-law index, $\alpha_q = -3$, is shown, similar results are obtained for other values. The radial dependence of σ_{LN,S_x} including the effects of temperature structure is shown in Figure 6.3 (dot-dashed).

There are only small differences between the isothermal and non-isothermal cases. The X-ray surface brightness is proportional to $n^2\sqrt{T}$ for bremsstrahlung emission. Therefore, the temperature structure effects on δ_{S_x} are much less important than those of the density structure. Hereafter, we neglect the effects of temperature structure and focus only on the effects of density inhomogeneity.

Actual observations by X-ray satellites have finite spatial resolution, characterized by the point spread function (PSF). We assume that the PSF is a circularly symmetric Gaussian with standard deviation σ . The PSF can then be parameterized by a single parameter called the *half power diameter* (θ_{HPD}) in which 50% of the X-rays are enclosed ($\theta_{\text{HPD}}/\sigma = 2\sqrt{2\log 2}$).

We investigate three cases, $\theta_{\text{HPD}}/\theta_c = 0.1, 0.2$ and 0.5 . Figure 6.9 shows the effect of the PSF on σ_{LN,S_x} as a function of radius. In each case, the average over 256 synthetic clusters is shown. Results for no PSF correction ($\theta_{\text{HPD}} = 0$, solid) and $\theta_{\text{HPD}}/\theta_c = 0.1$ (dashed), 0.2 (dot-dashed), and 0.5 (dotted) are shown. As $\theta_{\text{HPD}}/\theta_c$ increases, σ_{LN,S_x} near the center of the cluster decreases. This can be understood as follows. In each radial shell, fluctuations smaller than roughly the radius of the shell predominately contribute to the fluctuations, namely $\sigma_{\text{LN},S_x}(R)$. The PSF effectively smooths out the smaller scale fluctuations (roughly up to the size of the PSF),

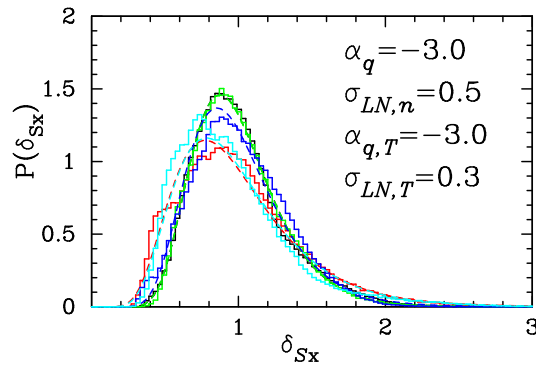


Figure 6.8: The distribution of δ_{Sx} for five individual clusters including the effects of temperature structure. Synthetic clusters (solid histogram) and best-fit lognormal model (dashed lines) are both shown for each cluster. Each color corresponds to a different individual synthetic cluster. Although we display only one example of the power-law index, $\alpha_q = -3.0$, similar results are obtained in other cases as well.

reducing $\sigma_{LN,Sx}$, while preserving the large scale fluctuations. Since the inner shells only contain small scale fluctuations, they are more strongly affected by the PSF. The case of $\theta_{HPD}/\theta_c = 0.5$ best illustrates these effects. The reduction of $\sigma_{LN,Sx}$ from the PSF is seen at all radii. However, it is only a slight reduction at large radii, increasing as the radius decreases, with a very large effect near the cluster center.

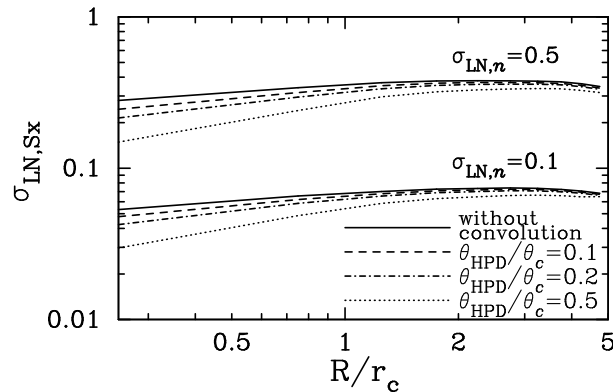


Figure 6.9: The effect of the PSF on $\sigma_{LN,Sx}$ as a function of radius, R/r_c , for the case of $\alpha_q = -3$ and $\beta = 2/3$. Solid curves show $\sigma_{LN,Sx}(R)$ without convolution of the PSF. Dashed, dash-dotted, and dotted curves correspond to $\theta_{HPD}/\theta_c = 0.1, 0.2$ and 0.5 , respectively. Two values of $\sigma_{LN,n}$ are plotted, 0.1 and 0.5 , as indicated in the figure.

In summary, when δ_n in three dimensions follows the lognormal distribution, δ_{Sx} in two dimensions also approximately follows the lognormal distribution. The mean value of $\sigma_{LN,Sx}$ for an individual cluster is strongly dependent on both $\sigma_{LN,n}$ and α_q . Because α_q is approximately equal to α_{Sx} , in principle, one can infer $\sigma_{LN,n}$ from $\sigma_{LN,Sx}$ although there is still some dispersion

even if α_q is known. In addition, the effect of the temperature structure is minimal.

6.3 Application to Abell 3667

Simulations suggest that the lognormal model (Eq. [3.6]) is a reasonable approximation of the small scale structure in galaxy clusters. We compare this model with *Chandra* X-ray observations of the nearby galaxy cluster Abell 3667 at a redshift $z = 0.056$ (Struble & Rood, 1999). A3667 is a well observed nearby bright galaxy cluster that does not exhibit a cool core observed by *Chandra*. With its complex structure, including a cold front (Vikhlinin et al., 2001) and possible merger scenario (e.g., Knopp et al., 1996), A3667 will serve as a difficult test case for the lognormal model of density fluctuations.

Table 6.1: A3667 *Chandra* Observations

obsID	t_{exp} (ks)	RA (h m s)	DEC (d m s)
513	45	20 12 50.30	-56 50 56.99
889	51	20 11 50.00	-56 45 34.00
5751	131	20 13 07.25	-56 53 24.00
5752	61	20 13 07.25	-56 53 24.00
5753	105	20 13 07.25	-56 53 24.00
6292	47	20 13 07.25	-56 53 24.00
6295	50	20 13 07.25	-56 53 24.00
6296	50	20 13 07.25	-56 53 24.00

6.3.1 Data Reduction

Chandra observations of the galaxy cluster A3667 are summarized in Table 6.1. Listed are the observation identification numbers, exposure times, and pointing centers of each of the eight archival *Chandra* observations of A3667 used in this analysis. The data are reduced with CIAO version 4.0 and calibration data base version 3.4.2. The data are processed starting with the level 1 events data, removing cosmic ray afterglows, correcting for charge transfer inefficiency and optical blocking filter contamination, and other standard corrections, in addition to generating a customized bad pixel file. The data are filtered for *ASCA* grades 0, 2, 3, 4, 6 and status=0 events, and the good time interval data provided with the observations are applied. Periods of high background count rate are excised using an iterative procedure involving creating light curves in background regions with 500 s bins, and excising time intervals that are in excess of 4σ from the median background count rate. This sigma clipping procedure is iterated until all remaining data lie within 4σ of the median. The final events list is limited to energies 0.7-7.0 keV to exclude the low and high energy data that are more strongly affected by calibration uncertainties. Finally,

the images are binned by a factor of eight, resulting in a pixel size of $3.94''$ ($1'' = 0.75h^{-1}$ kpc). This pixel size matches the resolution of the synthetic clusters considered in §6.2. In particular, the ratio of pixel size to the cluster core radius of the *Chandra* image is similar to the synthetic cluster grid spacing compared to the synthetic cluster core radius, namely, for $\theta_c \sim 180''$ ($\approx 135h^{-1}$ kpc) (Reiprich & Böhringer, 2002b; Knopp et al., 1996), $\theta_{\text{pix}}/\theta_c \sim d_{\text{grid}}/r_c \sim 0.02$. Exposure maps are constructed for each observation at an energy of 1 keV. The binned images and exposure maps for each observation are then combined to make the single image and exposure map used for the analysis.

A wavelet based source detector is used to find and generate a list of potential point sources. The list is examined by eye, removing bogus or suspect detections, and then used as the basis for our point source mask. Figure 6.10 (left) shows the *Chandra* merged image of A3667, the counts image divided by the exposure map, where the point source mask has been applied. Also shown is the δ_{Sx} image (right), discussed below. A cold front (Vikhlinin et al., 2001) is clearly visible in the south-eastern region of the δ_{Sx} image.

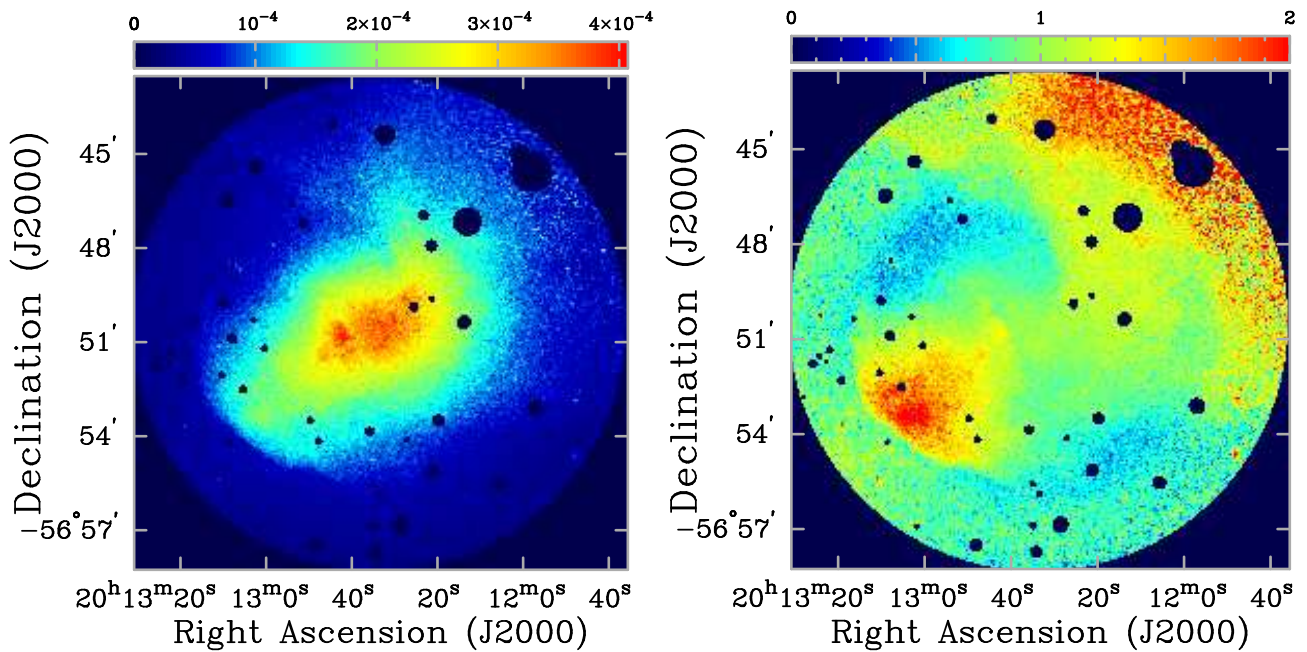


Figure 6.10: *Chandra* image of the galaxy cluster Abell 3667 (left) and the corresponding δ_{Sx} image (right). The counts image has been divided by the exposure map to yield X-ray surface brightness ($\text{cnt s}^{-1} \text{cm}^{-2} \text{arcmin}^{-2}$), including scaling for the pixel size. Point sources in the field have been masked. The size of both panels is approximately $16' \times 16'$ which corresponds to $0.7h^{-1} \text{Mpc} \times 0.7h^{-1} \text{Mpc}$.

6.3.2 Analysis and Results

In order to determine the center of A3667, a β model is fit to the data with fixed core radius ($180''$) and β ($2/3$), using software originally developed for the combined analysis of X-ray and Sunyaev-

Zel'dovich effect observations (Reese et al., 2000, 2002; Bonamente et al., 2006). Because A3667 is nearby and appears very large, *Chandra* observations do not encompass the entire cluster but provide a wealth of information on the complexities inherent in galaxy cluster gas. By using a β model fit to the diffuse emission of the cluster gas we obtain a better measurement of its center than simply using the brightest pixel or other simple estimates, which fail to take into account the complex structure manifest in this cluster. A circular region of radius $\sim 8'$ ($\approx 360h^{-1}$ kpc) centered on A3667 is used in the analysis, corresponding to two and a half times the cluster's core radius, the largest usable region from the arrangement of the combined *Chandra* observations.

The average X-ray surface brightness is required to compute $\delta_{S_x} = S_x/\bar{S}_X$. If one computes the average surface brightness, \bar{S}_X , in annular shells, then one will tend to under (over) estimate \bar{S}_X toward the inner (outer) radius of each annulus. Therefore, this will lead to an over (under) estimate of δ_{S_x} toward the inner (outer) radius of each annulus. To alleviate this systematic, we adopt the azimuthally averaged X-ray surface brightness as the model for \bar{S}_X , and use cubic spline interpolation between radial bins. The X-ray surface brightness radial profile for A3667 is shown in Figure 6.11, along with the interpolated model (line).

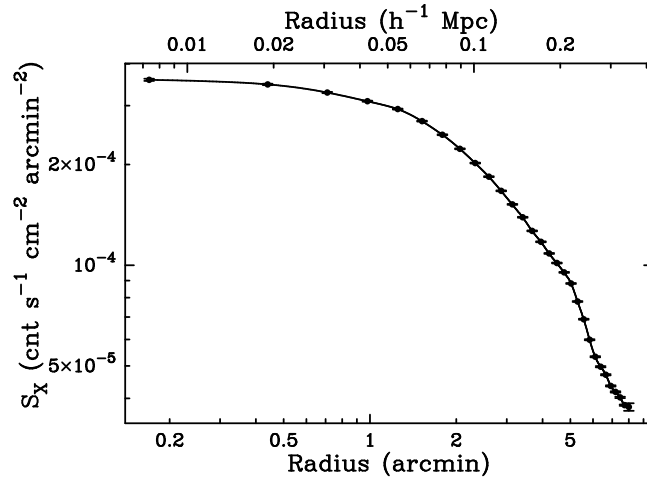


Figure 6.11: *Chandra* radial profile of the galaxy cluster Abell 3667 (points) with the interpolated model (solid line). This model is used as the average X-ray surface brightness distribution in the calculation of δ_{S_x} .

The probability distribution of δ_{S_x} , $p(\delta_{S_x})$, is computed from the histogram of pixels calculated from the δ_{S_x} image and shown in Figure 6.12. The lognormal distribution (Eq. [3.6]) is fit to the $p(\delta_{S_x})$ of A3667, where the only free parameter is the standard deviation of the logarithm of δ_{S_x} , σ_{LN,S_x} . The best fit value for the lognormal model is $\sigma_{LN,S_x} = 0.30$. In addition, a Gaussian distribution and the Gaussian squared distribution (Eq. [A.23]) are also fit to the data, with its parameter, the standard deviation. If density distribution follows a Gaussian, the density squared (the X-ray emissivity on the isothermal assumption) follows the Gaussian squared distribution provided by equation (A.23) in Appendix A.3. Figure 6.12 shows the PDF of δ_{S_x} for the *Chandra* observations of the galaxy cluster A3667 (solid blue histogram). The best fit lognormal (solid red), Gaussian (dashed green), and Gaussian squared (dotted) models are also shown. A Poisson

distribution (dot-dashed magenta) is also shown for comparison, using the average counts per pixel in the fitting region as the parameter for the Poisson distribution. Clearly, what is seen is not the result of Poisson statistics. The lognormal model seems to be a reasonable match to the observed PDF.

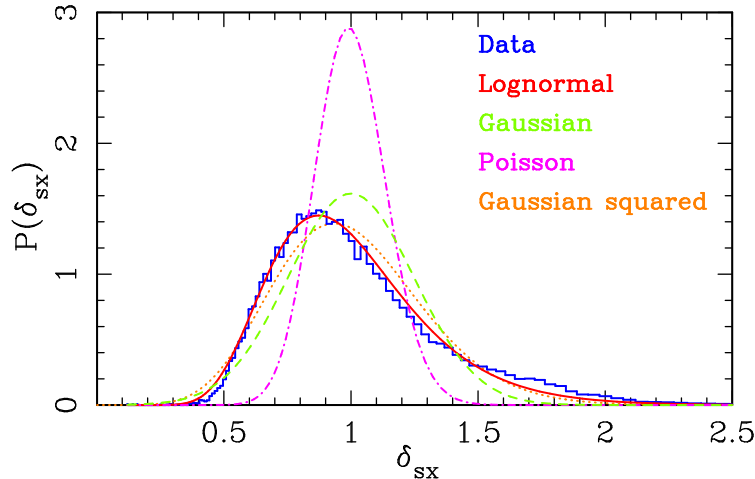


Figure 6.12: Probability distribution of δ_{Sx} from *Chandra* observations of the galaxy cluster Abell 3667 (blue histogram) along with the best fit lognormal distribution (red line) with $\sigma_{LN,Sx} = 0.30$. The lognormal distribution seems to be a reasonable description of the ICM inhomogeneity in A3667. Also shown are the best-fit Gaussian model (dashed green), a Poisson model (dot-dashed magenta) using the average counts per pixel within the fitting region, and the best-fit Gaussian squared model (Eq. [A.23]; dotted line orange).

However, without information on the power spectrum of the δ_{Sx} fluctuations, it is difficult to interpret the value of $\sigma_{LN,Sx}$ (§6.2.2) and relate it to the fluctuations in the density distribution (Eqs. [6.12, 6.13]; Fig. 6.4). Therefore, we take the Fourier transform of the δ_{Sx} image and compute the average power spectrum in wavenumber annuli. The power spectrum of δ_{Sx} fluctuations is shown in Figure 6.13 (thick solid) along with three power-law spectra with spectral indices of -2 (dashed), -3 (dot-dashed), and -4 (dotted) for comparison. The power spectrum of δ_{Sx} has been normalized to one at the largest scales. A simple power-law model fit to the power spectrum yields a spectral index of $\alpha_{Sx} = -2.7$ using the entire spectrum, and a spectral index of $\alpha_{Sx} = -3.0$ if excluding the larger wavenumbers ($\gtrsim 2 \text{ arcmin}^{-1}$), roughly where the power spectrum changes shape.

We also investigate the radial dependence of the δ_{Sx} distribution. As shown in Figure 6.14, the distribution of the inner radius is narrower than the outer one. The distributions of the synthetic clusters have a similar tendency with $\alpha_q = -3$ (Fig. 6.2). Therefore, we conclude that the Poisson noise from the outer region does not significantly affect the distribution.

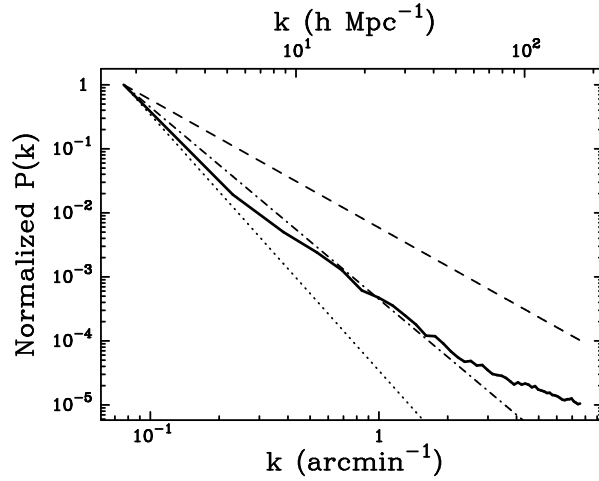


Figure 6.13: Power spectrum of δ_{S_x} (thick solid) from *Chandra* observations of the galaxy cluster Abell 3667, normalized to one at the largest scale. Also plotted are three power-law power spectra with spectral indices of -2 (dashed), -3 (dot-dashed), and -4 (dotted) for comparison.

6.3.3 Implications

Both the standard deviation of the logarithm of X-ray surface brightness fluctuations, $\sigma_{\text{LN}, S_x} = 0.30$, and the power spectrum power-law index $\alpha_{S_x} \approx -3$, fall into the range expected from hydrodynamical galaxy clusters and therefore used in the synthesized cluster analysis (§3.4). By combining these pieces of information, we can relate the information obtained from the X-ray surface brightness distribution to that of the underlying density distribution, using the results of the synthesized cluster analysis. Using the synthetic cluster result that the spectral indices of the X-ray surface brightness fluctuations and that of the Gaussian field are simply related as $\alpha_{S_x} \approx \alpha_q + 0.2$, and the relation between $\sigma_{\text{LN}, n}$, σ_{LN, S_x} , and α_q (Eqs. [6.12, 6.13]; Fig. 6.4), the *Chandra* results of $\sigma_{\text{LN}, S_x} = 0.30$ and $\alpha_{S_x} = -2.7$ imply that the fluctuations in the underlying density distribution have $\sigma_{\text{LN}, n} = 0.43$. A value of $\alpha_{S_x} = -3.0$ implies $\sigma_{\text{LN}, n} = 0.36$. The difficult test case of the A3667 X-ray surface brightness seems to follow the lognormal distribution of density fluctuations, thus enabling an estimate of the statistical properties of the underlying ICM density fluctuations.

Our data of A3667 has sufficient photon counts and is fairly free from the discreteness effect. However, in most clusters, if this is not the case and we need to take account of the Poissonian nature of photon statistics, as shown in Appendix E. We believe that the hybrid distribution described in Appendix E enable us to avoid the discreteness effect and to estimate the true S_x distribution.

6.4 Comparison with the Simulated Clusters

In §6.2, we found that synthetic clusters with lognormal fluctuations show a linear relation between σ_{LN, S_x} and $\sigma_{\text{LN}, n}$. We now return to the simulated clusters described in 3.2 to further

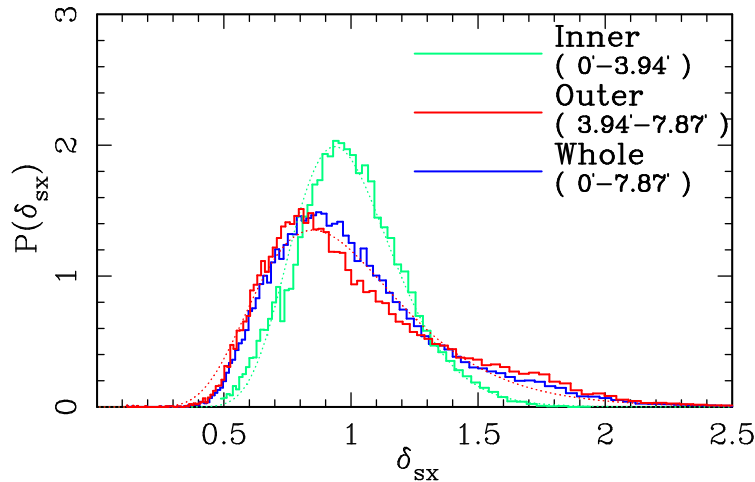


Figure 6.14: The radial dependence of the PDF of δ_{Sx} (histograms). Green and red histograms indicate the distribution within the inner shell ($R = 0' - 3.94'$) and the outer shell ($R = 3.94' - 7.87'$), respectively. Dotted lines are the best-fit lognormal function ($\sigma_{LN,Sx} = 0.21$ for the inner shell and $\sigma_{LN,Sx} = 0.32$ for the outer shell). Blue histogram indicates the distribution of the whole region ($R = 0' - 7.87'$).

explore these results.

For each cluster extracted from the simulations, we create X-ray surface brightness maps towards three orthogonal directions, and compute $\delta_{Sx}(\mathbf{R}) = S_X(\mathbf{R})/\bar{S}_X(R)$ in a similar manner as described for the synthetic clusters in § 6.2.1. The regions we consider are within the projected virial radius R_{200} . The projected virial radius, R_{200} , is the radius within which the mean interior density is 200 times that of the critical density.

Although the lognormal distribution is a good fit to the density (and temperature) of simulated galaxy clusters in three-dimensions, the projection to X-ray surface brightness suffers from the additional complexity of projection effects. If large clumps are present, the distribution of X-ray surface brightness fluctuations, δ_{Sx} , is not well approximated by the lognormal distribution. The large clumps artificially distort the average profile of the cluster and therefore bias the value of δ_{Sx} , which depends on the average profile. We also note that although these clumps fall within the projected virial radius, R_{200} , they usually fall outside of the three dimensional virial radius, r_{200} . We therefore exclude quadrants that contain large clumps, using $\delta_{Sx} > 10$ as the exclusion criterion. Then, we recompute $\bar{S}_X(R)$ and δ_{Sx} . The complex structure of simulated clusters is illustrated in the δ_{Sx} images shown in Figure 6.15, where examples of a simulated cluster both before and after removal of a quadrant are displayed. The circles show the projected virial radius, R_{200} .

In Figure 6.16 the probability distributions of δ_{Sx} for the simulated clusters (histograms) along with the best-fit lognormal model (dotted lines) are displayed. Each color indicates the projection along a different, orthogonal line of sight. Overall, the probability distributions of δ_{Sx} are reasonably well approximated by the lognormal function, consistent with the results from the synthetic clusters (§ 6.2.2).

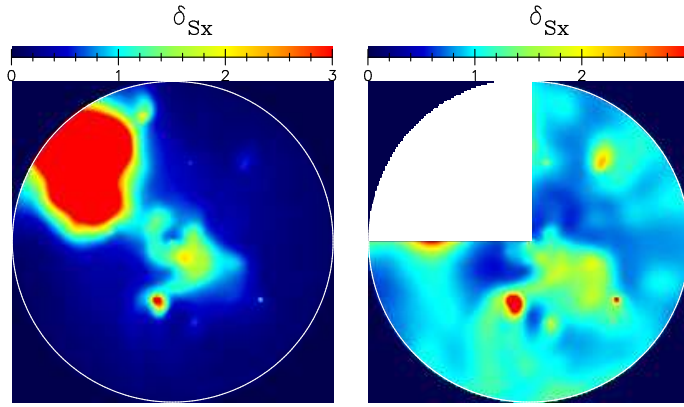


Figure 6.15: An example of a δ_{Sx} map from a cosmological hydrodynamic simulated cluster (“Centaurus”) both before (left) and after (right) removal of a quadrant with a large clump. Circles show the projected virial radius (R_{200}). Although within the projected virial radius, R_{200} , these structures often reside outside of the three-dimensional virial radius, r_{200} .

We now come full circle to compare our results from the synthetic clusters directly to the simulations. In order to do this, we look at the relationship between $\sigma_{LN,n}(\text{sim})$ measured in the simulated clusters and $\sigma_{LN,n}(\text{model})$ predicted from the synthetic cluster results, equations (6.12) and (6.13), where we adopt $\alpha_q = \alpha_{Sx} - 0.2$ (see §6.2.2). The value of α_{Sx} for each simulated cluster is obtained by fitting a power-law model, $\mathcal{P}(K) \propto K^{\alpha_{Sx}}$, to the power spectra of δ_{Sx} . Because the resolution of the simulations is much poorer than that of the synthetic clusters, we must recompute the coefficients c_1 and c_2 in equation 6.13 from a set of lower resolution synthetic clusters. Assuming $r_c \sim 100 h^{-1}$ kpc for the simulated clusters, we choose the resolution $\sim 0.1 d_{\text{grid}}/r_c$, noting that this value corresponds to the *maximum* resolution of the simulations. Performing the same procedure described in §6.2, we obtain $c_1 = 3.99 \times 10^{-2}$ and $c_2 = 3.36 \times 10^{-2}$.

We compare $\sigma_{LN,n}(\text{model})$ and $\sigma_{LN,n}(\text{sim})$ in Figure 6.17. Each color corresponds to a different line of sight. Although there is large scatter, these results indicate that it is possible to estimate $\sigma_{LN,n}$ within a factor of two only using the information obtained from the X-ray surface brightness distribution.

6.5 Summary

In this chapter, we have developed a method of extracting statistical information on the ICM inhomogeneity from X-ray observations of galaxy clusters. With a lognormal model for the fluctuations motivated by cosmological hydrodynamic simulations, we have created synthetic clusters, and have found that their X-ray surface brightness fluctuations retain the lognormal nature. In addition, the result that $\sigma_{LN,Sx}$ and $\sigma_{LN,n}$ are linearly related implies that one can, in principle, estimate the statistical properties of the three dimensional density inhomogeneity ($\sigma_{LN,n}$) from X-ray observations of galaxy clusters ($\sigma_{LN,Sx}$ and α_{Sx}).

We have compared the predictions of our model to *Chandra* X-ray observations of the galaxy cluster A3667. For the first time in a real galaxy cluster we were able to detect the lognormal

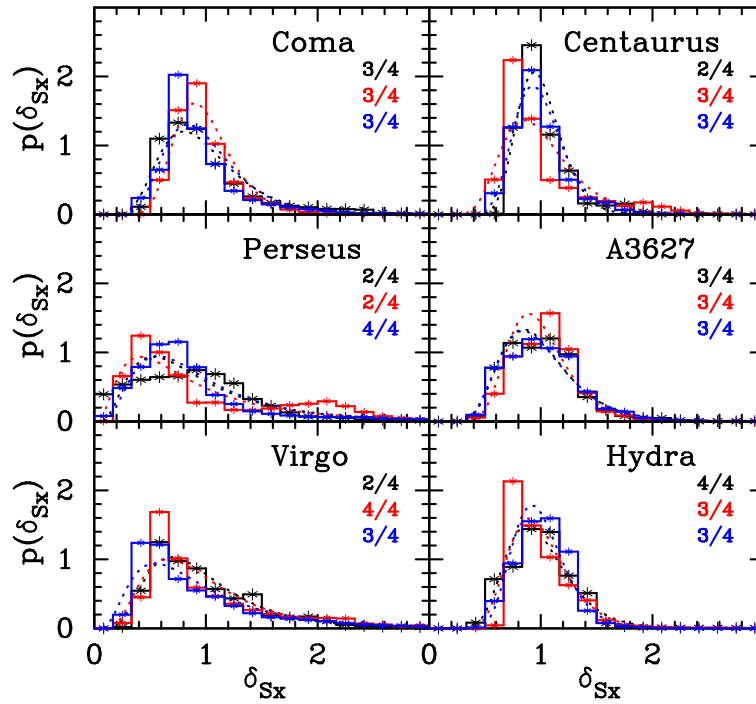


Figure 6.16: The distribution of δ_{Sx} for each of the six clusters from a cosmological hydrodynamic simulation (points and solid histogram). Each color indicates the projection along a different, orthogonal line of sight. For each line of sight, we show the number of quadrants used for the analysis. For example, “3/4” indicates that one quadrant is excluded and three remain. The best fit lognormal model for each projection is also shown (dotted lines).

signature of X-ray surface brightness fluctuations, which was originally motivated by simulations. Based on the synthetic cluster results, this enabled an estimate of the statistical properties of the inhomogeneity of the ICM of A3667. In the context of lognormally distributed inhomogeneity, we obtain $\sigma_{LN,n} \approx 0.4$ for the gas density fluctuations of A3667. It is encouraging that the value of the fluctuation amplitude for Abell 3667 is in reasonable agreement with typical values from the simulated clusters.

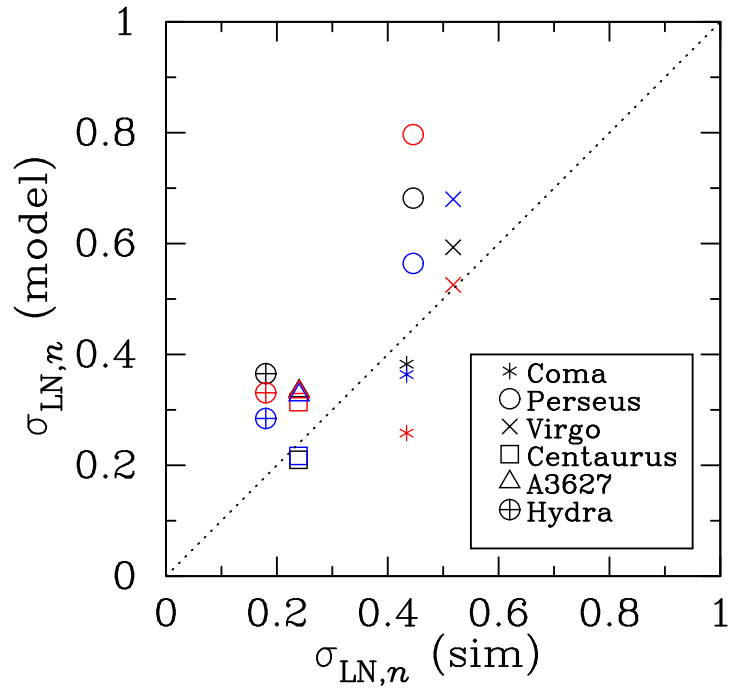


Figure 6.17: The density fluctuation standard deviation predicted by our model, $\sigma_{LN,n}(\text{model}) = \sigma_{LN,Sx}/Q(\alpha_q)$ versus that from the simulations, $\sigma_{LN,n}(\text{sim})$. Symbols show different simulated clusters (see figure legend) and colors indicate different orthogonal lines of sight. Also plotted is the simple linear relation $\sigma_{LN,n}(\text{model}) = \sigma_{LN,n}(\text{sim})$ for comparison.

Chapter 7

Conclusions

In this thesis, we have studied the statistical nature of the inhomogeneity in ICM and its implications for the cosmological applications of the galaxy clusters. Using the cosmological hydrodynamic simulation, we proposed a lognormal PDF for the statistical model of density and temperature fluctuations of ICM. We considered the effect of inhomogeneity to both the cluster temperature estimate and the Hubble constant measurement from the SZE and X-ray. We also confirmed the signature of the lognormal model of the density inhomogeneity from Abell 3667. Our conclusions are summarized as follows.

First of all, we have investigated the inhomogeneity of ICM using the cosmological hydrodynamic simulations. We found that the local inhomogeneities of the gas temperature and density, after corrected for the global radial profiles, have nearly a universal distribution that resembles the lognormal function. On the basis of the lognormal model, we have studied the influence of the ICM inhomogeneities on two important cosmological applications of galaxy clusters, the cluster temperature and the H_0 measurement from the SZE and X-ray.

In chapter 4, we have explored the origin of the bias in the spectroscopic temperature of simulated galaxy clusters discovered by Mazzotta et al. (2004). Using the simulations data, we have constructed mock spectra of clusters, and confirmed their results; the spectroscopic temperature is systematically lower than the emission-weighted temperature by 10-20% and that the spectroscopic-like temperature defined by equation (4.4) approximates the spectroscopic temperature to better than $\sim 6\%$. We have made an analytic description of this bias with the lognormal model. We have exhibited that not only the radial profiles but also the local inhomogeneities are largely responsible for the above mentioned bias of cluster temperatures.

Possible systematic errors of the H_0 measurement have been investigated in chapter 5. In particular we addressed the validity and limitations of the spherical isothermal β model in estimating H_0 , which has been used widely as a reasonable approximation after averaging over a number of clusters. We introduced the ratio of the estimated to the true Hubble constant, f_H , to characterize the systematic errors. We constructed an analytic model for f_H based on the lognormal model and the temperature estimate bias discussed in chapter 4, and identified three important sources for the systematic errors; density and temperature inhomogeneities in the ICM, the temperature profile, and departures from sphericity. While the above model prediction is fairly general, the net value of f_H sensitively depends on the degree of the inhomogeneity

and multi-phase temperature structure of real ICM. Our simulated cluster sample implies that $\chi_\sigma \approx (1.1 - 1.3)$, $\chi_T(T_{\text{ew}}) \approx (0.8 - 1)$, $\chi_{\text{spec-ew}} \approx (0.8 - 0.9)$, and therefore $\langle f_H \rangle \approx (0.8 - 0.9)$. Our results explain the discrepancy between the results of Reese et al. (2002) and that of the other measurements.

Through chapter 4 and chapter 5, we have confirmed that the ICM inhomogeneities have a crucial role in the cosmological applications of the galaxy clusters. Modeling of inhomogeneity in clusters will gain in importance for the future observations of galaxy clusters, including Japanese Astro-H satellite (Kunieda et al., 2004; Mitsuda et al., 2008; Takahashi et al., 2008) and Spektr Röntgen Gamma satellite.

In chapter 6, we have tested the lognormal model against observation. We have developed a method of extracting statistical information on the ICM inhomogeneity from X-ray observations of galaxy clusters. We have created synthetic clusters following the lognormal model, and have found that their X-ray surface brightness fluctuations retain the lognormal nature. In addition, the result that σ_{LN,S_x} and $\sigma_{\text{LN},n}$ are linearly related implies that one can, in principle, estimate the statistical properties of the three dimensional density inhomogeneity ($\sigma_{\text{LN},n}$) from X-ray observations of galaxy clusters (σ_{LN,S_x} and α_{S_x}).

We have compared the predictions of our model to *Chandra* X-ray observations of the galaxy cluster A3667. For the first time in a real galaxy cluster we were successful in detecting the lognormal signature of X-ray surface brightness fluctuations, which was originally motivated by simulations. Based on the synthetic cluster results, this enabled an estimate of the statistical properties of the inhomogeneity of the ICM of A3667. In the context of lognormally distributed inhomogeneity, we obtain $\sigma_{\text{LN},n} \approx 0.4$ for the gas density fluctuations of A3667. It is encouraging that the value of the fluctuation amplitude for Abell 3667 is in reasonable agreement with typical values from the simulated clusters.

Indeed, the lognormal distribution for density fields has been discussed in the context of the cosmological mass distribution (e.g., Coles & Jones, 1991; Kayo et al., 2001; Taruya et al., 2002) and the interstellar medium (e.g., Vázquez-Semadeni, 1994; Padoan et al., 1997; Passot & Vázquez-Semadeni, 1998; Wada & Norman, 2001, 2007). While it is not clear if they share any simple physical principle behind, it is interesting to attempt to look for the possible underlying connection. Although the physical origin of the lognormal model is still unresolved, the observational support for the density inhomogeneity discussed in chapter 6 is encouraging.

In conclusion, the inhomogeneity in the ICM significantly affects on cosmological analysis and interpretation of galaxy clusters. The statistical model we have developed will become a good tool to understand the current and future results of observations.

Acknowledgements

I would like to express my sincere gratitude to my supervisor and a collaborator of this work, Yasushi Suto, who has given me the principle that guides this work and a lot of advice. I am deeply grateful to my collaborators, Shin Sasaki, Tetsu Kitayama, and Erik D. Reese. This work would not have been possible without all of the help and support of them. I am also grateful to Tadayuki Takahashi for his careful reading of the manuscript and helpful suggestions. I would also like to thank the staff of high energy astrophysics group in ISAS/JAXA, in particular, Kazuhisa Mitsuda and Noriko Y. Yamasaki for both giving a lot of advice and knowledge about X-ray astronomy. The discussions with Kohji Yoshikawa, Keisuke Shinozaki, Yoh Takei, and Tomotaka Yoshino helped to deepen my understanding of X-ray astronomy and X-ray satellites. I also thank to my parents for supporting my graduate school life. Finally, I am very grateful to my wife, Yuri Ikegami, for her emotional support.

I gratefully acknowledge support from a Japan Society for Promotion of Science Grant-in-Aid for science fellows.

Appendix A

Nature of the Lognormal Distribution

A.1 Probability Density Function, Expectation and Moment

Let us consider the sample-space for the random variable x . The probability of the occurrence of the event A is denoted by $P(A)$. The distribution function is defined as

$$F(x') \equiv P(A) \tag{A.1}$$
$$A : x \leq x'.$$

Consider the event B

$$B : x_1 \leq x \leq x_2, \tag{A.2}$$

where $x_1 \leq x_2$. The probability of B is described as

$$P(B) = P(x \leq x_2) - P(x \leq x_1) = F(x_2) - F(x_1). \tag{A.3}$$

The probability density function (PDF) is the derivative of $F(x)$,

$$P(x) \equiv \frac{d}{dx}F(x). \tag{A.4}$$

Equation (A.3) can be rewritten as

$$P(B) = F(x_2) - F(x_1) = \int_{x_1}^{x_2} P(x)dx. \tag{A.5}$$

The expectation and the n -th moment of x are defined as

$$\langle x \rangle \equiv \int_{-\infty}^{\infty} xP(x)dx, \tag{A.6}$$

$$\langle x^n \rangle \equiv \int_{-\infty}^{\infty} x^n P(x)dx, \tag{A.7}$$

respectively.

Now, we consider the lognormal PDF:

$$P_{\text{LN}}(x) dx = \begin{cases} \frac{1}{\sqrt{2\pi}\sigma_{\text{LN},x}} \exp\left[-\frac{(\log x - \mu)^2}{2\sigma_{\text{LN},x}^2}\right] dx & \text{if } x \geq 0 \\ 0 & \text{if } x < 0 \end{cases} \quad (\text{A.8})$$

The average is given by

$$\langle x \rangle = \exp\left[\mu + \frac{\sigma_{\text{LN},x}^2}{2}\right]. \quad (\text{A.9})$$

The n -th moment is described as

$$\begin{aligned} \langle x^n \rangle &= \int_0^\infty x^n P_{\text{LN}}(x) dx, \\ &= \exp\left[n\mu + \frac{n^2\sigma_{\text{LN},x}^2}{2}\right] = \langle x \rangle^n \exp\left[\frac{n(n-1)\sigma_{\text{LN},x}^2}{2}\right]. \end{aligned} \quad (\text{A.10})$$

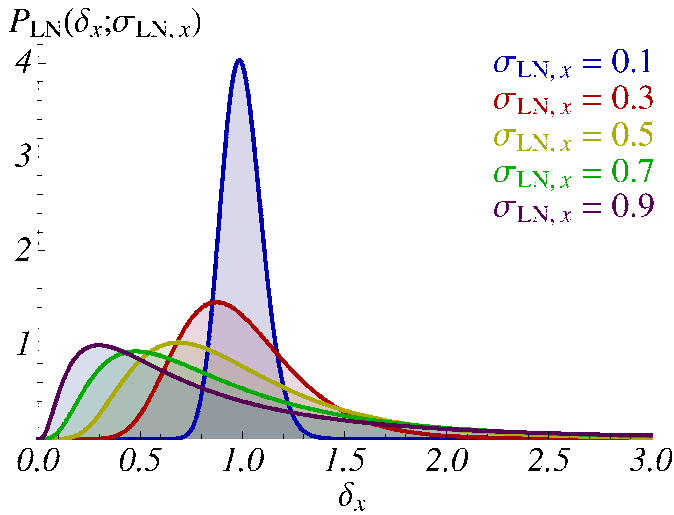


Figure A.1: The lognormal PDF. Each color indicates different value of $\sigma_{\text{LN},x}$: Blue, red, yellow, green, and purple correspond to $\sigma_{\text{LN},x} = 0.1, 0.3, 0.5, 0.7$, and 0.9 , respectively.

We can rewrite equation (A.8) in terms of $\delta_x \equiv x/\langle x \rangle$:

$$P_{\text{LN}}(\delta_x; \sigma_{\text{LN},x}) d\delta_x = \begin{cases} \frac{1}{\sqrt{2\pi}\sigma_{\text{LN},x}} \exp\left[-\frac{(\log \delta_x - \sigma_{\text{LN},x}^2/2)^2}{2\sigma_{\text{LN},x}^2}\right] \frac{d\delta_x}{\delta_x} & \text{if } \delta_x \geq 0 \\ 0 & \text{if } \delta_x < 0 \end{cases} \quad (\text{A.11})$$

Figure A.1 shows $P_{\text{LN}}(\delta_x; \sigma_{\text{LN},x})$ with five different values of $\sigma_{\text{LN},x} = 0.1, 0.3, 0.5, 0.7$, and 0.9 .

A.2 The Bivariate Log-normal Function

Let us consider two random variables x and y . The joint probability of the occurrence of the event C and D is denoted by $\mathbf{P}(C \cap D)$. The joint distribution function is defined as

$$\begin{aligned} F(x', y') &\equiv \mathbf{P}(C \cap D), \\ C : x &\leq x', D : y \leq y'. \end{aligned} \quad (\text{A.12})$$

The joint probability density function (joint PDF) is defined as

$$P(x', y') \equiv \frac{\partial^2}{\partial x' \partial y'} F(x', y'). \quad (\text{A.13})$$

In the x - y space, the probability of an infinitesimal region $(x'-x' + dx', y'-y' + dy')$ is obtained as

$$\mathbf{P}(x' \leq x < x' + dx' \cap x' \leq y < y' + dy') = P(x', y') dx' dy'. \quad (\text{A.14})$$

The marginal probability density function (marginal PDF) of x and y are defined as

$$P_x(x) \equiv \int_{-\infty}^{\infty} dy P(x, y), \quad (\text{A.15})$$

$$P_y(y) \equiv \int_{-\infty}^{\infty} dx P(x, y). \quad (\text{A.16})$$

The marginal PDF corresponds to the PDF of each the random variable.

The bivariate log-normal function is given by,

$$\begin{aligned} P_{\text{BLN}}(x, y; \sigma_{\text{LN}, x}; \sigma_{\text{LN}, y}) dx dy &= \frac{(1 - \rho^2)^{-1/2}}{2\pi \sigma_{\text{LN}, x} \sigma_{\text{LN}, y}} \exp \left[-\frac{A_x^2 - 2\rho' A_x B_y + B_y^2}{2(1 - \rho^2)} \right] \frac{dx}{x} \frac{dy}{y}, \\ \rho' &\equiv \frac{\log [\rho (\exp \sigma_{\text{LN}, x}^2 - 1)^{1/2} (\exp \sigma_{\text{LN}, y}^2 - 1)^{1/2} + 1]}{\sigma_{\text{LN}, y} \sigma_{\text{LN}, x}}, \\ A_x &\equiv (\log(x) + \sigma_{\text{LN}, x}^2/2) / \sigma_{\text{LN}, x}, \\ B_y &\equiv (\log(y) + \sigma_{\text{LN}, y}^2/2) / \sigma_{\text{LN}, y}, \end{aligned} \quad (\text{A.17})$$

where ρ is the correlation coefficient between x and y . If there is no correlation $\rho = 0$ and we obtain $P_{\text{BLN}}(x, y; \sigma_{\text{LN}, x}; \sigma_{\text{LN}, y}) = P_{\text{LN}}(x; \sigma_{\text{LN}, x}) P_{\text{LN}}(y; \sigma_{\text{LN}, y})$. The marginal probability density function of x and y are equal to $P_{\text{LN}}(x; \sigma_{\text{LN}, x})$ and $P_{\text{LN}}(y; \sigma_{\text{LN}, y})$, respectively.

A.3 Distribution of the Random Variable Squared

If one assumes that fluctuations, $\delta_x = x/\langle x \rangle$, follow the lognormal distribution, $P_{\text{LN}}(\delta_x; \sigma_{\text{LN}, x})$, the fluctuations of the density squared, $\delta_{xx} \equiv x^2/\langle x^2 \rangle$ can be written as

$$\delta_{xx} = \delta_x^2 \frac{\langle x \rangle^2}{\langle x^2 \rangle} = \delta_x^2 \exp(-\sigma_{\text{LN}, x}^2). \quad (\text{A.18})$$

The relation between δ_x and δ_{xx} is

$$\delta_x = \sqrt{\delta_{xx}} \exp(\sigma_{\text{LN},x}^2/2). \quad (\text{A.19})$$

Because δ_x follows $P_{\text{LN}}(\delta_x; \sigma_{\text{LN},x})$, the distribution of δ_{xx} is obtained as

$$P_{\text{LNS}}(\delta_{xx}; \sigma_{\text{LN},x}) = P_{\text{LN}}(\delta_x; \sigma_{\text{LN},x}) \left| \frac{d\delta_x}{d\delta_{xx}} \right| = P_{\text{LN}}(\delta_{xx}; 2\sigma_{\text{LN},x}). \quad (\text{A.20})$$

Therefore, δ_{xx} follows the lognormal distribution with lognormal standard deviation of $2\sigma_{\text{LN},x}$.

In the case that fluctuations, $\delta_x = x/\langle x \rangle$, follow a Gaussian:

$$P_{\text{G}}(\delta_x; \sigma_x) = \frac{1}{\sqrt{2\pi}\sigma_x} \exp\left[-\frac{(\delta_x - 1)^2}{2\sigma_x^2}\right], \quad (\text{A.21})$$

the relation between δ_x and δ_{xx} is

$$\delta_x = \sqrt{\delta_{xx}(1 + \sigma_x^2)}. \quad (\text{A.22})$$

The distribution of δ_{xx} is obtained as

$$P_{\text{GS}}(\delta_{xx}; \sigma_{\text{LN},x}) = P_{\text{G}}(\delta_x; \sigma_x) \left| \frac{d\delta_x}{d\delta_{xx}} \right| = \frac{\sqrt{1 + \sigma_x^2}}{\sqrt{8\pi\delta_{xx}}\sigma_x} \exp\left\{-\frac{[\sqrt{\delta_{xx}(1 + \sigma_x^2)} - 1]^2}{2\sigma_x^2}\right\}. \quad (\text{A.23})$$

Therefore, δ_{xx} follows $P_{\text{GS}}(\delta_{xx}; \sigma_{\text{LN},x})$, namely the Gaussian squared distribution, not a simple Gaussian. The shapes of the lognormal distribution, the Gaussian squared distribution, and a Gaussian are shown in Figure A.2.

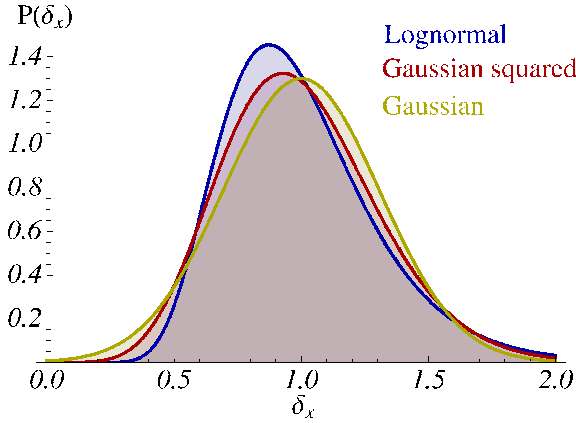


Figure A.2: The lognormal distribution (blue; $\sigma_{\text{LN},x} = 0.3$), the Gaussian squared distribution (red; $\sigma_x = 0.156$), and a Gaussian (yellow; $\sigma_x = 0.307$). Each distribution has the same variance.

Appendix B

Density and Temperature Distributions on a Sphere of the Triaxial Model

Triaxial model clusters are constructed simply by stretching spherical clusters along the three axis directions by a factor of λ_a , λ_b , and λ_c , respectively. The density (or temperature) of triaxial model is dependent on a single parameter:

$$\tilde{r} = \sqrt{\mu_A^2 x^2 + \mu_B^2 y^2 + z^2}, \quad (\text{B.1})$$

where $\mu_A \equiv \lambda_c/\lambda_a$, and $\mu_B \equiv \lambda_c/\lambda_b$ ($\lambda_c \leq \lambda_b \leq \lambda_a$). Therefore, density distribution at a constant radius r can be given by the distribution of \tilde{r} at r .

$$\begin{aligned} P(\delta_n; r) &= \frac{\partial \tilde{r}}{\partial \delta_n} P(\tilde{r})|_{|\tilde{r}|=r} \\ &= \frac{\partial \tilde{q}_r}{\partial \delta_n} P(\tilde{q}_r) = \frac{\bar{n}(r)}{r} \frac{\partial \tilde{r}}{\partial n} P(\tilde{q}_r)|_{|\tilde{r}|=r}, \end{aligned} \quad (\text{B.2})$$

where we define $\tilde{q}_r \equiv \tilde{r}/r$. By expressing equation (B.1) in polar coordinate, we obtain

$$\tilde{q}_r(\theta, \phi) = \sqrt{\mu_A^2 \sin^2 \theta \cos^2 \phi + \mu_B^2 \sin^2 \theta \sin^2 \phi + \cos^2 \theta}. \quad (\text{B.3})$$

Assuming random realization on a sphere, the probability of (θ, ϕ) is

$$P(\theta, \phi) d\theta d\phi = \sin \theta d\theta d\phi. \quad (\text{B.4})$$

We can convert $P(\theta, \phi)$ to $P(\tilde{q}_r, \phi)$ and obtain $P(\tilde{q}_r)$ by integrating $P(\tilde{q}_r, \phi)$ over ϕ :

$$\begin{aligned}
P(\tilde{q}_r) &= \frac{1}{2\pi} \int d\phi P(\tilde{q}_r, \phi) \\
&= \frac{1}{2\pi} \int d\phi P(\theta, \phi) \left| \frac{\partial(\cos \theta)}{\partial \tilde{q}_r} \frac{d\theta}{d(\cos \theta)} \right| \\
&= \frac{1}{2\pi} \int d\phi \left| \frac{\partial(\cos \theta)}{\partial \tilde{q}_r} \right| \\
&= \frac{1}{2\pi} \int d\phi \frac{\tilde{q}_r}{\sqrt{(1 - \mu_A^2 \cos^2 \phi - \mu_B^2 \sin^2 \phi)(\tilde{q}_r^2 - \mu_A^2 \cos^2 \phi - \mu_B^2 \sin^2 \phi)}}, \quad (\text{B.5})
\end{aligned}$$

where we assume $\mu_A \leq \mu_B \leq 1$ ($\lambda_c \leq \lambda_b \leq \lambda_a$). The integration range of ϕ is constrained by the existence condition of θ in equation (B.3). For $0 \leq \theta \leq 2\pi$, equation (B.3) provides the condition $\sqrt{\mu_A^2 \cos^2 \phi + \mu_B^2 \sin^2 \phi} \leq \tilde{q}_r \leq 1$. Therefore, the possible range of ϕ is $\sqrt{(\mu_B^2 - \tilde{q}_r^2)/(\mu_B^2 - \mu_A^2)} \leq \cos \phi \leq 1$ for $\tilde{q}_r < \mu_B$, while any ϕ ($0 \leq \phi \leq \pi$) is possible for $\tilde{q}_r \geq \mu_B$. The integration of equation (B.5) is analytically solved for the oblate case ($\mu_A = \mu_B \leq 1; \lambda_c \leq \lambda_b = \lambda_a$):

$$P(\tilde{q}_r) = \frac{\tilde{q}_r}{\sqrt{(1 - \mu_A^2)(\tilde{q}_r^2 - \mu_A^2)}}. \quad (\text{B.6})$$

We obtain the prolate case ($\mu_A \leq \mu_B = 1; \lambda_c = \lambda_b \leq \lambda_a$) in similarly,

$$P(\tilde{q}_r) = \frac{\tilde{q}_r}{\sqrt{(\mu_A^2 - 1)(\tilde{q}_r^2 - 1)}}. \quad (\text{B.7})$$

Figure B.1 displays $P(\tilde{q}_r)$ for four different sets of the axis ratio. To confirm the analytical results, we perform the Monte-Carlo simulation for 10^7 random realizations on a sphere (black lines). The numerical results well agree with analytic ones. The peak position corresponds to $\tilde{q}_r = \mu_B$.

For the density profile, we here assume the triaxial β model expressed as

$$n(\tilde{r}) = n_0 \left[1 + \left(\frac{\tilde{r}}{\tilde{r}_c} \right)^2 \right]^{-3\beta/2}. \quad (\text{B.8})$$

Figure B.2 displays the density distributions on a sphere at $r = \tilde{r}_c$ (blue) and $r = 5\tilde{r}_c$ (red) assuming $\beta = 2/3$. As shown the figure, the distribution has characteristic peaks. This result implies that the triaxial model cannot explain the lognormal-like distribution seen in the simulated clusters. Although we have considered the density distribution only, it is possible to apply the same procedure to the temperature distribution. Figure B.3 displays the temperature distributions on a sphere at $r = \tilde{r}_c$ (blue) and $r = 5\tilde{r}_c$ (red) assuming the triaxial polytropic model with $\gamma = 1.2$:

$$\begin{aligned}
T(\tilde{r}) &= T_0 [n(\tilde{r})/n_0]^{\gamma-1} \\
&= T_0 \left[1 + \left(\frac{\tilde{r}}{\tilde{r}_c} \right)^2 \right]^{-3\beta(\gamma-1)/2}. \quad (\text{B.9})
\end{aligned}$$

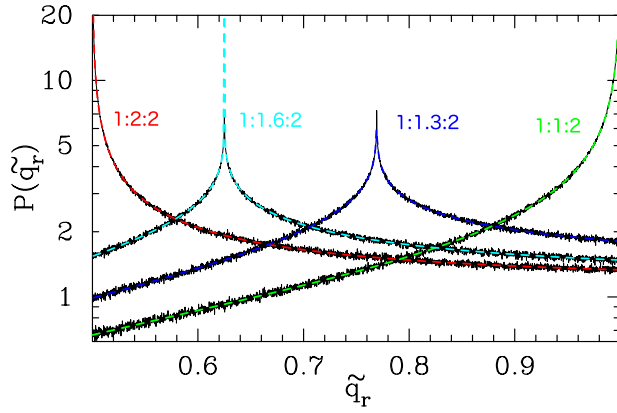


Figure B.1: The shape of $P(\tilde{q}_r)$. Each color indicates different axis ratio : $\lambda_c : \lambda_b : \lambda_a = 1 : 1 : 2$ (green), $1 : 1.3 : 2$ (blue), $1 : 1.6 : 2$ (cyan), and $1 : 2 : 2$ (red). Thin black lines are the results of Monte-Carlo simulation for 10^7 random realizations on a sphere.

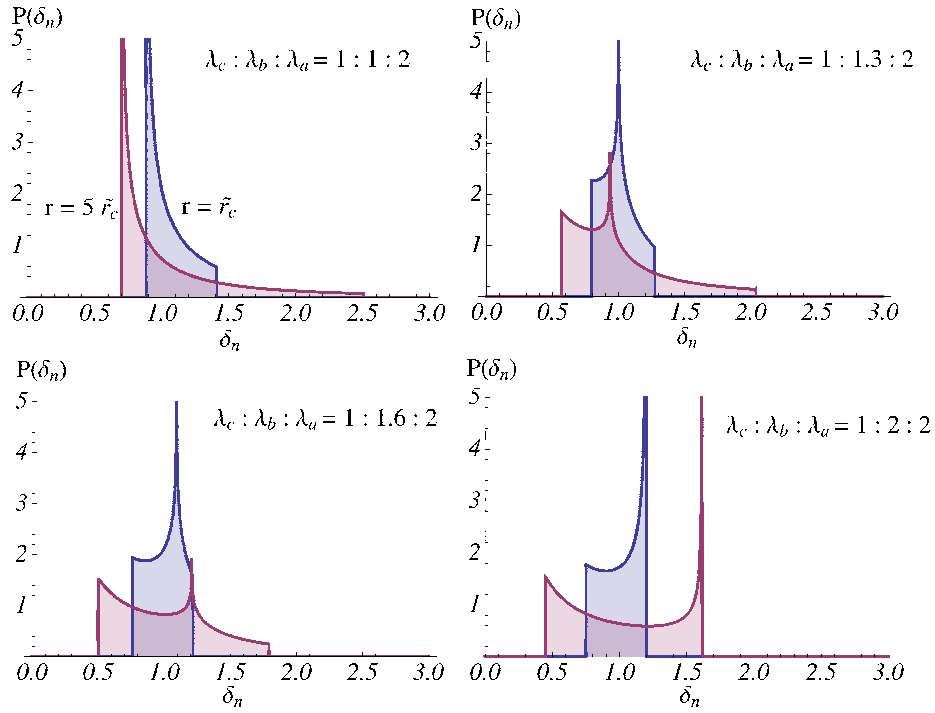


Figure B.2: The density distribution on a sphere of the triaxial β model with $\beta = 2/3$. Each panel indicates different axis ratio (top left, top right, bottom left, and bottom right correspond to $\lambda_c : \lambda_b : \lambda_a = 1 : 1 : 2$, $1 : 1.3 : 2$, $1 : 1.6 : 2$, and $1 : 2 : 2$, respectively). Blue and Red lines correspond to the distributions on a sphere at $r = \tilde{r}_c$ and $r = 5\tilde{r}_c$, respectively.

The variance of the temperature distribution is smaller than that of density distribution due to the shallower radial profile.

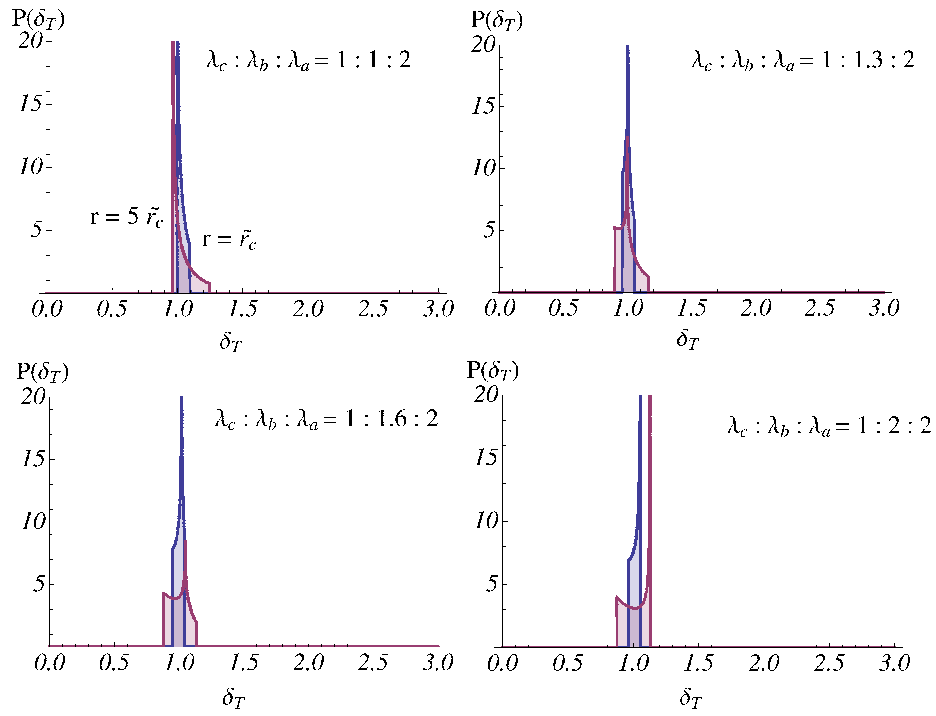


Figure B.3: The temperature distribution of the triaxial polytropic model with $\gamma = 1.2$ and $\beta = 2/3$. Each panel indicates same as Figure B.2.

Appendix C

Distribution of f_H for prolate and oblate ellipsoids

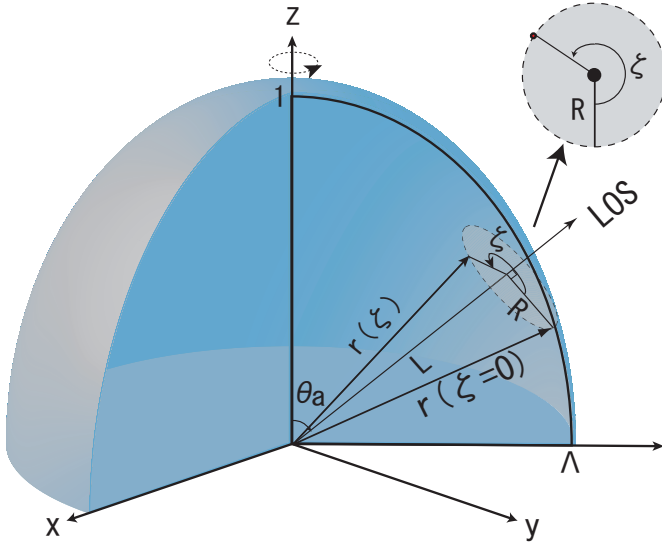


Figure C.1: Schematic representation of a prolate cluster with an axis ratio $\lambda_a : \lambda_b : \lambda_c = 1 : \Lambda : \Lambda$. Given the symmetry around the z -axis (the long axis), an LOS through the cluster center is specified by an angle θ_a from the z -axis. An arbitrary position in the cluster \mathbf{r} is expressed in terms of L (the projection of \mathbf{r} onto the LOS direction), R (the projection of \mathbf{r} onto the plane normal to the LOS), and ζ (the azimuthal angle on the plane normal to the LOS).

In this Appendix, we derive the distribution of f_H due to the asphericity of clusters, by considering the following two extreme cases; the prolate ($\lambda_a = \lambda_b < \lambda_c$) and the oblate ($\lambda_a < \lambda_b = \lambda_c$) ellipsoids. We choose z -axis as the long (short) axis and x - and y -axes as the short (long) axes for an prolate (oblate) ellipsoid. The direction of the unit vector along the LOS of an

observer, \mathbf{a} , is defined in terms of the spherical coordinate $(\theta_{\mathbf{a}}, \phi_{\mathbf{a}})$. Figure C.1 shows a schematic picture of a prolate ellipsoid.

Let us define the quantity $\Lambda \equiv \lambda_a/\lambda_c = \lambda_b/\lambda_c$ ($\Lambda \equiv \lambda_b/\lambda_a = \lambda_c/\lambda_a$) for the prolate (oblate) ellipsoid. We assume that the gas density follows the *prolate (oblate)* β model:

$$n(\mathbf{r})|_{\theta_{\mathbf{a}}} = n_0 (1 + (\tilde{r}/r_c)^2)^{-3\beta/2}, \quad (\text{C.1})$$

$$\tilde{r} \equiv |\mathbf{r}|[\sin^2 \theta_{\mathbf{r}}/\Lambda^2 + \cos^2 \theta_{\mathbf{r}}]^{1/2}, \quad (\text{C.2})$$

and $\theta_{\mathbf{r}}$ is the angle between z -axis and \mathbf{r} . Because the surface brightness profile is independent of $\phi_{\mathbf{a}}$ due to the z -axial symmetry, one can express f_H as function of $\theta_{\mathbf{a}}$.

For an isothermal cluster, the surface brightness averaged over a circle of radius R is proportional to $\int n^2 dL$ averaged over the angle ζ of the circle. We put $\zeta = 0$ where \mathbf{r} is located on the same plane defined by the LOS and z -axis. To compute the averaged surface brightness, we need an expression of the density n as a function of L , R , and ζ . In Cartesian coordinates, $\mathbf{r}(\zeta = 0)$ is

$$\mathbf{r}(\zeta = 0) = \begin{pmatrix} \sqrt{R^2 + L^2} \cos \phi_{\mathbf{a}} \sin(\arctan R/L + \theta_{\mathbf{a}}) \\ \sqrt{R^2 + L^2} \sin \phi_{\mathbf{a}} \sin(\arctan R/L + \theta_{\mathbf{a}}) \\ \sqrt{R^2 + L^2} \cos(\arctan R/L + \theta_{\mathbf{a}}) \end{pmatrix}. \quad (\text{C.3})$$

Multiplying the rotation matrix around \mathbf{a} , $M_{\mathbf{a}}(\zeta)$ to $\mathbf{r}(\zeta = 0)$, we obtain

$$\begin{aligned} \mathbf{r}(\zeta) &= M_{\mathbf{a}}(\zeta)\mathbf{r}(\zeta = 0) \\ &= \begin{pmatrix} R \cos \zeta \cos \phi_{\mathbf{a}} \cos \theta_{\mathbf{a}} + R \sin \zeta \sin \phi_{\mathbf{a}} + L \cos \phi_{\mathbf{a}} \sin \theta_{\mathbf{a}} \\ R \cos \zeta \sin \phi_{\mathbf{a}} \cos \theta_{\mathbf{a}} - R \sin \zeta \cos \phi_{\mathbf{a}} + L \sin \phi_{\mathbf{a}} \sin \theta_{\mathbf{a}} \\ L \cos \theta_{\mathbf{a}} - R \cos \zeta \sin \theta_{\mathbf{a}} \end{pmatrix}, \end{aligned} \quad (\text{C.4})$$

where

$$M_{\mathbf{a}}(\zeta) \equiv \begin{pmatrix} x_{\mathbf{a}}^2 + (1 - x_{\mathbf{a}}^2) \cos \zeta & x_{\mathbf{a}} y_{\mathbf{a}} (1 - \cos \zeta) + z_{\mathbf{a}} \sin \zeta & z_{\mathbf{a}} x_{\mathbf{a}} (1 - \cos \zeta) - y_{\mathbf{a}} \sin \zeta \\ x_{\mathbf{a}} y_{\mathbf{a}} (1 - \cos \zeta) - z_{\mathbf{a}} \sin \zeta & y_{\mathbf{a}}^2 + (1 - y_{\mathbf{a}}^2) \cos \zeta & y_{\mathbf{a}} z_{\mathbf{a}} (1 - \cos \zeta) + x_{\mathbf{a}} \sin \zeta \\ z_{\mathbf{a}} x_{\mathbf{a}} (1 - \cos \zeta) + y_{\mathbf{a}} \sin \zeta & y_{\mathbf{a}} z_{\mathbf{a}} (1 - \cos \zeta) - x_{\mathbf{a}} \sin \zeta & z_{\mathbf{a}}^2 + (1 - z_{\mathbf{a}}^2) \cos \zeta \end{pmatrix}, \quad (\text{C.5})$$

and

$$\begin{pmatrix} x_{\mathbf{a}} \\ y_{\mathbf{a}} \\ z_{\mathbf{a}} \end{pmatrix} \equiv \begin{pmatrix} \cos \phi_{\mathbf{a}} \sin \theta_{\mathbf{a}} \\ \sin \phi_{\mathbf{a}} \sin \theta_{\mathbf{a}} \\ \cos \theta_{\mathbf{a}} \end{pmatrix}. \quad (\text{C.6})$$

Thus, we obtain

$$|\mathbf{r}(\zeta)| \cos \theta_{\mathbf{r}} = L \cos \theta_{\mathbf{a}} - R \cos \zeta \sin \theta_{\mathbf{a}}. \quad (\text{C.7})$$

Then, $|\mathbf{r}(\zeta)|$ and $\theta_{\mathbf{r}}$ are written as

$$|\mathbf{r}(\zeta)| = \sqrt{L^2 + R^2} \quad (\text{C.8})$$

$$\theta_{\mathbf{r}} = \arccos \left(\frac{L \cos \theta_{\mathbf{a}} - R \cos \zeta \sin \theta_{\mathbf{a}}}{\sqrt{L^2 + R^2}} \right). \quad (\text{C.9})$$

Combining with equation (C.1), we can write $n(\mathbf{r})|_{\theta_{\mathbf{a}}}$ in terms of L, R , and ζ as

$$n(\mathbf{r})|_{\theta_{\mathbf{a}}} = n_0 \left(1 + (\tilde{r}(R, L, \zeta)|_{\theta_{\mathbf{a}}}/r_c)^2\right)^{-3\beta/2} \equiv n(R, L, \zeta), \quad (\text{C.10})$$

where

$$\tilde{r}(R, L, \zeta)|_{\theta_{\mathbf{a}}} \equiv \tilde{r} = \frac{\sqrt{L^2 + R^2 + [\Lambda^2 - 1](L \cos \theta_{\mathbf{a}} - R \cos \zeta \sin \theta_{\mathbf{a}})^2}}{\Lambda}. \quad (\text{C.11})$$

Then, the averaged surface brightness at R is

$$\begin{aligned} S_x(R)|_{\theta_{\mathbf{a}}} &= \frac{1}{2\pi} \int_0^{2\pi} d\zeta \int_{-\infty}^{\infty} dL [n(R, L, \zeta)|_{\theta_{\mathbf{a}}}]^2 \\ &= \frac{n_0^2 r_c}{2\pi} \int_0^{2\pi} d\zeta \int_{-\infty}^{\infty} dq_L \left[\frac{q_L^2 + q_R^2 + (\Lambda^2 - 1)(q_L \cos \theta_{\mathbf{a}} - q_R \cos \zeta \sin \theta_{\mathbf{a}})^2}{\Lambda^2} + 1 \right]^{-3\beta} \\ &\equiv \frac{n_0^2 r_c}{2\pi} I(q_R)|_{\theta_{\mathbf{a}}} \end{aligned} \quad (\text{C.12})$$

where we define the normalized length by r_c , $q_R \equiv R/r_c, q_L \equiv L/r_c$. We compute $I(q_R)|_{\theta_{\mathbf{a}}}$ numerically for $\Lambda = 0.5$ (prolate) and $\Lambda = 2.0$ (oblate) adopting $\beta = 0.65$. We fit $I(q_R)|_{\theta_{\mathbf{a}}}$ from $q_R = 0$ to $q_R = 10.0$ by with a functional form of the surface brightness profile assuming the spherical beta model ($\propto [1 + (q_R/q_{c,\text{fit}}|_{\theta_{\mathbf{a}}})^2]^{-3\beta_{\text{fit}}|_{\theta_{\mathbf{a}}} + 1/2}$). Thus, we obtain the counter part of $r_{c,\text{iso}\beta}$, $q_{c,\text{fit}}|_{\theta_{\mathbf{a}}} \equiv r_{c,\text{fit},S_x}/r_c$ and the fitted value of β , $\beta_{\text{fit}}|_{\theta_{\mathbf{a}}}$. While, $q_{c,\text{iso}\beta}|_{\theta_{\mathbf{a}}} \equiv r_{c,\text{iso}\beta}/r_c$ is written as

$$q_{c,\text{iso}\beta}|_{\theta_{\mathbf{a}}} = (\sin^2 \theta_{\mathbf{a}}/\Lambda^2 + \cos^2 \theta_{\mathbf{a}})^{-1/2} \frac{G(\beta)G(\beta_{\text{fit}}|_{\theta_{\mathbf{a}}}/2)^2}{G(\beta/2)^2 G(\beta_{\text{fit}}|_{\theta_{\mathbf{a}}})}. \quad (\text{C.13})$$

The first term of the right-hand side represents the elongation of the radius toward the LOS. The second term is the correction to the use of $\beta_{\text{fit}}|_{\theta_{\mathbf{a}}}$ in observation instead of the true β . However, the correction is very small (within 0.01% error).

Finally, we obtain the bias of H_0 as a function of $\theta_{\mathbf{a}}$,

$$f_H(\theta_{\mathbf{a}}) \equiv \frac{q_{c,\text{fit}}|_{\theta_{\mathbf{a}}}}{q_{c,\text{iso}\beta}|_{\theta_{\mathbf{a}}}}. \quad (\text{C.14})$$

The probability of f_H for the random assignment is proportional to the solid angle $\Omega(f_H)$. If $f_H(\theta_{\mathbf{a}})$ is a monotonic function, the PDF of f_H is obtained as

$$\begin{aligned} P(f_H) &= \frac{1}{4\pi} \frac{d\Omega}{df_H} = \frac{1}{4\pi} \frac{d\Omega}{d\theta_{\mathbf{a}}} \left| \frac{d\theta_{\mathbf{a}}}{df_H} \right| \\ &= \frac{\sin \theta_{\mathbf{a}}(f_H)}{2} \left| \frac{d\theta_{\mathbf{a}}(f_H)}{df_H} \right|, \end{aligned} \quad (\text{C.15})$$

where $\theta_{\mathbf{a}}(f_H) = f_H^{-1}(\theta_{\mathbf{a}})$.

Dotted lines in the upper panel of Figure C.2 show equation (C.15) for prolate ($\Lambda = 0.5$) and oblate ($\Lambda = 2.0$) ellipsoids. As shown in the lower panel, the corresponding $\theta_{\mathbf{a}}$ is a monotonically

increasing (decreasing) function of f_H for the prolate (oblate) ellipsoid. At $\theta_{\mathbf{a}} = 0$, f_H is equal to Λ , which corresponds to the case that the LOS is along the z -axis.

The PDF diverges at $\theta_{\mathbf{a}} = \pi/2$. This can be understood as follows. Equations (C.13) to (C.15) imply that

$$P(f_H) \propto \sin \theta_{\mathbf{a}}(f_H) \left| \frac{dq_{c,\text{fit}}^{-1}}{d\theta_{\mathbf{a}}(f_H)} \right|^{-1} \propto \frac{\sqrt{\cos^2 \theta_{\mathbf{a}}(f_H) + \Lambda^{-2} \sin^2 \theta_{\mathbf{a}}(f_H)}}{\cos \theta_{\mathbf{a}}(f_H)}, \quad (\text{C.16})$$

where we ignore the $\theta_{\mathbf{a}}$ -dependence of $q_{c,\text{fit}}|\theta_{\mathbf{a}}$ and $\beta_{\text{fit}}|\theta_{\mathbf{a}}$. Thus $\theta_{\mathbf{a}} \approx \pi/2$, $P(f_H)$ diverges as $1/\cos \theta_{\mathbf{a}}$. Note, however, its integration over a finite size of f_H does not diverge (see eq.[C.15]). This is plotted in the solid histograms, where the bin size $\Delta f_H = 0.05$ is adopted. The resulting distribution is skewed positively (negatively) for the prolate (oblate) ellipsoid, which is consistent with the results shown in Figure 5.3.

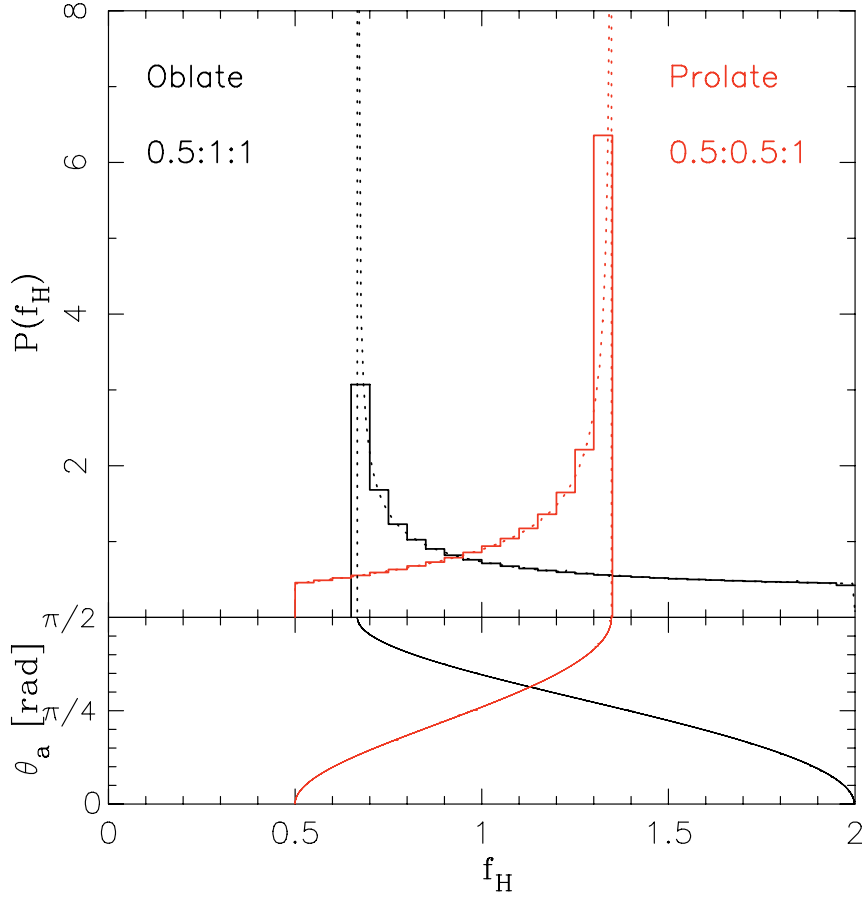


Figure C.2: Upper: The PDF of f_H for the oblate ($\Lambda = 2$; black curves) and prolate ($\lambda = 0.5$; red curves) ellipsoids. Dotted lines represent equation (C.15), while solid lines show the corresponding histograms with a bin size of $\Delta f_H = 0.05$. Lower: The angle, $\theta_{\mathbf{a}}$, as a function of f_H .

Appendix D

Relation of Density and Surface Brightness Distributions Under the Thick-slice Approximation

Modeling galaxy clusters with a spherical isothermal β model (Eq. [6.7]), the surface brightness at an arbitrary projected angular radius, θ , is given by

$$\begin{aligned}
 S_x(\theta) &\propto \int_{-\infty}^{\infty} [n(\mathbf{r})]^2 dl \\
 &= \int_{-\infty}^{\infty} \delta_{nn}(\mathbf{r}) \langle n^2 \rangle (r = \sqrt{l^2 + d_A^2 \theta^2}) dl \\
 &= M_2 n_0^2 \left(1 + \frac{d_A^2 \theta^2}{r_c^2}\right)^{-3\beta} \int_{-\infty}^{\infty} \delta_{nn}(\mathbf{r}) \left[1 + \left(\frac{l}{r_{c,\text{eff}}(\theta)}\right)^2\right]^{-3\beta} dl, \tag{D.1}
 \end{aligned}$$

where $r_{c,\text{eff}}(\theta) \equiv \sqrt{r_c^2 + d_A^2 \theta^2}$, and we assume the $\sigma_{\text{LX},x}$ in equation 3.6 is independent of r . Therefore, the second moment of n ($M_2 \equiv \langle n^2 \rangle / \langle n \rangle^2 = \exp(-\sigma_{\text{LN},n}^2)$) is also independent of r . In the above, we use $\langle n \rangle = \bar{n}(r)$.

The ensemble average of $\langle S_x(\theta) \rangle$ can be expressed as

$$\begin{aligned}
 \langle S_x(\theta) \rangle &\propto \int_{-\infty}^{\infty} \langle n^2 \rangle (r = \sqrt{l^2 + d_A^2 \theta^2}) dl \\
 &= \sqrt{\pi} n_0^2 M_2 r_c \frac{\Gamma(3\beta - 1/2)}{\Gamma(3\beta)} \left(1 + \frac{d_A^2 \theta^2}{r_c^2}\right)^{-3\beta+1/2} \tag{D.2}
 \end{aligned}$$

Combining equations (D.1) and (D.2), $\delta_{S_x,\text{ens}}$ reduces to

$$\begin{aligned}
 \delta_{S_x,\text{ens}}(\theta) &= \kappa_\beta \int_{-\infty}^{\infty} \delta_{nn}(\mathbf{r}) \left[1 + \left(\frac{l}{r_{c,\text{eff}}(\theta)}\right)^2\right]^{-3\beta} d\left(\frac{l}{r_{c,\text{eff}}(\theta)}\right) \\
 \kappa_\beta &\equiv \pi^{-1/2} \frac{\Gamma(3\beta)}{\Gamma(3\beta - 1/2)}. \tag{D.3}
 \end{aligned}$$

Now, fixing θ , let us consider the three-dimensional field $\delta_{nn}(\mathbf{r})W_\beta(l)$ and its projected two-dimensional field $\delta_{S_X, \text{ens}}|_\theta$, defined as

$$\delta_{S_X, \text{ens}}|_\theta = \int_{-\infty}^{\infty} \delta_{nn}(\mathbf{r})W_\beta(l')dl' \quad (\text{D.4})$$

$$W_\beta(l') \equiv \kappa_\beta(1+l'^2)^{-3\beta}, \quad (\text{D.5})$$

where we use a dimensionless length normalized by $r_{c, \text{eff}}(\theta)$ distinguished by prime ($l' \equiv l/r_{c, \text{eff}}(\theta)$, $k'_l \equiv k_l r_{c, \text{eff}}(\theta)$). Then, we can consider the variance of the $\delta_{S_X, \text{ens}}|_\theta$ -field,

$$\sigma_{\delta_{S_X, \text{ens}}|_\theta}^2 = \frac{1}{(2\pi)^2} \int d\mathbf{K}' P_{S_X, \text{ens}}|_\theta(\mathbf{K}'), \quad (\text{D.6})$$

where $P_{S_X, \text{ens}}|_\theta(\mathbf{K}')$ is the (two-dimensional) power spectrum of $\delta_{S_X, \text{ens}}|_\theta$. The variance of the δ_{nn} field can also be written as

$$\sigma_{\delta_{nn}}^2 = \frac{1}{(2\pi)^3} \int d\mathbf{k}' P_{nn}(\mathbf{k}'). \quad (\text{D.7})$$

With this, the relation between $P_{S_X, \text{ens}}(\mathbf{K}')$ and $P_{nn}(\mathbf{k}')$ is

$$P_{S_X, \text{ens}}|_\theta(\mathbf{K}') = \frac{1}{2\pi} \int dk'_l P_{nn}(\mathbf{k}') |\widetilde{W}_\beta(k'_l)|^2. \quad (\text{D.8})$$

The Fourier conjugate $\widetilde{W}_\beta(k'_l)$ is given by

$$\widetilde{W}_\beta(k'_l) = \kappa_\beta \left(\frac{2}{k'_l} \right)^{-3\beta+1/2} \frac{2\sqrt{\pi}}{\Gamma(3\beta)} K_{-3\beta+1/2}(k'_l), \quad (\text{D.9})$$

where $K_{-3\beta+1/2}(k'_l)$ is modified Bessel function of the second kind .

In the case that the largest scale fluctuation is smaller than the physical scale (the thick-slice approximation, following Fischera & Dopita (2004)), the Fourier conjugate of the window function becomes the Dirac-delta function, $|\widetilde{W}_\beta(k'_l)|^2 \sim g(\beta)\delta(k'_l)$. The normalization factor $g(\beta)$ is given by

$$g(\beta) \equiv 2 \int_0^\infty dk'_l |\widetilde{W}_\beta(k'_l)|^2 = 2\sqrt{\pi} \frac{\Gamma(3\beta)^2 \Gamma(6\beta - 1/2)}{\Gamma(3\beta - 1/2)^2 \Gamma(6\beta)}. \quad (\text{D.10})$$

Let us define the effective width

$$\Delta_{\text{eff}}(\theta) \equiv 2\pi r_{c, \text{eff}}(\theta)/g(\beta) = \sqrt{\pi} \frac{\Gamma(3\beta - 1/2)^2 \Gamma(6\beta)}{\Gamma(3\beta)^2 \Gamma(6\beta - 1/2)} r_{c, \text{eff}}(\theta). \quad (\text{D.11})$$

Fischera & Dopita (2004) explore the column density distribution assuming a plane parallel geometry with width Δ . In the thick slice case, Δ_{eff} corresponds to Δ although they consider the column density not the surface brightness. We assume statistical isotropy and a power law spectrum with upper and lower limit ($k'_{\text{max}} \equiv k_{\text{max}} r_{c, \text{eff}}(\theta)$ and $k'_{\text{min}} \equiv k_{\text{min}} r_{c, \text{eff}}(\theta)$),

$$P_{nn}(\mathbf{k}') \begin{cases} \propto |\mathbf{k}'|^{\alpha_{nn}} & k'_{\text{min}} < |\mathbf{k}'| < k'_{\text{max}} \\ = 0 & \text{otherwise.} \end{cases} \quad (\text{D.12})$$

Finally, using equation (D.6), (D.7), and (D.8) under the thick-slice approximation, we obtain

$$\sigma_{\delta_{\text{Sx,ens}}|\theta}^2 / \sigma_{\delta_{nn}}^2 = \begin{cases} \frac{1(\alpha_{nn} + 3)(1 - \zeta^{\alpha_{nn}+2})}{2(\alpha_{nn} + 2)(1 - \zeta^{\alpha_{nn}+3})} \left(\frac{\Delta_{\text{eff}}(\theta)}{l_{\text{max}}} \right)^{-1} & \alpha_{nn} \neq -3 \text{ and } \alpha_{nn} \neq -2 \\ \frac{\log \zeta}{2(\zeta - 1)} \left(\frac{\Delta_{\text{eff}}(\theta)}{l_{\text{max}}} \right)^{-1} & \alpha_{nn} = -2 \\ \frac{1 - 1/\zeta}{2 \log \zeta} \left(\frac{\Delta_{\text{eff}}(\theta)}{l_{\text{max}}} \right)^{-1} & \alpha_{nn} = -3, \end{cases} \quad (\text{D.13})$$

where $\zeta \equiv k_{\text{max}}/k_{\text{min}}$ and $l_{\text{max}} \equiv 2\pi k_{\text{min}}^{-1}$.

Then, although $\sigma_{\delta_{\text{Sx,ens}}|\theta}^2$ is the variance of $\delta_{\text{Sx,ens}}|\theta$ -field, we regard it as the variance of the ensemble average of $\delta_{\text{Sx,ens}}(\mathbf{R}')$ at θ . The conversion to the standard deviation of logarithm is expressed as

$$\sigma_{\text{LN, Sx}} = \sqrt{\log(1 + \sigma_{\delta_{\text{Sx,ens}}|\theta}^2)} \quad (\text{D.14})$$

In Figure 6.3, we adopt $\zeta = L_{\text{box}}/(2d_{\text{grid}}) = f_s/f_{\text{Ny}}$, where f_s and f_{Ny} are the sampling frequency and the Nyquist frequency, respectively, and $l_{\text{max}} = L_{\text{box}}$. We also adopt the fitted value of α_{nn} in equation (D.13).

Appendix E

Effect of Poisson process to the observed surface brightness distribution

In this Appendix, we provide the observed surface brightness distribution in poor photon statistics. If the number of photons is not enough, the observed surface brightness $\delta_{\text{Sx}}^{\text{obs}}$ deviates from true surface brightness δ_{Sx} due to the discreteness effect.

First, let us consider the distribution in a specific radius R . Then, the expectation of the photon number is determined by the true surface brightness.

$$\overline{\mathcal{N}}(\delta_{\text{Sx}}) = \overline{\mathcal{N}}_1 \delta_{\text{Sx}}, \quad (\text{E.1})$$

where $\overline{\mathcal{N}}_1$ is the expected photon number of $\delta_{\text{Sx}} = 1$. The observed photon number \mathcal{N} distributes according to Poisson distribution:

$$P_{\text{P}}(\mathcal{N}; \overline{\mathcal{N}}) = \frac{e^{-\overline{\mathcal{N}}} \overline{\mathcal{N}}^{\mathcal{N}}}{\mathcal{N}!}. \quad (\text{E.2})$$

Then, the photon number distribution is expressed as

$$P(\mathcal{N}) = \int_0^{\infty} P(\delta_{\text{Sx}}) P_{\text{P}}(\mathcal{N}; \overline{\mathcal{N}}(\delta_{\text{Sx}})) d\delta_{\text{Sx}}, \quad (\text{E.3})$$

where $P(\delta_{\text{Sx}})$ is true surface brightness distribution. We can convert $P(\mathcal{N})$ to the observed surface brightness distribution $P(\delta_{\text{Sx}}^{\text{obs}})$.

$$P(\delta_{\text{Sx}}^{\text{obs}}) = \overline{\mathcal{N}}_1 \int_0^{\infty} P(\delta_{\text{Sx}}) P_{\text{P}}(\overline{\mathcal{N}}_1 \delta_{\text{Sx}}^{\text{obs}}; \overline{\mathcal{N}}(\delta_{\text{Sx}})) d\delta_{\text{Sx}}. \quad (\text{E.4})$$

Figure E.1 displays $P(\delta_{\text{Sx}}^{\text{obs}})$ assuming $P(\delta_{\text{Sx}}) = P_{\text{LN}}(\delta_{\text{Sx}}; \sigma_{\text{LN}, \text{Sx}} = 0.4)$.

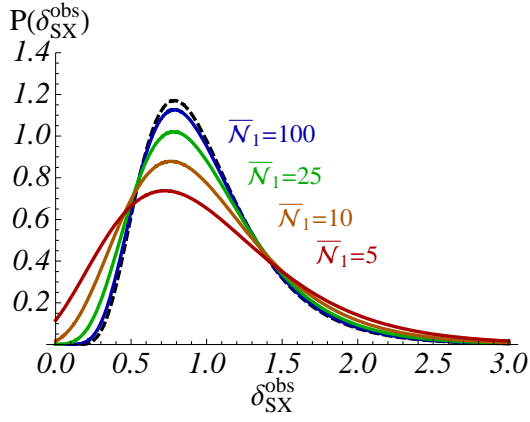


Figure E.1: The observed surface brightness distribution $P(\delta_{Sx}^{\text{obs}})$ on the assumption of $P(\delta_{Sx}) = P_{\text{LN}}(\delta_{Sx}; \sigma_{\text{LN}, Sx} = 0.4)$ with $\overline{N}_1 = 100, 25, 10$ and 5 . Dashed line indicates $P_{\text{LN}}(\delta_{Sx}; \sigma_{\text{LN}, Sx} = 0.4)$.

In general, the radial profile must be considered. Because we can use the above discussion at an arbitrary radius R , we can obtain the probability in general case

$$\begin{aligned}
 P(\delta_{Sx}^{\text{obs}}) &= \int dR W(R) \overline{N}_1(R) \int_0^\infty d\delta_{Sx} P(\delta_{Sx}; \sigma_{\text{LN}, Sx}) P_{\text{P}}(\overline{N}_1(R) \delta_{Sx}^{\text{obs}}; \overline{N}_1(R) \delta_{Sx}) \\
 &= \int_0^\infty d\delta_{Sx} P(\delta_{Sx}; \sigma_{\text{LN}, Sx}) \langle P_{\text{P}} \rangle(\delta_{Sx}^{\text{obs}}; \delta_{Sx}) \\
 \langle P_{\text{P}} \rangle(\delta_{Sx}^{\text{obs}}; \delta_{Sx}) &\equiv \int dR W(R) \overline{N}_1(R) P_{\text{P}}(\overline{N}_1(R) \delta_{Sx}^{\text{obs}}; \overline{N}_1(R) \delta_{Sx}) \tag{E.5}
 \end{aligned}$$

where $\overline{N}_1(R)$ is the average photon number at a radius R . $W(R)$ is the weight function ($\int dR W(R) = 1$). If we use the map without exclusion of the point sources, $W(R) \propto 2\pi R$. Because we can obtain $\overline{N}_1(R)$ from $\overline{S}_X(R)$, in principle, it is possible to derive $\langle P_{\text{P}} \rangle$, namely the averaged Poisson distribution and the fitting function $P(\delta_{Sx}^{\text{obs}})$ by fixing $\overline{N}_1(R)$.

References

- Abell, G. O. 1958, *ApJS*, 3, 211
- Allen, S. W., Schmidt, R. W., & Fabian, A. C. 2001, *Mon. Not. Roy. Astron. Soc.*, 328, L37
- Allen, S. W., Schmidt, R. W., & Fabian, A. C. 2001, *MNRAS*, 328, L37
- Ameglio, S., Borgani, S., Diaferio, A., & Dolag, K. 2006, *MNRAS*, 369, 1459
- Arnaud, K. A. 1996, in *Astronomical Society of the Pacific Conference Series*, Vol. 101, *Astronomical Data Analysis Software and Systems V*, ed. G. H. Jacoby & J. Barnes, 17–+
- Ascasibar, Y., Yepes, G., Mueller, V., & Gottloeber, S. 2003, *MNRAS*, 346, 731
- Avila-Reese, V., Firmani, C., Klypin, A., & Kravtsov, A. V. 1999, *MNRAS*, 310, 527
- Birkinshaw, M. 1999, *Phys. Rep.*, 310, 97
- Bonamente, M., Joy, M. K., LaRoque, S. J., Carlstrom, J. E., Reese, E. D., & Dawson, K. S. 2006, *ApJ*, 647, 25
- Borgani, S., Murante, G., Springel, V., Diaferio, A., Dolag, K., Moscardini, L., Tormen, G., Tornatore, L., & Tozzi, P. 2004, *MNRAS*, 348, 1078
- Breit, G., & Teller, E. 1940, *ApJ*, 91, 215
- Briel, U. G., Finoguenov, A., & Henry, J. P. 2004, *A&A*, 426, 1
- Carlstrom, J. E., Holder, G. P., & Reese, E. D. 2002, *ARA&A*, 40, 643
- Cavaliere, A., & Fusco-Femiano, R. 1976, *A&A*, 49, 137
- . 1978, *A&A*, 70, 677
- Clowe, D., Gonzalez, A., & Markevitch, M. 2004, *ApJ*, 604, 596
- Coles, P., & Jones, B. 1991, *MNRAS*, 248, 1
- de Vaucouleurs, G. 1948, *Annales d’Astrophysique*, 11, 247
- Dickey, J. M., & Lockman, F. J. 1990, *Ann. Rev. Astron. Astrophys.*, 28, 215

- Dolag, K., Hansen, F. K., Roncarelli, M., & Moscardini, L. 2005, *MNRAS*, 363, 29
- Dopita, M. A., & Sutherland, R. S. 2003, *Astrophysics of the diffuse universe (Astrophysics of the diffuse universe, Berlin, New York: Springer, 2003. Astronomy and astrophysics library, ISBN 3540433627)*
- Elmegreen, B. G. 2002, *ApJ*, 564, 773
- Fabian, A. C., Celotti, A., Blundell, K. M., Kassim, N. E., & Perley, R. A. 2002, *MNRAS*, 331, 369
- Fabian, A. C., Sanders, J. S., Taylor, G. B., Allen, S. W., Crawford, C. S., Johnstone, R. M., & Iwasawa, K. 2006, *MNRAS*, 366, 417
- Fahlman, G., Kaiser, N., Squires, G., & Woods, D. 1994, *ApJ*, 437, 56
- Felten, J. E., Gould, R. J., Stein, W. A., & Wolf, N. J. 1966, *ApJ*, 146, 955
- Fischera, J., & Dopita, M. A. 2004, *ApJ*, 611, 919
- Forman, W., Kellogg, E., Gursky, H., Tananbaum, H., & Giacconi, R. 1972, *ApJ*, 178, 309
- Freedman, W. L., Madore, B. F., Gibson, B. K., Ferrarese, L., Kelson, D. D., Sakai, S., Mould, J. R., Kennicutt, Jr., R. C., Ford, H. C., Graham, J. A., Huchra, J. P., Hughes, S. M. G., Illingworth, G. D., Macri, L. M., & Stetson, P. B. 2001, *ApJ*, 553, 47
- Fry, J. N., & Thomas, D. 1999, *ApJ*, 524, 591
- Fukushige, T., Kawai, A., & Makino, J. 2004, *ApJ*, 606, 625
- Furusho, T., Yamasaki, N. Y., Ohashi, T., Shibata, R., & Ezawa, H. 2001, *ApJ*, 561, L165
- Giacconi, R., Murray, S., Gursky, H., Kellogg, E., Schreier, E., & Tananbaum, H. 1972, *ApJ*, 178, 281
- Girardi, M., Giuricin, G., Mardirossian, F., Mezzetti, M., & Boschin, W. 1998, *ApJ*, 505, 74
- Gursky, H., Kellogg, E., Murray, S., Leong, C., Tananbaum, H., & Giacconi, R. 1971, *ApJ*, 167, L81+
- Hoekstra, H., Franx, M., Kuijken, K., & Squires, G. 1998, *ApJ*, 504, 636
- Hubble, E. P. 1930, *ApJ*, 71, 231
- Hughes, J. P., & Birkinshaw, M. 1998, *ApJ*, 501, 1
- Ikebe, Y., Reiprich, T. H., Böhringer, H., Tanaka, Y., & Kitayama, T. 2002, *A&A*, 383, 773
- Inagaki, Y., Suginozawa, T., & Suto, Y. 1995, *PASJ*, 47, 411
- Itoh, N., Kawana, Y., Nozawa, S., & Kohyama, Y. 2001, *MNRAS*, 327, 567

- Itoh, N., Kohyama, Y., & Nozawa, S. 1998, *ApJ*, 502, 7
- Jing, Y. P. 2000, *ApJ*, 535, 30
- Jing, Y. P., & Suto, Y. 2000, *ApJ*, 529, L69
- . 2002, *ApJ*, 574, 538
- Jones, C., Forman, W., Vikhlinin, A., Markevitch, M., David, L., Warmflash, A., Murray, S., & Nulsen, P. E. J. 2002, *ApJ*, 567, L115
- Kaastra, J. S. 1992, Technical Report, SRON
- Kaastra, J. S., Mewe, R., & Nieuwenhuijzen, H. 1996, in *UV and X-ray Spectroscopy of Astrophysical and Laboratory Plasmas*, 411–414
- Kaastra, J. S., Tamura, T., Peterson, J. R., Bleeker, J. A. M., Ferrigno, C., Kahn, S. M., Paerels, F. B. S., Piffaretti, R., Branduardi-Raymont, G., & Böhringer, H. 2004, *A&A*, 413, 415
- Kasun, S. F., & Evrard, A. E. 2005, *ApJ*, 629, 781
- Kawahara, H., Kitayama, T., Sasaki, S., & Suto, Y. 2008a, *ApJ*, 674, 11
- Kawahara, H., Reese, E. D., Kitayama, T., Sasaki, S., & Suto, Y. 2008b, *ApJ*, 687, 936
- Kawahara, H., Suto, Y., Kitayama, T., Sasaki, S., Shimizu, M., Rasia, E., & Dolag, K. 2007, *ApJ*, 659, 257
- Kay, S. T., da Silva, A. C., Aghanim, N., Blanchard, A., Liddle, A. R., Puget, J.-L., Sadat, R., & Thomas, P. A. 2007a, *MNRAS*, 377, 317
- . 2007b, *MNRAS*, 377, 317
- Kayo, I., Taruya, A., & Suto, Y. 2001, *ApJ*, 561, 22
- Kellogg, E., Gursky, H., Leong, C., Schreier, E., Tananbaum, H., & Giacconi, R. 1971, *ApJ*, 165, L49+
- King, I. 1962, *AJ*, 67, 471
- King, I. R. 1966, *AJ*, 71, 64
- Kitayama, T., Komatsu, E., Ota, N., Kuwabara, T., Suto, Y., Yoshikawa, K., Hattori, M., & Matsuo, H. 2004, *PASJ*, 56, 17
- Knopp, G. P., Henry, J. P., & Briel, U. G. 1996, *ApJ*, 472, 125
- Kobayashi, S., Sasaki, S., & Suto, Y. 1996, *PASJ*, 48, L107
- Komatsu, E., Kitayama, T., Suto, Y., Hattori, M., Kawabe, R., Matsuo, H., Schindler, S., & Yoshikawa, K. 1999, *ApJ*, 516, L1

- Komatsu, E., Matsuo, H., Kitayama, T., Hattori, M., Kawabe, R., Kohno, K., Kuno, N., Schindler, S., Suto, Y., & Yoshikawa, K. 2001, *PASJ*, 53, 57
- Kompaneets, A. S. 1957, *Sov. Phys. JETP*, 4, 730
- Kunieda, H., Inoue, H., Mitsuda, K., & Takahashi, T. 2004, in *Society of Photo-Optical Instrumentation Engineers (SPIE) Conference Series*, Vol. 5488, *Society of Photo-Optical Instrumentation Engineers (SPIE) Conference Series*, ed. G. Hasinger & M. J. L. Turner, 187–196
- Lee, J., Jing, Y. P., & Suto, Y. 2005, *ApJ*, 632, 706
- Lee, J., & Shandarin, S. F. 1998, *ApJ*, 500, 14
- Lee, J., & Suto, Y. 2003, *ApJ*, 585, 151
- . 2004, *ApJ*, 601, 599
- Lewis, A. D., Ellingson, E., Morris, S. L., & Carlberg, R. G. 1999, *ApJ*, 517, 587
- Lewis, G. F., Babul, A., Katz, N., Quinn, T., Herquist, L., & Weinberg, D. H. 2000, *ApJ*, 536, 623
- Liedahl, D. A., Osterheld, A. L., & Goldstein, W. H. 1995, *ApJ*, 438, L115
- Makino, N., Sasaki, S., & Suto, Y. 1998, *ApJ*, 497, 555
- Markevitch, M., Forman, W. R., Sarazin, C. L., & Vikhlinin, A. 1998, *ApJ*, 503, 77
- Markevitch, M., Ponman, T. J., Nulsen, P. E. J., Bautz, M. W., Burke, D. J., David, L. P., Davis, D., Donnelly, R. H., Forman, W. R., Jones, C., Kaastra, J., Kellogg, E., Kim, D.-W., Kolodziejczak, J., Mazzotta, P., Pagliaro, A., Patel, S., Van Speybroeck, L., Vikhlinin, A., Vrtilik, J., Wise, M., & Zhao, P. 2000, *ApJ*, 541, 542
- Mathiesen, B. F., & Evrard, A. E. 2001, *ApJ*, 546, 100
- Mathis, H., Lemson, G., Springel, V., Kauffmann, G., White, S. D. M., Eldar, A., & Dekel, A. 2002, *MNRAS*, 333, 739
- Mazzotta, P., Rasia, E., Moscardini, L., & Tormen, G. 2004, *MNRAS*, 354, 10
- Mewe, R., Gronenschild, E. H. B. M., & van den Oord, G. H. J. 1985, *A&AS*, 62, 197
- Mewe, R., Lemen, J. R., & van den Oord, G. H. J. 1986, *A&AS*, 65, 511
- Mitsuda, K., Takahashi, T., Kunieda, H., Kelley, R. L., Petre, R., & White, N. E. 2008, in *AAS/High Energy Astrophysics Division*, Vol. 10, 20–+
- Mohr, J. J., Mathiesen, B., & Evrard, A. E. 1999, *ApJ*, 517, 627
- Morrison, R., & McCammon, D. 1983, *ApJ*, 270, 119

- Nagai, D., Vikhlinin, A., & Kravtsov, A. V. 2007, *ApJ*, 655, 98
- Navarro, J. F., Frenk, C. S., & White, S. D. M. 1996, *ApJ*, 462, 563
- . 1997, *ApJ*, 490, 493
- Nozawa, S., Itoh, N., & Kohyama, Y. 1998, *ApJ*, 508, 17
- Padoan, P., Nordlund, A., & Jones, B. J. T. 1997, *MNRAS*, 288, 145
- Passot, T., & Vázquez-Semadeni, E. 1998, *Phys. Rev. E*, 58, 4501
- Rasia, E., Mazzotta, P., Borgani, S., Moscardini, L., Dolag, K., Tormen, G., Diaferio, A., & Murante, G. 2005, *ApJ*, 618, L1
- Raymond, J. C., & Smith, B. W. 1977, *ApJS*, 35, 419
- Reese, E. D., Carlstrom, J. E., Joy, M., Mohr, J. J., Grego, L., & Holzzapfel, W. L. 2002, *ApJ*, 581, 53
- Reese, E. D., Mohr, J. J., Carlstrom, J. E., Joy, M., Grego, L., Holder, G. P., Holzzapfel, W. L., Hughes, J. P., Patel, S. K., & Donahue, M. 2000, *ApJ*, 533, 38
- Reiprich, T. H., & Böhringer, H. 2002a, *ApJ*, 567, 716
- . 2002b, *ApJ*, 567, 716
- Rephaeli, Y. 1995, *ApJ*, 445, 33
- Rybicki, G. B., & Lightman, A. P. 1979, *Radiative processes in astrophysics* (New York, Wiley-Interscience, 1979. 393 p.)
- Salpeter, E. E. 1955, *ApJ*, 121, 161
- Sanders, J. S., & Fabian, A. C. 2008, *MNRAS*, L105+
- Sazonov, S. Y., & Sunyaev, R. A. 1998, *ApJ*, 508, 1
- Schuecker, P., Finoguenov, A., Miniati, F., Böhringer, H., & Briel, U. G. 2004, *A&A*, 426, 387
- Seaton, M. J. 1958, *Rev. Mod. Phys.*, 30, 979
- Sereno, M., De Filippis, E., Longo, G., & Bautz, M. W. 2006, *ApJ*, 645, 170
- Sheth, R. K., & Tormen, G. 1999, *MNRAS*, 308, 119
- Shibata, R., Matsushita, K., Yamasaki, N. Y., Ohashi, T., Ishida, M., Kikuchi, K., Böhringer, H., & Matsumoto, H. 2001, *ApJ*, 549, 228
- Shimizu, M., Kitayama, T., Sasaki, S., & Suto, Y. 2006, *PASJ*, 58, 291
- Silk, J., & White, S. D. M. 1978, *ApJ*, 226, L103

- Smith, R. K., Brickhouse, N. S., Liedahl, D. A., & Raymond, J. C. 2001, *ApJ*, 556, L91
- Spergel, D. N., Bean, R., Doré, O., Nolta, M. R., Bennett, C. L., Dunkley, J., Hinshaw, G., Jarosik, N., Komatsu, E., Page, L., Peiris, H. V., Verde, L., Halpern, M., Hill, R. S., Kogut, A., Limon, M., Meyer, S. S., Odegard, N., Tucker, G. S., Weiland, J. L., Wollack, E., & Wright, E. L. 2007, *ApJS*, 170, 377
- Springel, V. 2005, *MNRAS*, 364, 1105
- Springel, V., & Hernquist, L. 2003, *MNRAS*, 339, 289
- Springel, V., Yoshida, N., & White, S. D. M. 2001, *New Astronomy*, 6, 79
- Struble, M. F., & Rood, H. J. 1999, *ApJS*, 125, 35
- Sulkanen, M. E. 1999, *ApJ*, 522, 59
- Sunyaev, R. A., & Zeldovich, Y. B. 1970, *Comments on Astrophysics and Space Physics*, 2, 66
- . 1972, *Comments on Astrophysics and Space Physics*, 4, 173
- Sutherland, R. S. 1999, *MNRAS*, 300, 321
- Suto, Y., Sasaki, S., & Makino, N. 1998, *ApJ*, 509, 544
- Takahashi, T., Kelley, R., Mitsuda, K., Kunieda, H., Petre, R., White, N., Dotani, T., Fujimoto, R., Fukazawa, Y., Hayashida, K., Ishida, M., Ishisaki, Y., Kokubun, M., Makishima, K., Koyama, K., Madejski, G. M., Mori, K., Mushotzky, R., Nakazawa, K., Ogasaka, Y., Ohashi, T., Ozaki, M., Tajima, H., Tashiro, M., Terada, Y., Tsunemi, H., Tsuru, T. G., Ueda, Y., Yamasaki, N., Watanabe, S., & the NeXT team. 2008, arXiv 0807.2007
- Takei, Y., Ohashi, T., Henry, J. P., Mitsuda, K., Fujimoto, R., Tamura, T., Yamasaki, N. Y., Hayashida, K., Tawa, N., Matsushita, K., Bautz, M. W., Hughes, J. P., Madejski, G. M., Kelley, R. L., & Arnaud, K. A. 2007, *PASJ*, 59, 339
- Taruya, A., Takada, M., Hamana, T., Kayo, I., & Futamase, T. 2002, *ApJ*, 571, 638
- Tornatore, L., Borgani, S., Matteucci, F., Recchi, S., & Tozzi, P. 2004, *MNRAS*, 349, L19
- Trimble, V. 1987, *ARA&A*, 25, 425
- Tyson, J. A., Wenk, R. A., & Valdes, F. 1990, *ApJ*, 349, L1
- Uzan, J.-P., Aghanim, N., & Mellier, Y. 2004, *Phys. Rev. D*, 70, 083533
- Vazquez-Semadeni, E. 1994, *ApJ*, 423, 681
- Vázquez-Semadeni, E., & García, N. 2001, *ApJ*, 557, 727
- Vikhlinin, A. 2006, *ApJ*, 640, 710

- Vikhlinin, A., Kravtsov, A., Forman, W., Jones, C., Markevitch, M., Murray, S. S., & Van Speybroeck, L. 2006, *ApJ*, 640, 691
- Vikhlinin, A., Markevitch, M., & Murray, S. S. 2001, *ApJ*, 551, 160
- Wada, K., & Norman, C. A. 2001, *ApJ*, 547, 172
- . 2007, *ApJ*, 660, 276
- Wang, Y.-G., & Fan, Z.-H. 2006, *ApJ*, 643, 630
- Yoshikawa, K., Itoh, M., & Suto, Y. 1998, *PASJ*, 50, 203
- Yoshikawa, K., Taruya, A., Jing, Y., & Suto, Y. 2001, *The Astrophysical Journal*, 558, 520
- Zheng, Z. 2004, *ApJ*, 614, 527

Abbreviations

CDM	cold dark matter, (p1)
CMB	cosmic microwave background, (p1)
SZE	the Sunyaev-Zel'dovich effect, (p1)
PDF	probability density function, (p2)
LOS	line of sight, (p3)
CIE	collisional ionization equilibrium, (p12)
SPH	smoothing particle hydrodynamic, (p21)
IRAS	Infrared Astronomical Satellite, (p21)
RMF	redistribution matrix file, (p35)
RP	radial profile, (p39)
LI	local inhomogeneity, (p39)
PSF	point spread function, (p73)